Title
Encapsulating Metal Clusters and Acid Sites within Small Voids: Synthetic Strategies and Catalytic Consequences

Author
Goel, Sarika

Publication Date
2015

Peer reviewed|Thesis/dissertation

Encapsulating Metal Clusters and Acid Sites within Small Voids: Synthetic Strategies and Catalytic Consequences

by

Sarika Goel

A dissertation submitted in partial satisfaction of the

requirements for the degree of

Doctor of Philosophy

in

Chemical Engineering

in the

Graduate Division

of the

University of California, Berkeley

Committee in charge:

Professor Enrique Iglesia, Chair
Professor Alexander Katz
Professor Jeffrey R. Long

Summer 2015

Encapsulating Metal Clusters and Acid Sites within Small Voids: Synthetic Strategies and Catalytic Consequences

by

Sarika Goel

Abstract

Encapsulating Metal Clusters and Acid Sites within Small Voids: Synthetic Strategies and Catalytic Consequences

by

Sarika Goel

Doctor of Philosophy in Chemical Engineering

University of California, Berkeley

Professor Enrique Iglesia, Chair

The selective encapsulation of metal clusters within zeolites can be used to prepare clusters that are uniform in diameter and to protect them against sintering and contact with feed impurities, while concurrently allowing active sites to select reactants based on their molecular size, thus conferring enzyme-like specificity to chemical catalysis. The apertures in small and medium-pore zeolites preclude the use of post-synthetic protocols to encapsulate the relevant metal precursors because cationic or anionic precursors with their charge-balancing double layer and gaseous complexes cannot diffuse through their windows or channels. We have developed general strategies to encapsulate metal clusters within small-pore zeolites by using metal precursors stabilized by ammonia or organic amine ligands, which stabilize metal precursors against their premature precipitation at the high temperature and pH conditions required for the hydrothermal synthesis of the target zeolite structures and favor interactions between metal precursors and incipient aluminosilicate nuclei during the self-assembly of microporous frameworks. When synthesis temperatures were higher than 400 K, available ligands were unable to prevent the premature precipitation of the metal precursors. In such cases, encapsulation was achieved instead via interzeolite transformations after successfully encapsulating metal precursors or clusters via post-synthesis exchange or ligand protection into parent zeolites and subsequently converting them into the target structures while retaining the encapsulated clusters or precursors. Such strategies led to the successful selective encapsulation of a wide range of metal clusters (Pt, Pd, Ru, Rh, Ir, Re, and Ag) within small-pore (SOD (sodalite), LTA (Linde type A (zeolite A)), GIS (gismondine), and ANA (analcime)) and medium-pore (MFI (ZSM-5)) zeolites. These protocols provide novel and diverse mechanism-based strategies for the design of catalysts with protected active sites.

We have demonstrated the selectivity of the encapsulation processes by combining transmission electron microscopy and chemisorptive titrations with rigorous catalytic assessments of the ability of these materials to catalyze reactions of small molecules, which can access the intracrystalline voids, but not of larger molecules that cannot access the metal clusters within such voids. The selective confinement of clusters also prevented their contact with sulfur compounds (e.g., thiophene and H_2S), thus allowing reactions to occur at conditions that otherwise render unconfined clusters unreactive.

We have also developed synthetic protocols and guiding principles, inspired by mechanistic considerations, for the synthesis of zeolites via interzeolite transformations without the use of organic structure-directing agents (OSDA). More specifically, we have synthesized high-silica MFI (ZSM-5), CHA (chabazite), STF (SSZ-35) and MTW (ZSM-12) zeolites from FAU (faujasite) or BEA (beta) parent materials. Structures with lower framework densities (FAU or BEA) were successfully transformed into thermodynamically-favored, more stable structures with higher framework densities (MFI, CHA, STF, and MTW); to date, target materials with higher Si/Al ratios (Si/Al >10) have not been synthesized via interzeolite transformations without the aid of the OSDA species used to discover these zeolite structures and deemed essential up until now for their successful synthesis. Overcoming kinetic hurdles in such transformations required either the presence of common composite building units (CBU) between parent and target structures or, in their absence, the introduction of small amount of seeds of the daughter structures.

The $NaOH/SiO_2$ ratio, H_2O/SiO_2 ratio and Al content in reagents are used to enforce synchronization between the swelling and local restructuring within parent zeolite domains with the spalling of fragments or building units from seeds of the target structure. The pseudomorphic nature of these seed-mediated transformations, which conserve the volume occupied by the parent crystals and lead to similar size and crystal shape in products, reflect incipient nucleation of target structures occurring at the outer regions of the parent domains and lead to the formation of mesoporosity as a natural consequence of the space-conserving nature of these structural changes and of the higher density of the daughter frameworks. The synthesis mechanism and the guidelines developed enable us to enforce conditions required for the formation of zeolites that previously required OSDA species for their synthesis, thus expanding to a significant extent the diversity of zeolite frameworks that are accessible via these synthesis protocols and providing potential savings in the time and cost involved in the synthesis of some of these zeolite structures.

To my family for their unconditional love and support

Table of Contents

List of Figures

Chapter 2

Chapter 3

Chapter 4

Chapter 6

List of Tables

Chapter 2

Chapter 3

Chapter 4

Chapter 5

Chapter 6

List of Schemes

Chapter 2

Chapter 4

Chapter 5

Chapter 6

Acknowledgments

First and foremost, I would like to extend my sincere thanks and gratitude to my advisor, Professor Enrique Iglesia, for his unconditional support, guidance and patience throughout my graduate studies. I deeply respect and admire his amazing knowledge in the field of catalysis, dedication, hard work and efficiency. It has been an invaluable experience to learn from someone with such an insightful approach to conducting and communicating scientific research. I would also like to thank Dr. Stacey I. Zones (my unofficial advisor) who has taught me everything I know about Zeolites today. His deep knowledge of chemistry, keen insights of zeolite synthesis, enthusiasm of learning and perspectives on life motivate me to strive to improve every single day. I will always be indebted for their time, effort, and patience that has helped me to develop as a researcher and as an individual. I cannot imagine having better advisors and mentors during my graduate studies.

I would also like to thank Professors Shantanu Roy and Rajesh Upadhyay for nurturing my interest in Chemical Engineering during my undergraduate studies and for encouraging me to pursue higher studies. These individuals have been a constant source of inspiration over the years and have always motivated me to aim higher.

I would like to thank all LSAC members, past and present, for their help and support throughout, both personally and professionally. In particular, I would like to thank Nancy Artioli, Robert Carr, Cathy Chin, Minkee Choi, Prashant Deshlahra, David Flaherty, Monica Garcia, Raj Gounder, Elif Gurbuz, Stanley Herrmann, David Hibbitts, Romel Jimenez, Andrew Jones, Will Knaeble, Allie Landry, Jianwei Liu, Brett Loveless, Lei Ma, Erum Mansoor, Gina Noh, Trenton Otto, Michele Sarazen, Shuai Wang, Zhijie Wu, Edwin Yik, Masaoki Iwasaki, Xueyi Zhang and Xiaoqin Zou for engaging discussions, reviewing manuscripts, helping with the experiments and presentations, and most importantly, their invaluable advice.

This work would not have been possible without the support and guidance of collaborators, friends and mentors who continue to inspire and guide me. In particular, I would like to express my sincere gratitude towards Drs. C.Y. Chen, Alex Kuperman, Howard Lacheen, Sonjong Hwang, Robert Saxton, Dan Xie and Professor Alex Katz for their advice, simulating discussions, and extremely productive research collaborations. I would also like to thank Alexander Okrut, Richard Ouyang, Ron Runnebaum, Dandan Zhang and Reena Zalpuri for their help with a range of characterization instruments.

Life outside lab would not have been the same without the awesome friends at Berkeley I was lucky enough to know. In particular, I would like to express my thanks to Sameer Agarwal, Mangesh Bangar, Avinash Bhardwaj, Divya Chandran, Varsha Desai, Rutooj Deshpande, Kartik Ganpati, Satyam Godasi, Gautam Gundiah, Amrita Hazra, Pavan Hosur, Ankit Jain, Kaushik Jayaram, Pallavi Joshi, Sudeep Kamath, Tim Ketron, Debanjan Mukherjee, Prashant Pawan P, Sharanya Prasad, Ram Nekkanti, Manali Nekkanti, Shaama Sharada, Subhashini Srinivasan, and Neeraja Yadwadkar for all the good times and also to help me endure difficult times. I am also very grateful to Jyoti Raghaw, Richa Raj and Ankita Mittal, who in spite of being thousands of miles away, were always ready to lend a listening ear for anything and everything. My graduate

education experience would not have been so amazing without Maureen Apter and her family, Kim Strasburg and my entering class of 2010 PhD ChemE. Their kindness, generosity, love and care helped me adjust to the new surroundings and made me feel like home. The endless support and understanding of all my friends and well-wishers, far and near, throughout the years has meant more to me than words can express.

I have also acknowledged specific technical and intellectual contributions to this research in each chapter. I am also grateful for the generous financial support from the Chevron Energy Technology Company.

Last but not least, I am deeply indebted to my family - my parents, sister, brothers, brother-in-law, and little nephew- for their unconditional love, support, encouragement and understanding. My loving brother, Mayank Goel, whom I deeply miss, taught me what it means to live a life and inspired me to learn, grow and value every moment. Their sacrifices and firm belief in me brought me to where I am today and I dedicate this work to them.

Chapter 1

Introduction to Metal Clusters and Acid Sites Encapsulation within Zeolites Voids

1.1 Introduction

Zeolites are ordered microporous aluminosilicate materials with well-defined crystal structures and voids of molecular dimensions, which allow them to catalyze chemical reactions with unique reactivities and selectivities [1, 2]. The ability of these molecular sieves to control the access and egress of certain reactants and products and to preferentially contain certain transition states while excluding others based on size are described as shape selectivity concepts in acid catalysis by zeolites [3]. Furthermore, synthesis protocols for encapsulating metals [4-11] within zeolites can expand the diversity of catalytic chemistries, made possible by the ability of microporous solids to select reactants, transition states, and products based on their molecular size and shape, and to protect active sites from larger species that can act as poisons by titrating active sites.

General protocols for encapsulating metal clusters within zeolites of different void size and geometry can be used to tailor or select zeolite structures for specific catalytic applications; methods include ion exchange, incipient wetness, and incorporation of metal precursors during synthesis. The confinement of such clusters within small-pore zeolites (< 0.45 nm apertures) cannot be achieved via post-synthesis exchange from aqueous or vapor media, because the size of cationic or anionic precursors, with their charge-balancing double layer, and of gaseous complexes prevent their diffusion through the apertures in these microporous aluminosilicates. In these materials, encapsulation requires that precursors be placed and retained within microporous frameworks during hydrothermal syntheses and subsequent thermal treatment [9, 10]. The high pH (>12) conditions required for hydrothermal crystallization of zeolites typically cause the precipitation of such precursors as colloidal metal hydroxides of sizes larger than the zeolite voids [8], thus preventing their encapsulation. In Chapters 2 and 3, we report a general strategy for encapsulation of metal and oxide clusters within zeolites by choosing the appropriate ligands, such as NH_3 and organic amines, which stabilize metal cations and protect the cationic moieties against premature precipitation as oxyhydroxides during hydrothermal synthesis of zeolites. Avoiding premature precipitation allows zeolite building units to assemble around these solvated ligand-stabilized metal precursors via ubiquitous electrostatic and dispersion interactions that typically enforce the self-assembly of zeolite frameworks. We present the synthetic protocols for the encapsulation of active metals within zeolites with small voids (LTA, SOD, and GIS) and show that such zeolite structures can protect metal (Pt, Pd, Ru, Rh, Re, Ir, and Ag) clusters against sintering and from contact with larger molecules that block active metal surfaces. These data also provide chemical and structural evidence for confinement and for the consequences of encapsulation on catalytic rates and selectivity.

ANA zeolite requires synthesis temperatures (~ 415 K) that decompose even ligand-stabilized metal precursors; in this case, we have enforced encapsulation by first placing metal clusters within zeolites that form at milder conditions (parent structure) and then subjecting the sample to the conditions that convert this parent zeolite to the intended framework (daughter structure), while preserving encapsulation. In Chapter 3, GIS structures that already contain reduced metal clusters

were converted into ANA via local recrystallization processes that retained metal clusters within ANA crystals; these protocols have led to the successful encapsulation of Pt and Ru clusters within ANA voids.

Encapsulation, thermal stability and phase purity for metal containing zeolites were established using X-ray diffraction, transmission electron microscopy, and chemisorptive titration methods. The catalytic consequences of encapsulation were demonstrated in practice and used, in turn, to demonstrate the selectivity of the encapsulation protocols. Oxidative dehydrogenation (ODH) of methanol (kinetic diameter 0.37 nm) and isobutanol (kinetic diameter 0.55 nm), hydrogenation of ethene (kinetic diameter 0.39 nm), isobutene ((kinetic diameter 0.50 nm) and toluene (kinetic diameter 0.59 nm), and ethene hydrogenation in the presence and absence of thiophene (kinetic diameter 0.46 nm) were used to confirm encapsulation and to establish the ability of metal-containing LTA, GIS, and ANA catalysts to select reactants based on size and to protect active sites from large organosulfur poisons. H_2-D_2 (kinetic diameter 0.28 nm) isotopic exchange in the presence and absence of H_2S (kinetic diameter 0.36 nm) was used to probe the ability of metal containing SOD to activate dihydrogen without interferences by large H_2S poison molecules.

MFI (ZSM-5), medium-pore silica-rich zeolite, also requires high crystallization temperatures (423-473 K) and pH (>11) for its template-free hydrothermal synthesis; therefore, metal encapsulation in such materials remains inaccessible via procedures that involve direct hydrothermal synthesis using ligand-stabilized metal precursors, as well as post-synthesis exchange [11], except in the case of monovalent or divalent cations. In Chapter 4, we report a general strategy for the encapsulation of metal clusters within MFI by exploiting interzeolite transformations of BEA or FAU zeolites (parent structures) into MFI zeolite (daughter structure), without organic structure-directing agents (OSDA), and describe the catalytic consequences of the selective encapsulation of metal clusters (Pt, Ru, Rh) within the void spaces of MFI frameworks.

We have established these interzeolite transformations, transformation of one zeolite into another [12, 13], as a general and convenient route for the encapsulation of clusters within microporous solids in those cases for which the successful placement of precursors can be accomplished within a parent zeolite structure via post-synthesis exchange or during hydrothermal crystallization. This parent structure, containing metal clusters within its microporous voids, can then be recrystallized without loss of encapsulation into a daughter structure of higher framework density, for which more direct methods of encapsulation are unavailable or impractical. In the case of MFI, encapsulation was also achieved more directly, but less selectively or quantitatively, by introducing metal precursors later along the nucleation-growth process or by decreasing the pH required for synthesis by using F^- instead of OH^- as mineralizing agents. Such direct methods led to low encapsulation yields, making interzeolite transformations the preferred method for the encapsulation of metal clusters within MFI.

We have extended the interzeolite transformation approach to now synthesize a variety of zeolite frameworks without OSDA species using our developed thermodynamic and kinetic guiding principles. Avoiding the use of OSDA in zeolite synthesis is preferable because the OSDA species are usually very expensive and their removal by thermal treatments (~800-1000 K) is an energy intensive process and involves the release of toxic gases directly into the atmosphere, which increases the economic and environmental burdens of zeolite synthesis protocols. Much effort has

been devoted, therefore, to synthesize zeolites with cheaper OSDA species [14, 15] or avoiding the use of OSDA altogether [13, 16-18]. In Chapter 5, our studies have also led to synthetic protocols and to guiding principles inspired by mechanistic considerations for the synthesis of crystalline microporous solids via interzeolite transformations that avoid direct intervention by OSDA. More specifically, we report the successful synthesis of high-silica (Si/Al = 11-23) MFI, CHA, STF and MTW zeolites via OSDA-free interzeolite transformation methods. Parent zeolites BEA (Framework density (FD) 15.3; defined as T atom/nm^3, where T stands for Si or Al atoms in the zeolite framework [19]) or FAU (FD 13.3) were transformed into target daughter structures MFI (FD 18.4), CHA (FD 15.1), STF (FD 16.9), or MTW (FD 18.2) via recrystallization in aqueous NaOH at hydrothermal conditions, indicating that structures with lower framework densities can be successfully transformed into more stable structures with higher framework densities. Concomitant kinetic hurdles required the presence of a common CBU between parent and target structures or, in their absence, the addition of either seeds *or* OSDA moieties for successful transformations.

A plausible synthesis mechanism, pseudomorphic in nature, and thus preserving the volume and crystal shape of parent structures, for seed-assisted transformations is consistent with the observed effects of the parent Si/Al ratio, the $NaOH/SiO_2$ and H_2O/SiO_2 ratios, and the required synthesis temperature and time, as well as with the crystal shape and presence of intracrystal mesoporous voids in the product crystals. Such phenomena reflect the incipient nucleation of new structures at the outer regions of the parent crystals, which cause the emergence of mesoporosity as a natural consequence of the space-conserving nature of the structural changes and of the higher density of the resulting daughter frameworks. The success and the pseudomorphic nature of these transformations required the synchronization of the "spalling" of seed fragments, when such are needed, and the "loosening" of the parent framework structures. Specific guidelines for successful transformations are inferred from the mechanistic insights of seed-assisted FAU to MFI transformation and from the spontaneous BEA to MFI conversion.

The seed-assisted interzeolite transformation protocols for CHA, STF and MTW zeolites led to highly crystalline product zeolites but their micropore volumes measured by N_2 adsorption measurements were much smaller than the theoretical void spaces of these zeolite frameworks, inconsistent with micropore volumes expected from their crystallinity values obtained from X-ray diffraction measurements. In Chapter 6, the nature of Al and Si species present in product CHA was probed using solid state ^{27}Al, ^{29}Si and ^{23}Na MAS NMR measurements to identity the species potentially causing the pore blocking or aperture narrowing in these materials. We also investigate the possible causes of lower micropore volumes (obtained by N_2 adsorption at 77 K) by changing the adsorbate and adsorption temperatures (adsorption of Ar at 87 K and CO_2 at 195, 273 and 294 K) so as to minimize the diffusion constraints and understand the origins of low adsorbate uptakes. A post-synthetic treatment strategy is, then, proposed and performed which led to successful pore unblocking in these materials to form accessible highly crystalline zeolite products necessary for catalytic applications.

The resulting concepts and strategies, taken together, provide predictive guidance for synthesizing a broad range of zeolite frameworks, without the costs and the environmental impacts typically associated with the use of OSDA moieties, in the direction dictated by thermodynamic

guidance and with kinetics mediated by either common structural units along the reaction coordinate or by seeds of the target product.

1.2 References

(1) Csicsery, S. M. *Zeolites* 1984, 4, 202.
(2) Davis, M. E. *Chem. Mater.* 2014, 26, 239.
(3) Corma, A. *Chem. Rev.* 1995, *95* (3), 559.
(4) Sachtler, W. M. H. *Acc. Chem. Res.* 1993, 26, 383.
(5) Gallezot, P. *Post-Synthesis Modification I* 2002, 257.
(6) Flytzani-Stephanopoulos, M.; Gates, B. C. *Annu. Rev. Chem. Biomol. Eng.* 2012, *3*, 545.
(7) Zhan, B.-Z.; Iglesia, E. *Angew. Chem. Int. Ed.* 2007, *46*, 3697.
(8) Choi, M.; Wu, Z.; Iglesia, E. *J. Am. Chem. Soc*. 2010, 132, 9129.
(9) Balkus, K. J.; Gabrielov, A. G. *J. Inclusion Phenom. Mol. Reco. Chem.* 1995, 21, 159.
(10) Wu, J. C. S.; Goodwin J. G.; Davis M. *J. Catal.* 1990, 125, 488.
(11) Altwasser, S.; Gläser, R.; Lo, A. S.; Liu, P.-H.; Chao, K.-J.; Weitkamp, J. *Micropor. Mesopor. Mater.* 2006, 89, 109.
(12) Zones, S. I. *J. Chem. Soc., Faraday Trans*. 1991, 87, 3709.
(13) Sano T., Itakura M., Sadakane M. *J. Japan Petro. Inst.* 2013, 56 (4), 183.
(14) Zones, S. I.; Hwang, S.-J. *Chem. Mater.* 2002, *14* (1), 313.
(15) Lee, H.; Zones, S. I.; Davis, M. E. *Nature* 2003, *425* (6956), 385.
(16) Xie, B.; Zhang, H.; Yang, C.; Liu, S.; Ren, L.; Zhang, L.; Meng, X.; Yilmaz, B.; Müller, U.; Xiao, F.-S. *Chem. Commun.* 2011, *47* (13), 3945.
(17) Itabashi, K.; Kamimura, Y.; Iyoki, K.; Shimojima, A.; Okubo, T. *J. Am. Chem. Soc.* 2012, *134* (28), 11542.
(18) Maldonado, M.; Oleksiak, M. D.; Chinta, S.; Rimer, J. D. *J. Am. Chem. Soc.* 2013, *135* (7), 2641.
(19) Baerlocher, C.; McCusker, L. B. Database of Zeolite Structures: http://www.iza-structure.org/databases/.

Chapter 2

Hydrothermal Synthesis of LTA-Encapsulated Metal Clusters and Consequences for Catalyst Stability, Reactivity and Selectivity

Abstract

Noble metal clusters (Pt, Pd, Rh, Ir, Re and Ag) are selectively encapsulated within LTA voids via hydrothermal synthesis using metal precursors with ligands (NH_3 for Pt and Ir; ethylenediamine for Pd, Rh, Re and Ag) that prevent their premature precipitation as colloidal oxyhydroxides. Such stability appears to be necessary and sufficient for successful encapsulation of cationic precursors during nucleation and growth of zeolite frameworks. Mean cluster diameters measured by titration of exposed metal atoms (H_2 on Pt, Pd, Rh, Ir, Re; O_2 on Ag; 1.1-1.8 nm) and by transmission electron microscopy (1.2-1.9 nm), were similar, indicating that cluster surfaces were clean and accessible to molecules used as titrants or reactants. Metals clusters were narrowly distributed in size and stable against sintering and coalescence during oxidative thermal treatments (573-873 K). Encapsulation selectivities were measured from turnover rates for reactions of small and large reactants, specifically hydrogenation of alkenes (ethene and isobutene) and oxidation of alkanols (methanol and isobutanol), which reflect the restricted access to encapsulated clusters by the larger molecules. These encapsulation selectivities, which reflect the ratio of metal surface areas within and outside LTA crystals ranged from 7.5-83 for all samples. Confinement within LTA crystals protects clusters from contact with thiophene and allows ethene hydrogenation to proceed at thiophene concentrations that fully suppressed reactivity for metal clusters dispersed on mesoporous SiO_2. These protocols provide a general strategy for encapsulating clusters within small-pore zeolite voids, for which post-synthesis exchange is infeasible. Their successful encapsulation protects such clusters from coalescence and growth and allows them to select reactants and reject poisons based on their molecular size.

2.1 Introduction

The encapsulation of metal or oxide clusters within small-pore zeolites provides potential routes to prepare catalysts with small metal clusters uniform in size, to select reactants, transition states and products based on molecular sizes, and to protect such clusters against sintering or poisoning during thermal treatment or catalysis [1-4]. Such strategies, however, present formidable synthetic and characterization challenges. Encapsulation within small-pore (8-membered ring (8-MR)) and medium-pore (10-MR) zeolites cannot be achieved through post-synthesis exchange, impregnation [5], or adsorption/decomposition of metal complexes, because multivalent cations in aqueous media form solvated oligomeric complexes larger than the small apertures provided by the windows in these zeolites [2, 3, 6]. Therefore, metal precursors must be present during hydrothermal synthesis and must remain stable at the demanding conditions required for hydrothermal crystallization of aluminosilicate gels into zeolite frameworks with pores of small (0.3-0.5 nm) or medium (0.5-0.6 nm) size [6-27].

The successful encapsulation of Pt clusters within LTA [6-14] and MFI [15], of Ru clusters within LTA [16] and MFI [17], of Rh clusters within LTA [18-22], and of Au clusters within MFI

[23] has been reported via hydrothermal syntheses. These studies recognized the need for metal precursors to be present during zeolite crystallization and inferred the success of encapsulation from chemisorption uptakes or transmission electron micrographs. These reports of successful encapsulation, however, used metal precursors that precipitate as colloidal oxyhydroxides at the pH and temperatures required for zeolite synthesis [24-29], making the reported encapsulations infeasible.

Here, we report a general strategy for encapsulation of metal and oxide clusters within LTA by choosing ligands that stabilize metal cations and protect the cationic moieties against precipitation as oxyhydroxides during hydrothermal synthesis of zeolites (Scheme 2.1) (Table 2.1, solution behaviour of various metal complexes at hydrothermal synthesis conditions in the absence of silica). Avoiding premature precipitation allows zeolite building units to assemble around these solvated ligand-stabilized precursors via ubiquitous electrostatic and dispersion interactions that typically enforce the self-assembly of zeolite frameworks.

We show here that these methods lead to selective encapsulation of Pt, Pd, Rh, Ir, Re and Ag clusters within LTA zeolites, which consist of sodalite cages (pore diameter 0.6 nm) and α cages (pore diameter 1.1 nm). These materials are used here to explore the consequences of encapsulation for cluster stability, reactivity and selectivity using reactants of varying sizes and diffusivities. X-ray diffraction (XRD), transmission electron microscopy (TEM) and H_2 or O_2 chemisorption uptakes are used to measure zeolite phase purity, cluster sizes and thermal stability. The oxidative dehydrogenation (ODH) of methanol and isobutanol (kinetic diameters: 0.37 nm [16, 30, 31] and 0.55 nm [24, 30], respectively) and the hydrogenation (HD) of ethene and isobutene (0.39 nm [32] and 0.50 nm [30], respectively) are used to confirm encapsulation by comparing the reactivity of smaller and larger reactants on metal clusters on LTA and mesoporous SiO_2. Ethene hydrogenation rates with and without thiophene (0.46 nm [11]) also demonstrate the high encapsulation selectivity and the ability of LTA frameworks to protect clusters from contact with organosulfur compounds, thus preserving their surface cleanliness and reactivity during hydrogenation catalysis.

2.2 Methods

2.2.1 Materials

Fumed SiO_2 (0.014 μm, 200 ± 25 m^2 g^{-1}, Sigma), $NaAlO_2$ (anhydrous, Riedel-de Haën, technical), NaOH (99.995%, Aldrich), $Pd(NO_3)_2$ (99.99%, Alfa Aesar), $[Pd(NH_3)_4](NO_3)_2$ (10 % wt. in H_2O, Aldrich), $[Pd(NH_2CH_2CH_2NH_2)_2]Cl_2$ (99.9%, Aldrich), $[Pt(NH_3)_4]$ $(NO_3)_2$ (99.99%, Alfa Aesar), $[Rh(NH_3)_5Cl]Cl_2$ (Rh 34.5% min, Alfa Aesar), $[Rh(NH_2CH_2CH_2NH_2)_3]Cl_3$ (≥ 99.5%, Aldrich), $[Ir(NH_3)_5Cl]Cl_2$ (99.9%, Alfa Aesar), $AgNO_3$ (99.9999%, Aldrich), NH_4ReO_4 (99.9%, Aldrich), $[Re(NH_2CH_2CH_2NH_2)_2O_2]Cl$ (99.8%, Aldrich), $NH_2CH_2CH_2NH_2$ (99.8%, Aldrich), $NH_3 \cdot H_2O$ (28 % wt. in H_2O, Aldrich).

2.2.2 Catalyst Synthesis

2.2.2.1 Metal-Free LTA

A synthesis gel with the molar composition of 2.6 Na_2O: 1.0 Al_2O_3: 1.5 SiO_2: 92.6 H_2O was prepared. In a typical experiment, 6.0 g $NaAlO_2$ and 4.7 g NaOH were dissolved in 62.0 cm^3 demineralized H_2O and mixed with 3.2 g fumed SiO_2. The resultant gel was transferred into a 500 cm^3 polypropylene container (Nalgene), sealed, and homogenized by magnetic stirring at 800 rpm for 600 s. The gel was stirred in an oil bath at 400 rpm and 333 K for 4 h. After 4 h, the slurry temperature was raised (~ 0.03 K s^{-1}) to 373 K and the sample was magnetically stirred at 400 rpm for 16 h. The solids were collected on a fritted funnel (Pyrex 36060, 10-15 μm) and washed with deionized water until the rinse liquid reached pH 7-8. The collected sample was treated in ambient air at 373 K for 6 h.

2.2.2.2 Metal Clusters Encapsulated within LTA

Pt, Rh and Re Clusters Encapsulated within LTA. An aluminosilicate gel with the same composition as metal-free LTA synthesis (Table 2.2) was prepared and magnetically stirred at 400 rpm and 333 K for 3 h. $[Pt(NH_3)_4](NO_3)_2$, $[Rh(NH_2CH_2CH_2NH_2)_3]Cl_3$ or $[Re(NH_2CH_2CH_2NH_2)_2O_2]Cl$ (Table 2.2) was dissolved in 10.0 cm^3 H_2O and added dropwise to the gel at 0.08 cm^3 s^{-1}. The gel was homogenized by vigorous magnetic stirring (400 rpm) at 333 K for 1 h. Then, the synthesis temperature was raised to crystallization temperature of 373 K (~0.03 K s^{-1}) and the mixture was stirred at 400 rpm for 16 h. The solids were filtered, washed and dried using the same procedure as for metal-free LTA. Samples were treated in air (99.999%, Praxair, 1.67 cm^3 g^{-1} s^{-1}) at 673 K (0.08 K s^{-1}) for 3 h and then in 9% H_2/He (99.999%, Praxair, 1.67 cm^3 g^{-1} s^{-1}) at 623 K (0.08 K s^{-1}) for 4 h to remove the ligands used to stabilize metal precursors and reduce cations to their respective zero-valent states. Samples were passivated under 0.5% O_2/He (99.999%, Praxair, 1.67 cm^3 g^{-1} s^{-1}) for 1 h at 300 K before air exposure.

Pd, Ir and Ag Clusters Encapsulated within LTA. The encapsulation of Pd, Ir and Ag clusters within LTA required initially dispersed ligand-stabilized metal precursors over the SiO_2 surface [19, 20]. For synthesis of Pd/LTA or Ir/LTA, $[Pd(NH_2CH_2CH_2NH_2)_2]Cl_2$ or $[Ir(NH_3)_5Cl]Cl_2$ (Table 2.2) was first dissolved in 30.0 cm^3 deionized water and then 3.2 g fumed SiO_2 was added to the mixture. The resulting mixture was stirred at 400 rpm and 333 K for 3 h. Then, 32.0 cm^3 alkaline solution containing 4.7 g NaOH and 6.0 g $NaAlO_2$ was added to the mixture and stirred (400 rpm) at 333 K for 1 h. The temperature was raised to the crystallization temperature of 373 K (~ 0.03 K s^{-1}) and the slurry was stirred at 400 rpm for 16 h. Ag/LTA was synthesized using ethylenediamine-stabilized Ag precursor, prepared by dissolving $AgNO_3$ in 10 cm^3 of 10 wt.% aqueous ethylenediamine solution. Subsequent steps were the same as for the encapsulation of Pd clusters in LTA. The resulting products were separated by filtering, washed and dried using the same procedure as for metal-free LTA. Pd and Ir samples were first treated in air (99.999%, Praxair, 1.67 cm^3 g^{-1} s^{-1}) at 673 K (0.08 K s^{-1}) for 3 h and then in 9% H_2/He (99.999%, Praxair, 1.67 cm^3 g^{-1} s^{-1}) at 623 K (0.08 K s^{-1}) for 4 h to remove ligands and to reduce cations to their respective zero-valent states. The Ag sample was first treated in air (99.999%, Praxair, 1.67 cm^3 g^{-1} s^{-1}) using the same procedure as for Pd/LTA and then in 9% H_2/He (1.67 cm^3 g^{-1} s^{-1}) at 523 K (0.03 K s^{-1}). All samples were passivated under 0.5% O_2/He (99.999%, Praxair, 1.67 cm^3 g^{-1} s^{-1}) for 1 h at 300 K before air exposure.

Silica-Supported Metal Clusters. The metal clusters supported on SiO_2 (Davisil®, Grade 646, 300 m^2 g^{-1}, 10 nm mean pore diameter) were prepared by impregnation [24, 33] with aqueous

solutions of the same metal precursors as in the case of LTA. Solutions (0.1 M) of $[Pt(NH_3)_4](NO_3)_2$, $[Pd(NH_2CH_2CH_2NH_2)_2]Cl_2$, $[Rh(NH_2CH_2CH_2NH_2)_3]Cl_3$, $[Ir(NH_3)_5Cl]Cl_2$, $[Re(NH_2CH_2CH_2NH_2)_2O_2]Cl$ or $[Ag(NH_2CH_2CH_2NH_2)]NO_3$ were prepared and then diluted to 0.004–0.011 M. SiO_2 (5.0 g) was then added to these solutions and the mixture was stirred (400 rpm) for 4 h and subsequently treated at 373 K overnight under rotation to remove water. The solid samples were treated in ambient air at 373 K for 6 h, then heated in air (99.999%, Praxair, 1.67 $cm^3\ g^{-1}\ s^{-1}$) at 623 K (0.03 K s^{-1}) for 2 h, and in 9% H_2/He (99.999%, Praxair, 1.67 $cm^3\ g^{-1}\ s^{-1}$) at 623 K (0.03 K s^{-1}) for 2 h. Samples were passivated under 0.5% O_2/He (99.999%, Praxair, 1.67 $cm^3\ g^{-1}\ s^{-1}$) for 1 h at 300 K before air exposure.

2.2.3 Characterization

X-ray diffractograms were measured using a Siemens D500 diffractometer and Cu Kα radiation (λ = 0.15418 nm) on samples ground to fine powder and spread uniformly with Vaseline onto a glass slide. Diffractograms were measured for 2θ values of 5-50° at 0.02° intervals. Metal contents were measured by inductively coupled plasma atomic emission spectrometry (ICP-AES) using an IRIS Intrepid spectrometer. Metal dispersions were measured by H_2 chemisorption on Pt, Pd, Rh, Ir and Re samples and by O_2 chemisorption on Ag samples using an Autosorb-1 apparatus (Quantachrome). For H_2 chemisorption, samples were first treated in pure H_2 (99.999%, Praxair; 1 bar) at 623 K (0.08 K s^{-1}) for 1 h and then in dynamic vacuum at 623 K for 1 h. Hydrogen adsorption isotherms were measured at 313 K and 5.0-50 kPa of H_2 for Pt, Rh and Ir samples, and at 623 K and 5.0-50 kPa of H_2 for Re samples [34]. In order to avoid formation of the β-hydride phase in Pd samples [35], hydrogen adsorption isotherms were measured at 343 K and 0.4-1.5 kPa of H_2. For oxygen chemisorption, samples were treated in pure H_2 at 523 K (0.08 Ks^{-1}) for 1 h and then evacuated under vacuum at 523 K for 2 h. Oxygen adsorption isotherms were measured at 443 K and 10-30 kPa of O_2 on Ag samples [36]. Metal dispersions were calculated using $H/Pt_s=1$, $H/Pd_s=1$, $H/Rh_s=1$, $H/Ir_s=2$ [37], $H/Re_s=4$ [34, 38], and $O/Ag_s=1$ adsorption stoichiometry. Mean cluster sizes were calculated from these dispersion values by assuming spherical clusters [39].

Transmission electron microscopy (TEM) images were taken with a Philips 420 TEM operated at 120 kV. Before TEM analysis, samples were embedded into an adhesive polymer, mechanically thinned, and dimpled and further thinned by ion-polishing at about 3.0 kV on a Gatan PIP. Metal cluster size distributions were determined by counting > 400 crystallites. The surface area weighted cluster diameters, $d_{TEM,}$ were calculated using $d_{TEM} = \sum n_i d_i^3 / \sum n_i d_i^2$ [39, 40].

2.2.4 Catalytic Reactions

All gases [He (99.999%, Praxair), H_2 (99.999%, Praxair), C_2H_4 (5% C_2H_4/He, Praxair, CS), Air (99.999%, Praxair), 20% O_2/He (99.999%, Praxair), 9% H_2/He (99.999%, Praxair), isobutene (99%, Aldrich)] were purified by an O_2/H_2O trap (Agilent) to remove trace H_2O and O_2 (except for O_2/He). CH_3OH (99.9%, Aldrich), C_2H_5OH (99.9%, Aldrich), i-C_4H_9OH (99.9%, Aldrich) were used as received. Thiophene (99%, Aldrich) was purified over degassed molecular sieve 3A and by repeated freeze-vacuum-thaw cycle using dry ice/acetone traps (195 K).

Oxidative dehydrogenation (ODH) and hydrogenation (HD) reactions were carried out in a packed-bed quartz micro-reactor. Catalyst powders were diluted with fumed SiO_2 (Cab-O-Sil, HS-

5, 310 $m^2 g^{-1}$) to a SiO_2/catalyst weight ratio of 10 (100 for Pt/SiO_2). The mixtures were pelletized and sieved to retain aggregates 0.18 to 0.25 mm in diameter and diluted with quartz granules of similar size to avoid bed temperature gradients. For oxidative dehydrogenation of alkanols, samples were treated in flowing H_2 (1.67 $cm^3 g^{-1} s^{-1}$) at 573 K with 0.08 K s^{-1} (except Ag samples; treated at 523 K with 0.03 K s^{-1}) for 1 h and then cooled to 393 K and treated in 20% O_2/He (1.67 $cm^3 g^{-1} s^{-1}$) for 1 h before catalytic measurements. Alkanol (methanol and isobutanol) oxidative dehydrogenation reactions were carried out with 4 kPa alkanols and 9 kPa O_2 at 393 K (353 K in methanol ODH on Pt). Alkene (ethene and isobutene) hydrogenation reactions were carried out with 1.5 kPa alkenes and 5 kPa H_2 at 294 K. Ethene hydrogenation with/without 0.1 kPa thiophene were carried out with 1.5 kPa ethene and 5 kPa H_2 at 294 K to probe the ability of LTA structures to protect active sites from thiophene and the extent of encapsulation. Selectivities are reported on a carbon basis as the percentage of the converted alkanol or alkene appearing as a given product. Turnover rates were reported as the molecules converted per time normalized by the number of surface metal atoms. Blank experiments using empty reactors, quartz, metal-free Na-LTA or fumed SiO_2 did not lead to detectable alkanol or alkene conversions at any of the conditions used in this study. Turnover rates did not depend on the extent of dilution at 10:1 and larger diluent: catalyst mass ratios. No deactivation was detected during ODH and hydrogenation reactions on metal clusters on LTA or SiO_2 (over 72 h). Reactants and product concentrations were measured by on-line gas chromatography (Agilent 6890GC) using a methyl-silicone capillary column (HP-1; 50 m × 0.25 mm, 0.25 μm film thickness) and a Porapak Q packed column (80-100 mesh, 1.82 m × 3.2 mm) connected to flame ionization and thermal conductivity detectors, respectively.

2.3 Results and Discussion

We report here the synthesis of noble metal clusters (Pt, Pd, Rh, Ir, Re, and Ag) encapsulated within LTA zeolites by the stabilization of metal precursors using NH_3 or ethylenediamine ligands to prevent their premature precipitation as colloidal hydroxides at the pH and temperatures required for zeolite crystallization. The zeolite framework may function as a ligand, an anion or a solvent as it assembles building blocks around the metal complexes during nucleation and growth of the zeolite framework [26-29]. The NH_3 and ethylenediamine ligands may act as bridges between metal cations and zeolite frameworks to form stable complexes within cavities that allow adequate volume for these metal complexes [26, 27]; these ligands also act as surface functionalization groups for silica and alumina moieties and thus promote the uniform dissemination of metal cationic species throughout the surfaces of mesoporous oxides typically used as catalyst supports [26, 41-43].

The precipitation of metal complexes as insoluble oxyhydroxides in aqueous zeolite synthesis media can be prevented by screening of precursors and ligands for their stability. The solubility product constant (K_{sp}) of metal hydroxides ($M(OH)_m$), $K_{sp}=[M^{m+}]\times[OH^-]^m$ ($M^{m+}=Pt^{2+}$, Pd^{2+}, Rh^{3+}, Ir^{3+}, Re^{5+} and Ag^+; $[OH^-]=m[M^{m+}]$), is the product of the equilibrium concentrations of the ions in a saturated solution of metal hydroxides, with each concentration raised to an exponent corresponding to the stoichiometric coefficient of that ion in the chemical reaction equation [44-46]. The solubility quotient (Qc) of metal cations and hydroxide anions, $Q_c=[M^{n+}]\times[OH^-]^n$ ($M^{n+}=Pt^{2+}$, Pd^{2+}, Rh^{3+}, Ir^{3+}, Re^{5+} and Ag^+), is the product of the concentrations of metal cations and hydroxide anions in any solution. Precipitation occurs when Q_c becomes equal to K_{sp}, although slightly higher values may be required to overcome nucleation barriers, which require

supersaturation of solutions [44-46]. In our synthesis protocols, we maintain the Q_c for metal cations and hydroxide anions to values below K_{sp} for each specific ion pairs (entries in bold, Table 2.1) to avoid precipitation of metal cations in the zeolite synthesis gels at ambient temperature (~298 K) using suitable ligands to decrease metal cation (Pt^{2+}, Pd^{2+}, Rh^{3+}, Ir^{3+}, Re^{5+} and Ag^{+}) concentrations through complexation with ligands (Table 2.1, NH_3 as the ligand: $[Pt(NH_3)_4]^{2+}$ and $[Ir(NH_3)_5Cl]^{2+}$ complex ions; ethylenediamine as the ligand: $[Pd(NH_2CH_2CH_2NH_2)_2]^{2+}$, $[Rh(NH_2CH_2CH_2NH_2)_3]^{3+}$, $[Re(NH_2CH_2CH_2NH_2)_2O_2]^{+}$ and $[Ag(NH_2CH_2CH_2NH_2)]^{+}$ complex ions) in aqueous solution [42, 44-50].

Precursors were chosen based on their stability and then examined at the pH conditions and temperatures (373 K) required for hydrothermal zeolite syntheses, but in the absence of the silica in order to allow visual detection of any colloids formed (Table 2.1). Table 2.1 shows the metal precursors tested for their stability and those shown to remain in solution without precipitation as oxyhydroxides. Preventing premature precipitation provides the opportunity for zeolite building units to self-assemble around ligand-stabilized metal cations during hydrothermal synthesis. These processes are mediated by electrostatic or van der Waals interactions; they are essential for the nucleation and growth of crystalline zeolite frameworks and for the uniform distribution and ultimate encapsulation of active metals within such frameworks [24-29].

2.3.1 Size and Stability of Metal Clusters

X-ray diffractograms (XRD) of metal-containing LTA zeolites detected crystalline LTA structures after hydrothermal synthesis in the presence and absence of ligand-stabilized metal precursors (Figure 2.1 for Pt and Rh; Figure 2.S1 for Pd, Ir, Re and Ag clusters in LTA). Subsequent thermal treatment in flowing air at 673 K and H_2 at 623 K (Ag at 523 K) for 4 h did not lead to detectable changes in crystallinity. M/LTA (M= Pt, Pd, Rh, Ir, Re, and Ag) samples show only the characteristic lines of LTA structure without any detectable diffraction lines for the respective metal phase after treatment in H_2 at 623 K (Ag at 523 K) for 4 h (0.35-1.40 wt.% metal; Table 2.3). These data confirmed the thermal stability of Na-LTA structures and the substantial absence of large metal crystallites.

Chemisorption uptakes of H_2 or O_2 gave higher dispersions (0.62–0.91, Table 2.3) for clusters in LTA than for clusters on SiO_2 (0.22-0.74, Table 2.3) at similar metal contents (0.35-1.40 wt.%, Table 2.3) after treatment in H_2 (99.999%, Praxair) at 623 K (0.08 K s^{-1}) for 1 h and then in dynamic vacuum at 623 K for 1 h. TEM images (Figure 2.2 and 2.S2) were used to calculate the dispersity index (DI) of the metal clusters (Figure 2.3). The DI value is given by surface-averaged diameter ($d_{TEM} = \sum n_i d_i^3 / \sum n_i d_i^2$) divided by the number-averaged diameter ($d_n = \sum n_i d_i / \sum n_i$). This parameter is a measure of the cluster size non-uniformity, with a value of unity reflecting unimodal clusters and values smaller than 1.5 to relatively uniform size distributions [39, 40, 51]. The DI value for all M/LTA samples was near unity (1.03-1.12, Figure 2.3a), consistent with very narrow size distributions in all samples. The size uniformity and the mean cluster diameters evident from these TEM images suggest that metal clusters reside within the LTA crystals, a conclusion confirmed below from catalytic reactions for large and small molecules.

Surface-averaged mean cluster diameters (d_{TEM} = 1.1–1.9 nm, Figures 2.2 and 2.S2) from TEM images were larger than LTA cages (0.6 nm sodalite cage and 1.1 nm α-cage) for most metals.

Metal clusters appear to span more than one cage, but remain isolated from the external surface by many intervening intact cages and windows, thus providing the reactant shape selectivity that we seek (section 2.3.2). The formation of crystal defects around growing clusters is expected [3] and [4], but local lattice defects are difficult to detect by XRD and TEM. Moreover, the formation of metal clusters larger than cage dimensions may occur concurrently with local re-crystallization, in a process that would heal any structural defects, thus leading to the observed modestly uniform size and spherical shape of the clusters [52] and making the detection of defects by XRD or TEM impossible.

The use of N-containing ligands as protecting agents in metal precursors can, in some instances, lead to residual fragments strongly bound at metal cluster surfaces, thus making such surfaces inaccessible to molecules in chemisorption and catalytic processes. Surface cleanliness was confirmed by comparing H_2 (for Pt, Pd, Rh, Ir and Re) and O_2 (for Ag) chemisorption uptakes with those expected from the size distribution detected by TEM. A surface cleanliness index (CI) was defined as the ratio of the diameter determined from H_2 and O_2 chemisorption (d_{chem} = 1.2-1.8 nm, Table 2.3) to the surface-averaged diameter from TEM images (d_{TEM} = 1.1-1.9 nm, Figures 2.2 and 2.S2). A value of unity indicates that clusters detected in micrographs exhibit clean surfaces capable of binding H and O with the expected adsorption stoichiometry after treatment in H_2 at 673 K (Ag at 523 K) for 4 h; values larger than unity would indicate the presence of residues at cluster surfaces. All M/LTA samples gave CI values near unity (0.92–1.20, Figure 2.3b), consistent with the presence of essentially clean surfaces and with the complete removal of N-containing ligands or any other residues. Such surfaces are therefore available to catalyze reactions of any molecules that can reach such sites by diffusing through the LTA microporous framework.

Such clean clusters of nearly unimodal size do not sinter or coalesce even at high treatment temperatures (523–873 K), apparently because of their effective isolation by confinement and their spatial uniformity. Only a small fraction (~0.29-3.37%, Table 2.3) of α-cages in LTA is occupied by clusters and their mean distances are 7.4-16.7 nm (Table 2.3). The data in Figure 2.4 demonstrate this remarkable size stability for the specific case of Pt and Rh and contrast the properties of these metal-containing Na-LTA zeolites with the growth of clusters of similar size dispersed on mesoporous SiO_2.

Pt and Rh mean cluster diameters (d_{chem}) were calculated based on dispersions measured by H_2 chemisorption on Pt/LTA (0.76 wt.% Pt) and Rh/LTA (0.35 wt.% Rh) samples treated in flowing dry air (99.999%, Praxair, 1.67 $cm^3\ g^{-1}\ s^{-1}$) at temperatures between 523 and 873 K for 4 h and then in flowing H_2 (1.67 $cm^3\ g^{-1}\ s^{-1}$) at 623 K for 4 h. These data are shown together with the corresponding data for Pt/SiO_2 (0.79 wt.% Pt) and Rh/SiO_2 (1.10 wt.% Rh) in Figure 2.4. On SiO_2, cluster diameters increased from 2.0 nm to 3.2 nm and 1.9 nm to 2.9 nm for Pt and Rh clusters, respectively, when samples were treated at 523 K and 873 K in flowing dry air (1.67 $cm^3\ g^{-1}\ s^{-1}$) and then in flowing H_2 (1.67 $cm^3\ g^{-1}\ s^{-1}$) at 623 K for 4 h. In contrast, the diameter of Pt and Rh clusters in LTA decreased slightly (from 2.0 nm to 1.5 nm and 1.4 nm to 1.2 nm for Pt and Rh, respectively) when samples were treated from 523 to 673 K in flowing dry air (1.67 $cm^3\ g^{-1}\ s^{-1}$) and then remained constant after treatment in flowing dry air (1.67 $cm^3\ g^{-1}\ s^{-1}$) at temperatures up to 873 K. The initial decrease in cluster diameter reflects either the migration of metal atoms from inaccessible sodalite cages (0.6 nm 6-MR cage, connected by 0.16 nm 4-MR windows) into α-cages (1.1 nm 8-MR cages connected by 0.22 nm 6-MR and

0.41 nm 8-MR windows) [11], where they become accessible to H_2 (0.29 nm kinetic diameter [24]) and O_2 (0.35 nm kinetic diameter [24]) titrants or the more complete removal of ligands or other residues deposited during hydrothermal crystallization [2, 3, 53, 54]. Sodalite cages (0.22 nm window) prevent access and egress of most molecules and make reduction and removal of ligands difficult at low temperatures [11, 53, 54].

These data, taken together, indicate that confinement of small and uniform metal clusters within LTA voids inhibits coalescence and Ostwald ripening of such metal clusters. Their surfaces are able to bind H and O atoms, suggesting that they can catalyze reactions of any reactants that can diffuse through the windows in LTA zeolites. This protection from cluster coalescence and growth, which occur ubiquitously in mesoporous SiO_2, appears to require that clusters reside within LTA voids. Next, we show that such clusters are indeed located within LTA voids by measuring the rates of reactions of large and small molecules and comparing their reactivities with those measured on mesoporous SiO_2 supports, where reactant size does not influence accessibility and, consequently, reactivity. In doing so, we exploit the intended benefits of encapsulating active sites, present on cluster surfaces within confining zeolite voids, in selecting reactants based on molecular size to demonstrate the ability of our synthetic protocols to achieve encapsulation.

2.3.2 Reactant Selectivity in Alkanol Dehydrogenation and Alkene Hydrogenation

Encapsulation confers active sites with the ability to make contact with only certain reactants and/or to form certain transition states and products based on their molecular sizes and shapes [24, 25]. Here, we specifically address reactant shape selectivity by using the oxidative dehydrogenation (ODH) of alkanols (methanol and isobutanol; 0.37 and 0.55 nm respective kinetic diameters) and the hydrogenation (HD) of alkenes (ethene and isobutene; 0.39 and 0.50 nm respective kinetic diameters); these reactions of large and small molecules allow a quantitative measure of the relative surface areas of Pt, Pd, Rh, Ir, Re and Ag clusters residing within and outside the confined environment of the microporous voids provided by LTA zeolites. The small windows in LTA (0.41 nm × 0.41 nm) allow facile diffusion of methanol and ethene reactants, but impede or at least restrict access to intracrystal spaces by the larger isobutanol and isobutene molecules. As a result, the relative rates of reactions of small and large reactants on restricted and unrestricted locations provide a measure of the fraction of the metal surface area that resides within LTA voids.

The ratios of ODH or HD turnover rates for small and large reactants, defined as χ ($\chi_{ODH,i} = r_{methanol}/r_{isobutanol}$ and $\chi_{HD,i} = r_{ethene}/r_{isobutene}$; i = LTA, SiO_2), are larger on clusters encapsulated within LTA than on unconstrained clusters dispersed on mesoporous SiO_2. The ratios of these χ values on LTA and SiO_2 samples can then be used to define an encapsulation selectivity parameter ($\phi = \chi_{j,\,LTA}/\chi_{j,\,SiO2,}$ j = ODH, HD) for each reaction-reactant pair [24, 25]. This parameter provides an accurate estimate of the extent to which the active surfaces reside within the inaccessible intracrystal regions of LTA, which larger reactants cannot access [24, 25]. Encapsulation selectivities (ϕ) near unity would indicate nearly unrestricted access to active sites by both large and small reactants and unsuccessful encapsulation. Large ϕ values, in contrast, provide evidence that clusters predominantly reside within regions that restrict access to the larger reactants, thus making them appear much less reactive than clusters dispersed on accessible mesoporous SiO_2 supports.

2.3.2.1 Oxidative Dehydrogenation (ODH) of Alkanols

Alkanol ODH reactions form alkanals as primary products; alkanals undergo secondary reactions with alkanols to form hemiacetals or alkoxyalkanols and then dialkoxylalkanes and carboxylic acids via dehydrogenation or sequential condensation steps [55, 56]. Methanol and isobutanol ODH turnover rates ($r_{methanol}$ and $r_{isobutanol}$) were measured at low conversions (< 5%). These measurements gave the expected high initial selectivities to the corresponding alkanals and slow formation of CO_2 (CO_2 < 9%, Table 2.4-2.6). Small amounts of condensation products (<7%), such as dimethoxymethane, diethoxyethane, and diisobutoxy isobutane also formed. Selectivities to formaldehyde, acetaldehyde, and isobutyraldehyde decreased with increasing reactant conversion (varied using residence time), as expected from their formation as primary products and the secondary reactions that they can undergo.

Methanol ODH turnover rates were slightly higher on SiO_2 than on LTA samples (by factors of 1.0–1.4, Table 2.4), possibly because of cluster size effects that make smaller clusters in LTA samples (Table 2.3) less reactive than larger clusters on SiO_2. These size effects reflect the higher binding of chemisorbed oxygen, the most abundant intermediate, on sites of lower coordination, which prevail on smaller clusters [55, 57]. Any effects of cluster size on reactivity would be expected to influence isobutanol ODH reactions similarly, which occur via a similar kinetically relevant step (H-abstraction from adsorbed alkanols or alkoxides by chemisorbed oxygen [54, 56]). Yet, isobutanol ODH turnover rates are much smaller on LTA than on SiO_2 samples (~20–160 times; Table 2.4), thus providing compelling evidence for the selective encapsulation of metal clusters in all LTA samples. These ODH rate measurements give encapsulation selectivities values much larger than unity (13.5–80.1 for methanol and isobutanol ODH (Table 2.4); Figure 2.5). These values reflect the much higher $\chi_{ODH,\ LTA}$ values measured on LTA samples (11.2–96.2, for methanol and isobutanol ODH (Table 2.4)) than on SiO_2 samples ($\chi_{ODH,\ SiO2}$ = 0.83–4.5, Table 2.4). These data, taken together with the size and uniformity of the metal clusters, provide evidence for the tendency of ligand-stabilized precursors to reside within the evolving zeolite structure, as such structures self-assemble during hydrothermal syntheses. These clusters reside predominantly within LTA crystals, where methanol, but not isobutanol, can access the catalytic surfaces of metal clusters.

2.3.2.2 Hydrogenation (HD) of Alkenes

Alkene hydrogenation reactions are much less sensitive than alkanol oxidation reactions to cluster size [24, 25] and are used here to confirm the conclusions reached based on ODH turnover rates. Alkene hydrogenation led to the exclusive formation of the corresponding alkane on all samples (Table 2.4). Isobutene cracking products were not detected, indicating that any residual acid sites are unreactive at these conditions. Pt/LTA gave a much higher χ_{HD} values ($\chi_{HD,\ LTA} = r_{ethene}/r_{isobutene}$, $\chi_{HD,\ LTA}$ = 15.8, Table 2.4) than Pt/SiO_2 ($\chi_{HD,\ SiO2}$ = 2.1, Table 2.4), consistent with selective encapsulation (ϕ_{HD} = 7.5, Table 2.4) and with the preferential encapsulation of Pt clusters within LTA voids. Pd/LTA and Rh/LTA also gave encapsulation selectivities (ϕ_{HD}) much larger than unity (8.3 and 82.9 respectively, Table 2.4 and Figure 2.5) confirming that Pd and Rh clusters also reside predominantly within LTA voids accessible only to the smaller ethene reactants. Ethene hydrogenation turnover rates were lower (by a factor of 1.2–2.9, Table 2.4) on LTA than on SiO_2 samples, apparently because access to metal clusters was restricted by diffusion

through LTA apertures or through residual opening around tight-fitting clusters, even for ethene at these low temperatures (294 K) [25].

These data, taken together with the shape selectivity in alkanol ODH reactions (Figure 2.5) and the mean diameter (Table 2.3), size uniformity (Figure 2.3), and stability against coalescence or sintering (Figure 2.4), suggest that metal clusters encapsulated within LTA via direct hydrothermal synthesis with ligand-stabilized metal precursors can select reactants based on molecular size and allow access to active sites only by reactants smaller than the interconnecting LTA windows

2.3.3 Protection of Metal Clusters from Contact with Larger Poisons during Catalysis

The oxidation and hydrogenation reactions show that LTA selectively sieves molecules based on size and prevents access to metal sites by molecules larger than the connecting LTA windows. Consequently, encapsulated clusters should also resist inhibition or poisoning by large molecules that bind strongly on cluster surfaces (e.g., organosulfur compounds) [16]. In this section, we provide evidence that LTA-encapsulated Pt and Rh clusters can be kept from contact with thiophene (0.46 nm kinetic diameter) [11], a titrant well-known to render metal surfaces unreactive for hydrogenation reactions.

Ethene hydrogenation rates were measured at 294 K on Pt/LTA and Rh/LTA and on the respective SiO_2-supported samples without thiophene and with 0.1 kPa thiophene (Figure 2.6). The small windows (0.41 nm × 0.41 nm) in LTA allow the diffusion of ethene and H_2 reactants, but hinder access by thiophene (kinetic diameter 0.46 nm) [11]. As a result, the addition of thiophene (0.1 kPa) to ethene-H_2 reactant mixtures decreased ethene hydrogenation rates to ~0.7 of its values before thiophene addition on LTA-encapsulated Pt and Rh clusters, but fully suppressed rates on both SiO_2-supported samples. This small decrease in hydrogenation rates upon thiophene addition on LTA-encapsulated Pt and Rh clusters reflects diffusional constraints imposed by reversible thiophene physisorption at external LTA surfaces or irreversible thiophene poisoning of metal clusters at unprotected external surfaces. The subsequent removal of thiophene led to the partial recovery of ethene hydrogenation turnover rates in M/LTA (M = Pt and Rh; Figure 2.6; to 0.75–0.80 of initial rates), but hydrogenation rates remained undetectable on SiO_2 samples even after the removal of thiophene. These data show that 0.75–0.80 fraction of the active metal surfaces ($f_{thiophene}$) reside within LTA voids, which are inaccessible to molecules larger than LTA apertures and are thus protected from contact with larger organosulfur compounds.

Encapsulation selectivities determined from alkene hydrogenation reactions (ϕ_{HD}) can also be used to infer the fraction of the measured rates arising from metal clusters residing within LTA voids ($f_{HD} = (\phi_{HD} - 1)/\phi_{HD}$) and to compare such values with those determined from the decrease in ethene hydrogenation upon titration of clusters at external LTA surfaces by thiophene ($f_{thiophene}$). f_{HD} values provide a lower limit for the fraction of the cluster surfaces residing within LTA crystals, where ethene, but not isobutene, can reach active sites. Even ethene, however, shows lower turnover rates on clusters dispersed on LTA than on SiO_2 (Table 2.4), apparently as a result of diffusional constraints, thus making ϕ_{HD} smaller than in the absence of such diffusional constraints. Therefore, f_{HD} values obtained from encapsulation selectivities are smaller than the actual fraction of active surfaces residing within LTA crystals and represent a lower limit for such

values. The values of f_{HD} on Pt/LTA and Rh/LTA are near unity (0.86 and 0.99 respectively), consistent with the nearly complete encapsulation of metal clusters within LTA voids and with $f_{thiophene}$ values (0.75 and 0.80, respectively).

These data and their mechanistic interpretation provide compelling evidence for selective encapsulation and for the general nature of the synthesis protocols reported in this study. The inhibition of premature precipitation of metal precursors and the self-assembly of LTA frameworks around stabilized precursors solvated as cationic species place such precursors, and ultimately the metal clusters derived from them, within confined spaces. As a result, LTA voids stabilize clusters against growth at treatment temperatures that sinter clusters of similar size on mesoporous supports, while also restricting access to active cluster surfaces by larger reactants or poisons.

2.4 Conclusions

Encapsulation of noble metal clusters (Pt, Pd, Rh, Ir, Re and Ag) within LTA voids was achieved by direct hydrothermal synthesis using ligand-stabilized metal precursors. The synthesis method developed here is based on the selection of appropriate ligands that prevent metal precursor precipitation by forming bulk oxyhydroxides during hydrothermal syntheses, thus allowing their inclusion in the synthesis gel, and promote the assembly of zeolite building units around the solvated ligand-stabilized cationic forms. These materials exhibited high shape selectivities in catalytic oxidative dehydrogenation of alkanols and in hydrogenation of alkenes. They also showed remarkable resistance against poisoning by organosulfur compounds having kinetic diameter larger than zeolite windows and also against thermal sintering because of confinement of metal clusters within zeolite voids. We expect that the present strategy of selective metal encapsulation using ligand-stabilized metal precursors can be extended further to zeolites of different frameworks, void environments and framework compositions and to clusters of other metals, metal oxides and metal sulfides of catalytic importance. These findings hold promise for the design and synthesis of catalysts for hydrotreating molecules in the presence of large heteroatom-containing compounds without poisoning active sites.

2.5 Acknowledgments

The authors gratefully acknowledges Dr. Zhijie Wu (China University of Petroleum, Beijing) for data collection and his technical and intellectual contributions to this work, Dr. Stacey I. Zones (Chevron; University of California at Berkeley) for technical advice and extensive discussions, Dr. George D. Meitzner for the technical review of this work and Chevron Energy Technology Company for the financial support of this research.

2.6 Figures, Tables and Scheme

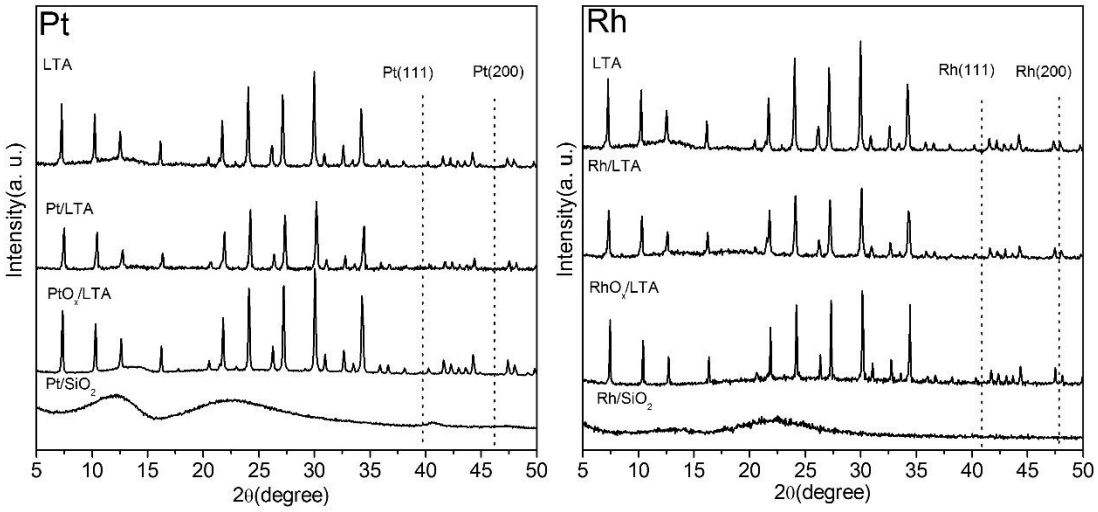

Figure 2.1 X-ray diffraction patterns of Pt and Rh containing LTA and SiO_2 samples.

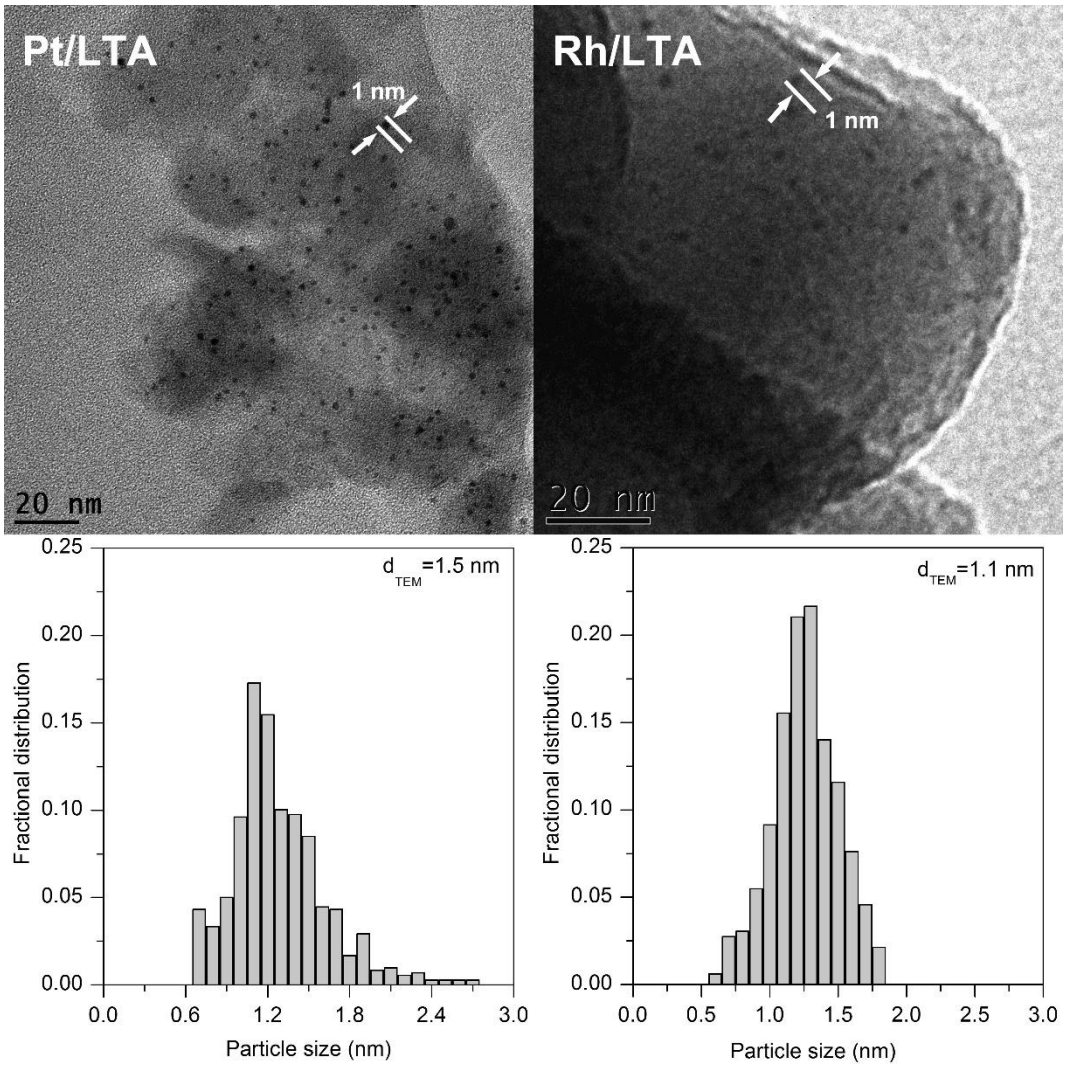

Figure 2.2 TEM images and metal cluster size distribution ($d_{TEM} = \sum n_i d_i^3 / \sum n_i d_i^2$) graphs of Pt/LTA and Rh/LTA samples.

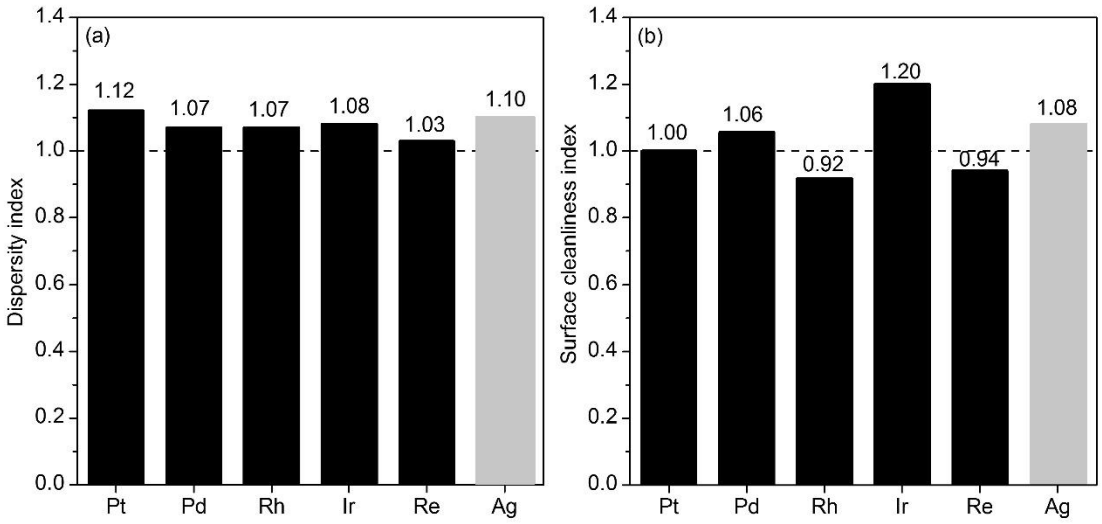

Figure 2.3 (a) Dispersity index of metal clusters from TEM characterization and (b) the surface cleanliness index of metal clusters from H_2 (bar in black) or O_2 (bar in gray) chemisorptions and TEM measurements in M/LTA samples (M= Pt, Pd, Rh, Ir, Re and Ag).

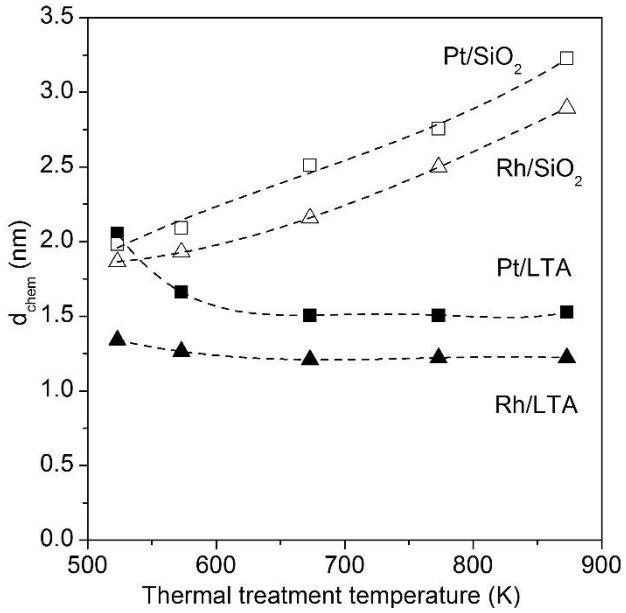

Figure 2.4 Effect of air treatment temperature on mean cluster diameter (estimated from the metal dispersion [24, 38]) of Pt and Rh containing LTA and SiO_2 samples.

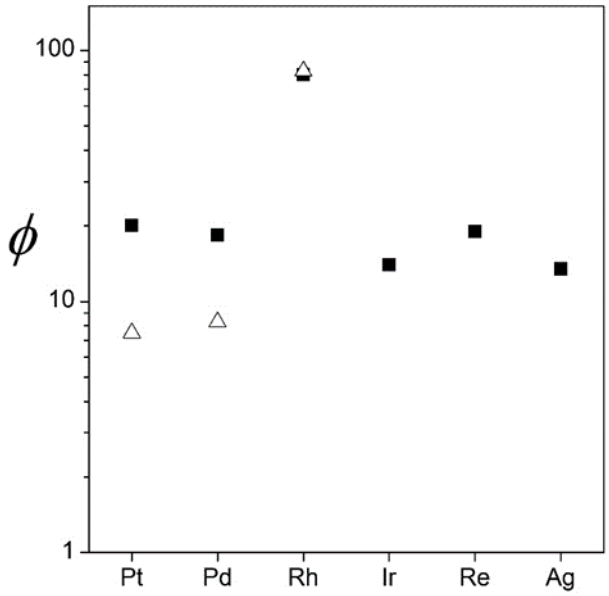

Figure 2.5 Encapsulation selectivity parameter (ϕ), reflecting the shape selectivity, of various M/LTA samples (M= Pt, Pd, Rh, Ir, Re, and Ag) for (i) selective oxidative dehydrogenation (ODH) of methanol and isobutanol (■) and (ii) selective hydrogenation of ethene and isobutene (△).

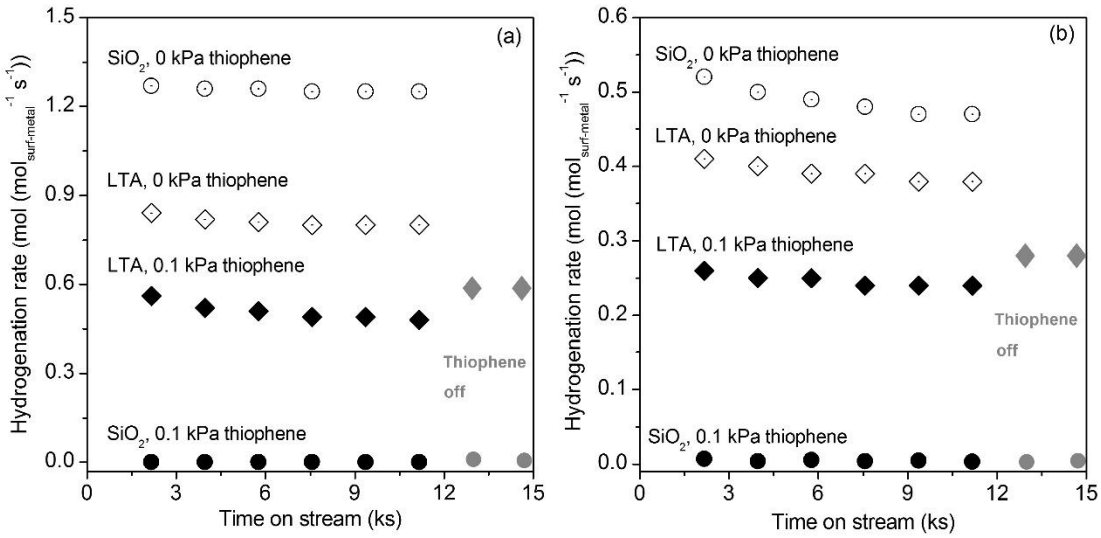

Figure 2.6 Ethene hydrogenation rates at 294 K (1.5 kPa ethene) for (a) Pt/LTA and Pt/SiO_2 and (b) Rh/LTA and Rh/SiO_2 samples in the presence (0.1 kPa) and absence of thiophene.

Table 2.1 Solubility product constants (K_{sp}) of metal hydroxides and solubility quotients (Q_c) of metal cations and hydroxide ions and solution behavior of various metal complexes at hydrothermal synthesis conditions in the absence of SiO_2.

Metal	Precursors (10^{-2} mol/L)	Solubility product constant (K_{sp}) of hydroxides at 298 K [a]	Solubility quotient (Q_c) at 298 K [b]	Behavior at zeolite synthesis conditions (in the absence of SiO_2)[c]
Pt	$Pt(NO_3)_2$	1.0×10^{-35}, $Pt(OH)_2$	1.5×10^{-5}	X
	$[Pt(NH_3)_4]\ (NO_3)_2$		**0.4×10^{-35}**	Y
Pd	$Pd(NO_3)_2$	1.0×10^{-31}, $Pd(OH)_2$	3.9×10^{-6}	X
	$[Pd(NH_2CH_2CH_2NH_2)_2]Cl_2$		**0.2×10^{-31}**	Y
Rh	$RhCl_3$	1.0×10^{-23}, $Rh(OH)_3$	4.8×10^{-6}	X
	$[Rh(NH_3)_5Cl]Cl_2$		2.1×10^{-22}	Z
	$[Rh(NH_2CH_2CH_2NH_2)_3]Cl_3$		**2.5×10^{-51}**	Y
Ir	**$[Ir(NH_3)_5Cl]Cl_2$**	3.3×10^{-64}, $Ir(OH)_3$	--	Y
Re	NH_4ReO_4	-, $Re(OH)_4$	--	X
	$[Re(NH_2CH_2CH_2NH_2)_2O_2]Cl$		--	Y
Ag	$AgNO_3$	2.0×10^{-8}, AgOH	3.1×10^{-5}	X
	$[Ag(NH_2CH_2CH_2NH_2)]NO_3$		**1.8×10^{-8}**	Y

[a] The K_{sp} for a metal hydroxide can essentially indicate whether precipitation will occur under conditions of metal cation and hydroxide ion concentration. If $Q_c < K_{sp}$, unsaturated solution of metal hydroxides, precipitate will not form; If $Q_c > K_{sp}$, supersaturated solution, sudden precipitation may occur when system is disturbed (shock, temperature changes etc.) [44-46]. K_{sp} for $Re(OH)_4$ was not available in literature because of rearrangement of rhenium hydroxides to rhenium oxo-hydrides [58].

[b] The concentration of hydroxide ions in the LTA zeolite gel is 0.17 mol L^{-1}, and the concentrations of various noble metals are 5.18×10^{-4} mol L^{-1} (Pt), 1.35×10^{-4} mol L^{-1} (Pd), 9.78×10^{-4} mol L^{-1} (Rh), 4.62×10^{-4} mol L^{-1} (Ir), 1.05×10^{-3} mol L^{-1} (Re) and 1.83×10^{-4} mol L^{-1} (Ag). Here, the solubility quotient (Q_c) has the same form as the solubility constant (K_{sp}) expression, but the concentrations of the substances are the free metal cations without bonded ligands (NH_3 or ethylenediamine) and hydroxide ions. The concentrations of metal cations without bonded ligands in metal precursors are calculated based on the stability constants of metal complexes using NH_3 or ethylenediamine as ligands [42, 47-50]. No complex stability values of $[Ir(NH_3)_5Cl]Cl_2$, NH_4ReO_4 and $[Re(NH_2CH_2CH_2NH_2)_2O_2]Cl$ have been reported in the literature.

[c] X = Precipitation < 10 s; Y = Clear solution without precipitate > 24 h; Z = Precipitation < 15 min.

Table 2.2 Initial molar ratios of constituents in synthesis gel of M/LTA samples.

Sample	Metal precursor used	Molar metal precursor	Na_2O	Al_2O_3	SiO_2	H_2O
Pt/LTA	$[Pt(NH_3)_4](NO_3)_2$	0.048	2.63	1.00	1.46	92.6
Pd/LTA	$[Pd(NH_2CH_2CH_2NH_2)_2]Cl_2$	0.017	2.63	1.00	1.46	125.0
Rh/LTA	$[Rh(NH_2CH_2CH_2NH_2)_3]Cl_3$	0.091	2.63	1.00	1.46	92.6
Ir/LTA	$[Ir(NH_3)_5Cl]Cl_2$	0.043	2.63	1.00	1.46	92.6
Re/LTA	$[Re(NH_2CH_2CH_2NH_2)_2O_2]Cl$	0.098	2.63	1.00	1.46	92.6
Ag/LTA	$[Ag(NH_2CH_2CH_2NH_2)]NO_3$	0.017	2.63	1.00	1.46	92.6

Table 2.3 Metal content, dispersion and mean cluster diameter of metal containing LTA and SiO_2 samples.

Sample	Metal loading (% wt.)[a]	Dispersion[b]	d_{chem}[c] (nm)	d_{TEM}[d] (nm)	Average fraction of α cages of LTA occupied by metal clusters[e] (%)	Average distance among metal clusters within LTA[f] (nm)
Pt/LTA	0.76	0.75	1.5	1.5	0.58	13.2
Pt/SiO_2	0.79	0.61	1.9	2.4	--	--
Pd/LTA	0.58	0.62	1.8	1.9	0.46	14.3
Pd/SiO_2	0.55	0.38	2.9	3.1	--	--
Rh/LTA	0.35	0.89	1.2	1.1	0.91	11.3
Rh/SiO_2	1.10	0.60	1.8	2.1	--	--
Ir/LTA	0.40	0.65	1.5	1.8	0.29	16.7
Ir/SiO_2	1.10	0.74	1.3	1.4	--	--
Re/LTA	0.63	0.78	1.7	1.6	0.35	15.7
Re/SiO_2	0.51	0.22	3.7	4.8	--	--
Ag/LTA	1.40	0.91	1.3	1.4	3.37	7.4
Ag/SiO_2	1.00	0.26	4.5	4.7	--	--

[a] Determined from inductively coupled plasma optical emission spectroscopy.

[b] Metal dispersion (D) estimated from H_2 (for Pt, Pd, Rh, Ir and Re) or O_2 chemisorption (for Ag) from $D= N_s/N_T$, where N_s is the total number of metal atoms present on the surface and N_T is the total number of metal atoms (surface and bulk).

[c] Mean cluster diameter estimated from the metal dispersion using $d_{chem} = 6\ (v_m/a_m)/D$ [39], where v_m is the bulk metal atomic density of Pt (15.10×10^{-3} nm^3), Pd (14.70×10^{-3} nm^3), Rh (13.78×10^{-3} nm^3), Ir (14.24×10^{-3} nm^3), Re (15.06×10^{-3} nm^3) and Ag (17.06×10^{-3} nm^3), and a_m is the surface area occupied by an atom on a polycrystalline surface of Pt (8.07×10^{-2} nm^2), Pd (7.93×10^{-2} nm^2), Rh (7.58×10^{-2} nm^2), Ir (7.73×10^{-2} nm^2), Re (6.60×10^{-2} nm^2) and Ag (8.75×10^{-2} nm^2) [39] metal.

[d] Surface-area-weighted mean cluster diameter (d_{TEM}) estimated from TEM analysis, $d_{TEM} = \sum n_i d_i^3 / \sum n_i d_i^2$ [39], the mean cluster diameter of metal supported on SiO_2 samples are quoted from reference [24].

[e] Average fraction (F) of α cages of LTA occupied by metal clusters calculated from the metal loading (L) and metal cluster diameter (d_{chem}) assuming spherical clusters, $F = \frac{\frac{M \times L}{4/3 \times \pi \times (d_{chem}/2)^3 \times \rho}}{\frac{M \times (1-L)}{M_{LTA}} \times N_A} \times 100\%$, where M is the weight of LTA samples, ρ is the mass density of metal (21.45, 12.02, 12.40, 22.42, 20.53, 10.50 g cm^{-3} for Pt, Pd, Rh, Ir, Re and Ag, respectively [39]), M_{LTA} is the molecular weight (17520 g mol^{-1}) of the ideal lattice ($[Na_{12}^+(H_2O)_{27}]_8\ [Al_{12}Si_{12}O_{46}]_8$) of LTA containing one α cage, and N_A is the Avogadro's constant (6.022×10^{23}).

[f] The average distance among metal clusters within LTA calculated from the average fraction (F) of α cages occupied by metal clusters, distance$=2 \times [(1/F) \times a^3]^{1/3}$, where a is the lattice parameter of LTA (1.19 nm) and homogeneous distribution of metal clusters in LTA zeolites was assumed.

Table 2.4 Alkanol oxidative dehydrogenation (ODH) and alkene hydrogenation (HD) turnover rates, relative reactivities of small and large reactants and encapsulation selectivity parameters for metal containing LTA and SiO_2 samples.[a]

Sample	Alkanol ODH reactions				Alkene HD reactions			
	$r_{methanol}$ (mol ($mol_{surf\text{-}metal}^{-1}$ s^{-1}))	$r_{isobutanol}$ (mol ($mol_{surf\text{-}metal}^{-1}$ s^{-1}))	$\chi_{ODH,j}$[b] j=LTA, SiO_2	ϕ_{ODH}[c]	r_{ethene} (mol ($mol_{surf\text{-}metal}^{-1}$ s^{-1}))	$r_{isobutene}$ (mol ($mol_{surf\text{-}metal}^{-1}$ s^{-1}))	$\chi_{HD,j}$[b] j=LTA, SiO_2	ϕ_{HD}[c]
Pt/LTA	0.53	0.016	32.2	20.1	0.81	0.051	15.8	7.5
Pt/SiO_2	0.56	0.35	1.6		1.30	0.61	2.1	
Pd/LTA	0.45	0.011	40.4	18.4	0.56	0.014	40.0	8.3
Pd/SiO_2	0.51	0.23	2.2		1.60	0.34	4.8	
Rh/LTA	0.025	0.00026	96.2	80.1	0.39	0.0084	46.4	82.9
Rh/SiO_2	0.049	0.042	1.2		0.47	0.84	0.56	
Ir/LTA	0.20	0.011	18.2	14.0				
Ir/SiO_2	0.19	0.15	1.3					
Re/LTA	0.072	0.00084	85.4	19.0				
Re/SiO_2	0.10	0.022	4.5					
Ag/LTA	0.027	0.0024	11.2	13.5				
Ag/SiO_2	0.029	0.035	0.83					

[a] Alkanol oxidative dehydrogenation rates were measured at 4 kPa alkanols and 9 kPa O_2 at 393 K (353 K for methanol ODH on Pt) and alkene hydrogenations at 1.5 kPa alkenes and 5 kPa H_2 at 294 K.

[b] $\chi_{ODH,\,j} = r_{methanol} / r_{isobutanol}$, j= LTA, SiO_2; $\chi_{HD,\,j} = r_{ethene}/r_{isobutene}$, j=LTA, SiO_2.

[c] For ODH reaction, $\phi_{ODH} = \chi_{ODH,\,LTA}/\chi_{ODH,\,SiO2}$; For HD reaction, $\phi_{HD} = \chi_{HD,\,LTA}/\chi_{HD,\,SiO2}$.

Table 2.5 Methanol ODH turnover rates and selectivities.[a]

Catalyst	Conversion (%)	$r_{methanol}$ (mol ($mol_{surf\text{-}metal}^{-1}$ s^{-1}))	Product selectivities (%)[b]				
			HCHO (formaldehyde)	MF	DMM	MMOH	CO_2
Pt/ LTA	2.7	0.53	80.1	4.5	4.2	2.3	8.9
Pt/SiO_2	2.4	0.56	84.0	7.5	1.4	0.3	6.8
Pd/LTA	3.1	0.45	80.4	11.8	0.1	0.6	7.1
Pd/SiO_2	1.6	0.51	90.2	2.4	0.6	1.7	5.1
Rh/ LTA	4.1	0.025	83.1	5.1	0.5	4.2	7.1
Rh/SiO_2	1.8	0.049	93.5	3.2	0.6	0.2	2.5
Ir/ LTA	1.8	0.20	91.4	2.9	0	3.2	2.5
Ir/SiO_2	2.2	0.19	55.2	30.9	6.2	1.2	6.5
Re/LTA	2.0	0.072	96.9	1.2	0	0	1.9
Re/SiO_2	1.8	0.10	93.6	2.1	0.3	0.2	3.8
Ag/LTA	2.2	0.027	89.6	5.7	0.4	1.1	3.2
Ag/SiO_2	1.8	0.029	73.4	20.0	0.6	0	6.0

[a] Methanol ODH rates were measured at 4 kPa methanol, 9 kPa O_2 and 393 K (353 K on Pt).
[b] MF - methyl formate (CH_3OCHO) ; DMM - dimethoxymethane ($CH_3OCH_2OCH_3$); MMOH-methoxy-methanol (CH_3OCH_2OH).

Table 2.6 Isobutanol ODH turnover rates and selectivities.[a]

Catalyst	Conversion (%)	$r_{isobutanol}$ (mol ($mol_{surf\text{-}metal}^{-1}$ s^{-1}))	Product selectivities (%)				
			i-C_3H_7CHO (isobutyraldehyde)	i-C_3H_7COOH (isobutyrate)	i-$C_3H_7COOC_4H_9$ (isobutyl isobutyrate)	i-$C_3H_7COC_4H_9OH$	CO_2
Pt/ LTA	1.2	0.016	85.7	10.3	0.4	1.1	2.5
Pt/SiO_2	1.4	0.35	77.6	18.3	0	1.4	2.7
Pd/ LTA	0.7	0.011	91.7	2.9	2.1	0.6	2.7
Pd/SiO_2	1.1	0.23	76.7	15.9	0.6	0.9	5.9
Rh/ LTA	0.5	0.00026	95.4	0.1	0.2	2.2	2.1
Rh/SiO_2	1.1	0.042	92.3	0.4	0.4	1.8	5.1
Ir/ LTA	1.2	0.16	87.5	1.2	1.2	5.2	4.9
Ir/SiO_2	2.0	0.15	88.8	0.7	0.5	4.1	5.9
Re/LTA	0.1	0.00084	99.7	0	0	0.3	0
Re/SiO_2	0.5	0.022	92.1	0.8	0.3	6.8	0
Ag/ LTA	1.3	0.0024	95.3	0.1	0	1.6	3.0
Ag/SiO_2	2.2	0.035	95.1	0.7	0.1	1.2	2.9

[a] Isobutanol ODH rates were measured at 4 kPa isobutanol, 9 kPa O_2 and 393 K.

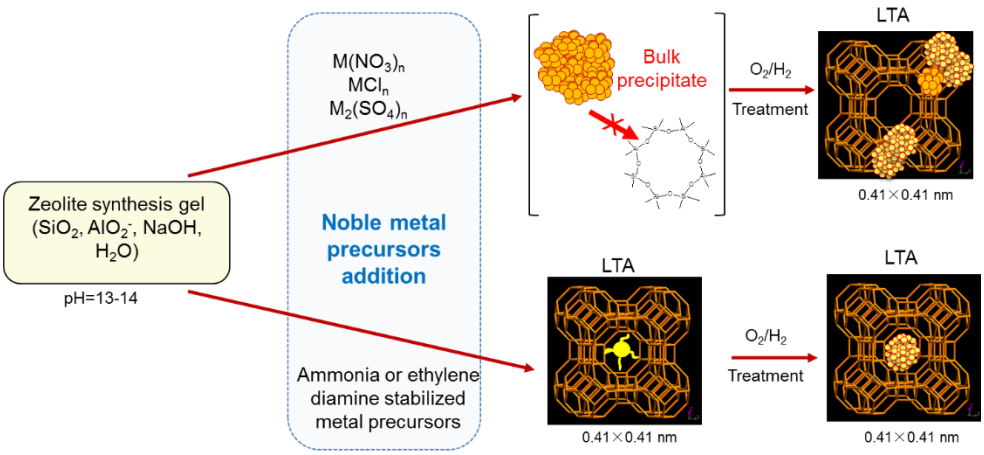

Scheme 2.1 Schematic of the process for encapsulation of metal clusters within LTA voids.

2.7 Supporting Information

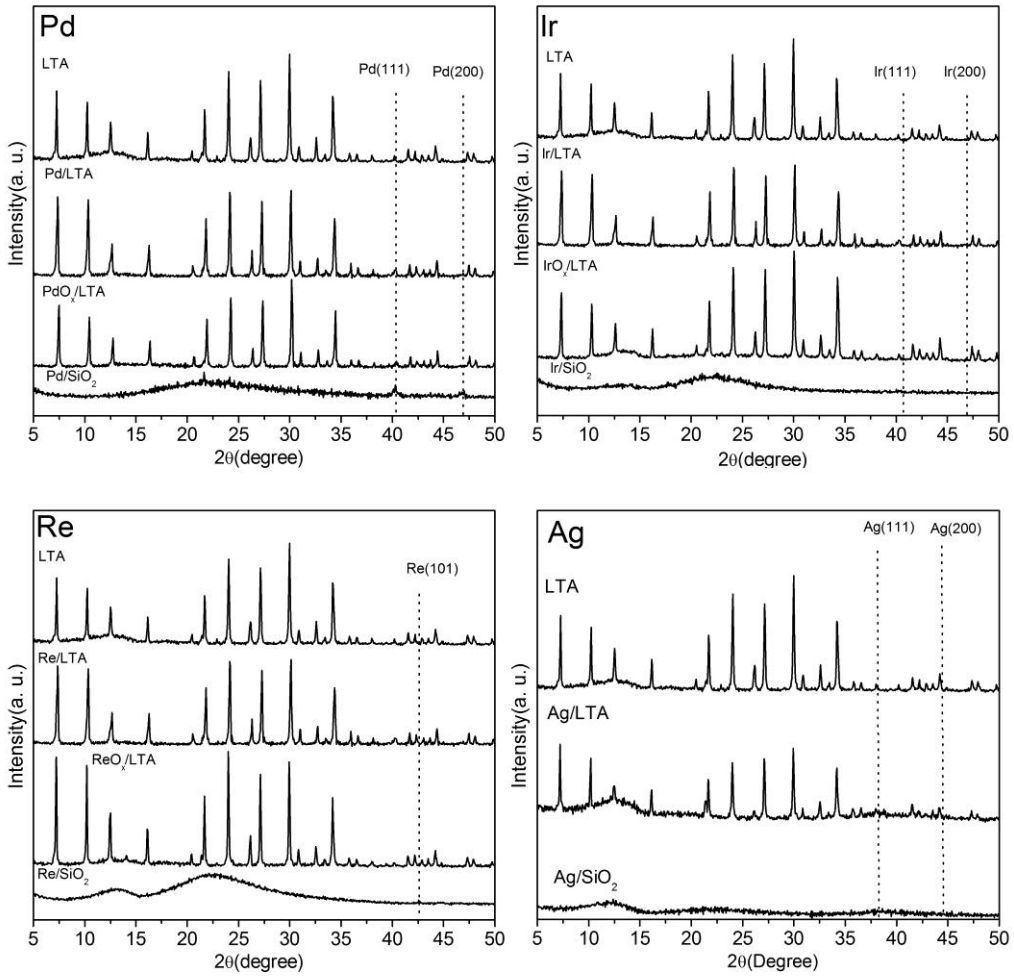

Figure 2.S1 X-ray diffraction patterns of metal (Pd, Ir, Re, and Ag) containing LTA and SiO_2 samples.

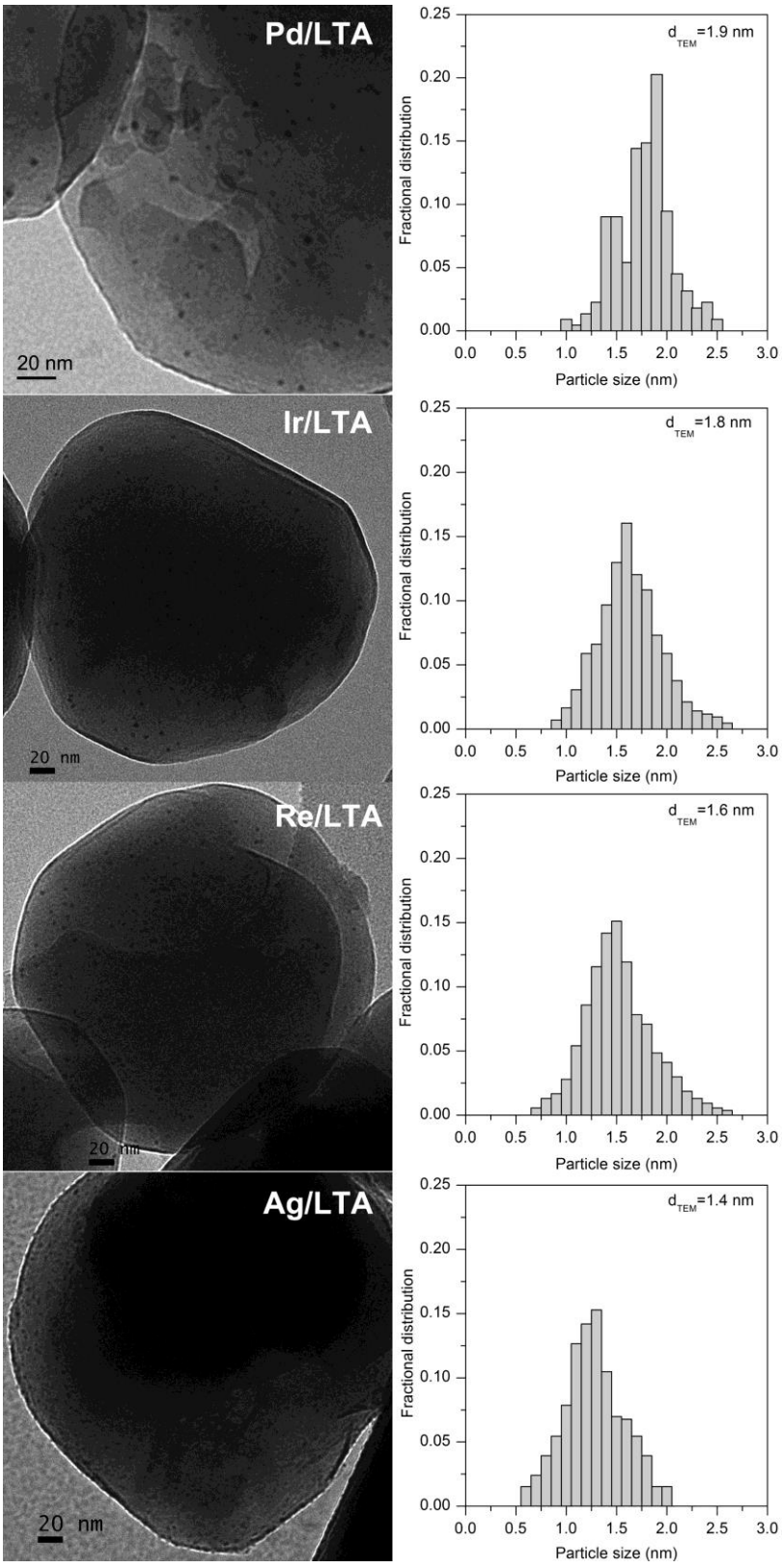

Figure 2.S2 TEM images and metal cluster size distribution graphs of M/LTA (M = Pd, Ir, Re, and Ag) samples ($d_{TEM} = \sum n_i d_i^3 / \sum n_i d_i^2$).

Rh/LTA samples synthesized using $RhCl_3$, $[Rh(NH_3)_5Cl]Cl_2$ and $[Rh(NH_2CH_2CH_2NH_2)_3]Cl_3$ as precursors ($Q_{c,[Rh(NH2CH2CH2NH2)3]Cl3} < K_{sp} < Q_{c,[Rh(NH3)5Cl]Cl2} << Q_{c,RhCl3}$, Tables 2.1 and 2.S1) gave very different ϕ_{ODH} values (1.1, 3.7 and 80.1 respectively). Close examination of the stability of rhodium complexes reveal that ~100% $RhCl_3$, ~96% $[Rh(NH_3)_5Cl]Cl_2$ and ~0% $[Rh(NH_2CH_2CH_2NH_2)_3]Cl_3$ (measured by ICP-AES) precursors precipitated at the temperature and pH conditions and the time frame of hydrothermal zeolite synthesis in the absence of silica. These data suggest that $RhCl_3$ precursors decomposed completely to form oxyhydroxides during zeolite crystallization which are too big to be contained within small cages of LTA zeolites. $[Rh(NH_3)_5Cl]Cl_2$ precursors were also unstable during zeolite synthesis and led to partially occluded metal (d_{TEM} = 4.8 nm, Figure S3) but $[Rh(NH_2CH_2CH_2NH_2)_3]Cl_3$ precursors did not decompose during zeolite synthesis (d_{TEM} = 1.1 nm, Figure 2.2).

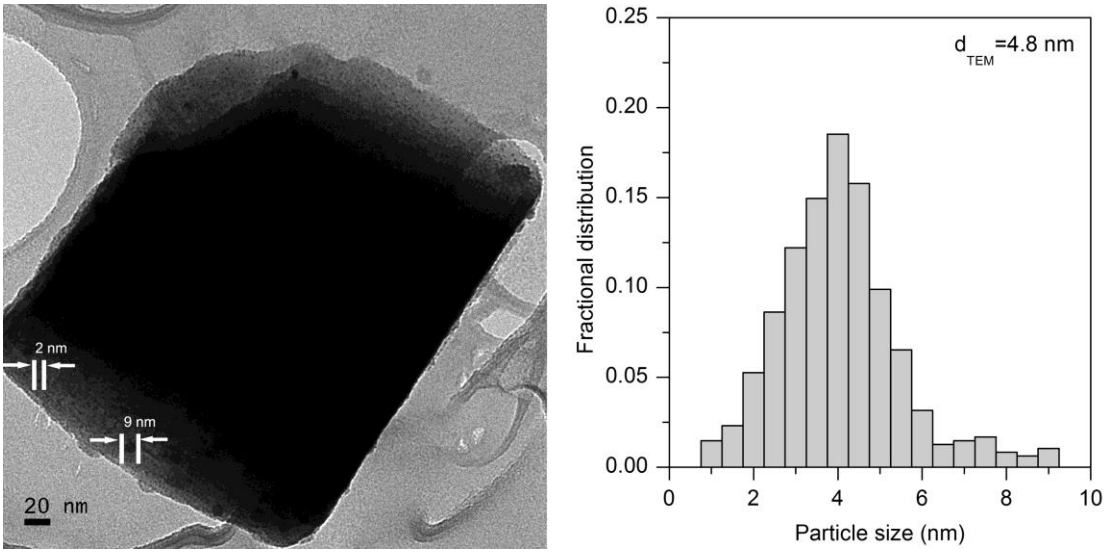

Figure 2.S3 TEM image and metal cluster size distribution graph of Rh/LTA ($d_{TEM} = \sum n_i d_i^3 / \sum n_i d_i^2$) synthesized using $[Rh(NH_3)_5Cl]Cl_2$ precursor.

Table 2.S1 Metal loading and dispersion of Rh/LTA samples synthesized using different precursors and their catalytic performance in alkanol ODH reaction.

Metal precursor	Metal loading (wt.%)	Metal dispersion	Alkanol ODH reactions [a]		
			$r_{methanol}$ (mol ($mol_{surf\text{-}metal}^{-1}$ s^{-1}))	$r_{isobutanol}$ (mol ($mol_{surf\text{-}metal}^{-1}$ s^{-1}))	ϕ_{ODH} [b]
$RhCl_3$	1.00	0.15	0.047	0.037	1.1
$[Rh(NH_3)_5Cl]Cl_2$	1.10	0.28	0.035	0.0079	3.7
$[Rh(NH_2CH_2CH_2NH_2)_3]Cl_3$	0.35	0.89	0.025	0.00026	80.1

[a] Oxidative dehydrogenation reactions were measured at 4 kPa methanol, 9 kPa O_2 and 393 K.

[b] $\chi_{ODH,i} = r_{methanol} / r_{isobutanol}$, i=LTA, SiO_2, $\phi_{ODH} = \chi_{ODH,\ LTA}/\chi_{ODH,\ SiO2}$.

2.8 References

(1) Sachtler, W.M.H. *Acc. Chem. Res.* 1993, 26, 383.
(2) Gallezot, P.; Moskovits M., Ed. *Metal Cluster;* J. Wiley & Sons, 1986, pp 219–247.
(3) Gallezot, P. *Post-Synthesis Modification I* 2002, 257.
(4) Sachtler, W.M.H.; Zhang, Z. *Adv. Catal.* 1993, 39, 129.
(5) Uzun, A.; Gates, B.C. *Angew. Chem. Int. Ed.* 2008, 47, 9245.
(6) Weisz, P.B.; Frilette, V.J.; Maatman, R.W.; Mower, E.B. *J. Catal.* 1962, 1, 307.
(7) Frilette, V.J.; Maatman, R.W. US Patent 3373109, 1968.
(8) Junguin, B.; Clement, C.; Leprince, P.; Montaranl, R. *Bull. Soc. Chim. Fr.* 1966, 7, 709.
(9) Ohgoshi, S.; Nakamura, I.; Wakushima, Y. *Stud. Surf. Sci. Catal.* 1993, 77, 289.
(10) Miller, J.T.; Pei, S.Y. *Appl. Catal. A* 1998, 168, 1.
(11) Yang, H.; Chen, H.; Chen, J.; Omotoso, O.; Ring, Z. *J. Catal.* 2006, 243, 36.
(12) Yang, H.; Chen, H.; Du, H.; Hawkins, R.; Craig, F.; Ring, Z.; Omotoso, O.; Munoz, V.; Mikula, R. *Micropor. Mesopor. Mater.* 2009, 117, 33.
(13) Küehl, G.H. US Patent 4191663, 1980.
(14) Chen, S.; Chen, J.; Gieleciak, R.; Fairbridge, C.; *Appl. Catal. A* 2012, 415–416, 70.
(15) Jacobs, P.A.; Tielen, M.; Martens, J. *J. Mol. Catal.* 1984, 27, 11.
(16) Zhan, B.Z.; Iglesia, E. *Angew. Chem. Int. Ed.* 2007, 46, 3697.
(17) Zhan, B.Z.; White, M.A.; Sham, T.K.; Pincock, J.A.; Doucet, R.J.; Rao, K.V.R.; Robertson, K.N.; Cameron, T.S. *J. Am. Chem. Soc.* 2003, 125, 2195.
(18) Altwasser, S.; Gläser, R.; Lo, A.S.; Liu, P.H.; Chao, K.J.; Weitkamp, J. *Micropor. Mesopor. Mater.* 2006, 89, 109.
(19) Rossin, J.A.; Davis, M.E. *J. Chem. Soc., Chem. Commun.* 1986, 234.
(20) Davis, R.J.; Rossin, J.A.; Davis, M.E. *J. Catal.* 1986, 98, 477.
(21) Wu, J.C.S.; Goodwin, J.G.; Davis, M. *J. Catal.* 1990, 125, 488.
(22) Davis, M.E.; Saldarriaga, G.; Rossin, J.A. *J. Catal.* 1987, 103, 520.
(23) Laursen, A.B.; Højholt, K.T.; Lundegaard, L.F.; Simonsen, S.B.; Helveg, F.; Schüth, S.; Paul, M.; Grunwaldt, J.D.; Kegnæs, S.; Christensen, C.H.; Egeblad, K. *Angew. Chem. Int. Ed.* 2010, 19, 3504.
(24) Choi, M.; Wu, Z.; Iglesia, E. *J. Am. Chem. Soc.* 2010, 132, 9129.
(25) Goel, S.; Wu, Z.; Zones, S.I.; Iglesia, E. *J. Am. Chem. Soc.* 2012, 134, 17688.
(26) Balkus Jr., K.J.; Gabrielov, A.G. J. *Inclusion Phenom. Mol. Recognit. Chem.* 1995, 21, 159.
(27) Balkus Jr., K.J.; Hargis, C.D.; Kowalai, S. *ACS Symp. Ser.* 1992, 499, 347.
(28) Salama, T.M.; Ali, I.O.; Hanafy, A.I.; Al-Meligy, W.M. *Mater. Chem. Phys.* 2009, 113, 159.
(29) Rankel, L.A.; Valyocsik, E.W. US Patent 4388285, 1983.
(30) Boucheffa, Y.; Thomazeau, C.; Cartraud, P.; Magnoux, P.; Guisnet, M. *Ind. Eng. Chem. Res.* 1997, 36, 3198.
(31) Van Mao, R.L.; Nguyen, T.M.; Mclaughlin, G.P. *Appl. Catal.* 1989, 48, 265.
(32) Triebe, R.W.; Tezel, F.H.; Khulbe, K.C. *Gas Sep. Purif.* 1996, 10, 81.
(33) Jiao, L.; Regalbuto, J.R. *J. Catal.* 2008, 260, 329.
(34) Paryjczak, T.; Gebauer, D. *J. Colloid Interface Sci.* 1979, 72, 181.
(35) Aben, P.C. *J. Catal.* 1968, 10, 224.
(36) Hoost, T.E.; Kudla, R.J.; Collins, K.M.; Chattha, M.S. *Appl. Catal. B* 1997, 13, 59.

(37) Mcvicker, G.B.; Baker, R.T.K.; Garten, R.L.; Kugler, E.L. *J. Catal.* 1980, 65, 207.
(38) Yates, D.J.C.; Sinfelt, J.H. *J. Catal.* 1969, 14, 182.
(39) Bergeret, G.; Gallezot, P. In *Handbook of Heterogeneous Catalysis;* Wiley-VCH Verlag GmbH & Co. KgaA: New York, 2008.
(40) Schneider, M.; Duff, D.G.; Mallat, T.; Wildberger, M.; Baiker, A. *J. Catal.* 1994, 147, 500.
(41) Rossi, L.M.; Nangol, I.M.; Costa, N.J.S. *Inorg. Chem.* 2009, 48, 4640.
(42) Paoletti, P. *Pure Appl. Chem.* 1984, 56, 491.
(43) Zhu, H.; Liang, C.; Yan, W.; Overbury, S.H.; Dai, S. *J. Phys. Chem. B* 2006, 110, 10842.
(44) Hawke, S.J. *J. Chem. Educ.* 1998, 75, 1179.
(45) Speight J.G., Ed. *Lange's Handbook of Chemistry*; McGRAW-HILL, 2005, pp 1.331-1.342.
(46) Juodkazyte, J.; Sebeka, B.; Valsiunas, I.; Juodkazis, K. *Electroanalysis* 2005, 17, 947.
(47) House J.E., Ed. *Inorganic Chemistry*; Elsevier, 2008, pp 671–685.
(48) Housecroft, C.E.; Sharpe A.G., Eds. *Inorganic Chemistry*; Pearson Prentice Hall, 2005, pp 171–185.
(49) Kaas, K.; Springborg, J. *Inorg. Chem.* 1987, 26, 387.
(50) Skibsted, L.H.; Ford, P.C. *Acta Chem. Scand. A* 1980, 34, 109.
(51) Gilbert, R.G.; Hess, M.; Jenkins, A.D.; Jones, R.G.; Kratochvíl, P.; Stepto, R.F.T. *Pure Appl. Chem.* 2009, 81, 351.
(52) Jaeger, N.I.; Schulz-Ekloff, G.; Ryder, P. *Stud. Surf. Sci. Catal.* 1984, 18, 299.
(53) Gallezot, P.; Alarcon-Diaz, A.; Dalmon, J.A.; Renouprez, A.J.; Imelik, B. *J. Catal.* 1975, 39, 334.
(54) Gallezot, P.; Bergeret, G. *J. Catal.* 1981, 72, 294.
(55) Liu, H.C.; Iglesia, E. *J. Phys. Chem. B* 2005, 109, 2155.
(56) Louis, C.; Tatibout, J.M.; Che, M. *J. Catal.* 1988, 109, 354.
(57) Lichtenberger, J.; Lee, D.; Iglesia, E. *Phys. Chem. Chem. Phys.* 2007, 9, 4902.
(58) Tahmassebi, S.K.; Conry, R.R.; Mayer, J.M. *J. Am. Chem. Soc.* 1993, 115, 7553.

Chapter 3

Synthesis and Catalytic Properties of Metal Clusters Encapsulated within Small-Pore (SOD, GIS, ANA) Zeolites

Abstract

The synthesis protocols for encapsulation of metal clusters reported here expand the diversity in catalytic chemistries made possible by the ability of microporous solids to select reactants, transition states, and products based on their molecular size. We report a synthesis strategy for the encapsulation of noble metals and their oxides within SOD (Sodalite, 0.28 nm x 0.28 nm), GIS (Gismondine, 0.45 nm x 0.31 nm) and ANA (Analcime, 0.42 nm x 0.16 nm) zeolites. Encapsulation was achieved via direct hydrothermal synthesis for SOD and GIS using metal precursors stabilized by ammonia or organic amine ligands, which prevent their decomposition or precipitation as colloidal hydroxides at the conditions of hydrothermal synthesis (< 380 K) and favor interactions between metal precursors and incipient aluminosilicate nuclei during self-assembly of microporous frameworks. The synthesis of ANA requires higher crystallization temperatures (~ 415 K) and high pH (> 12), thereby causing precipitation of even ligand-stabilized metal precursors as hydroxides. As a result, encapsulation was achieved by the recrystallization of metal clusters containing GIS into ANA, which retained these metal clusters within voids throughout the GIS-ANA transformation.

3.1 Introduction

Encapsulation of metal and oxide clusters within zeolites [1-5] can protect such clusters against sintering and also prevent their contact with toxic impurities, while concurrently allowing active sites to select reactants and transition states based on molecular size [6-10]. The confinement of such clusters within small-pore zeolites (<0.45 nm apertures) cannot be achieved via post-synthesis exchange from aqueous or vapor media, because the size of cationic or anionic precursors, with their charge-balancing double layer, and of gaseous complexes prevents their diffusion through the apertures in these microporous aluminosilicates. In these materials, encapsulation requires that precursors be placed and retained within microporous frameworks during hydrothermal syntheses and subsequent thermal treatment [9, 11]. The high pH (>12) conditions required for hydrothermal crystallization of zeolites typically cause the precipitation of such precursors as colloidal metal hydroxides larger than the zeolite voids [12], thus preventing their encapsulation. Organic amines and NH_3 ligands can stabilize metal cations and prevent premature precipitation; they can also act as coordinating agents to encourage the sequestering of precursors during the incipient formation of aluminosilicate frameworks [13].

Hydrothermal synthesis of zeolites proceeds via three steps: induction, nucleation and crystallization [14]. The framework building units are denoted as the ‘host’ and the external component as the ‘guest’. Zeolite nucleation and crystallization hinges on a balance of guest-host assembly with the guest stabilizing the surrounding zeolite framework [15]. The ligand-stabilized metal cationic complexes used here are hydrophilic and are very effective in templating Al-rich zeolites (Sodalite (SOD), Analcime (ANA) and Gismondine (GIS)) [16] during hydrothermal

synthesis, in contrast with Si-rich zeolites, which require hydrophobic organo-cations as stabilizing guests and structure-directing agents [17].

We present here synthetic protocols for the encapsulation of active metals within zeolites with small voids (SOD, GIS and ANA, Figure 3.1) and show that such zeolite structures can protect Pt, Pd, Ru and Rh clusters against sintering and from contact with larger molecules that block active surfaces. These data also provide chemical and structural evidence for confinement and for the consequences of encapsulation on catalytic rates and selectivity. Precursor stabilization during synthesis proved infeasible for ANA because of the high temperatures required for its crystallization (~ 415 K). GIS structures already containing reduced metal clusters were instead converted into ANA via local recrystallization processes that retained metal clusters within ANA crystals.

Encapsulation and phase purity were established using X-ray diffraction, transmission electron microscopy, and titration methods. Oxidative dehydrogenation (ODH) of methanol (kinetic diameter 0.37 nm) and isobutanol (kinetic diameter 0.55 nm), hydrogenation of ethene (kinetic diameter 0.39 nm) and toluene (kinetic diameter 0.59 nm), and ethene hydrogenation in the presence and absence of thiophene (kinetic diameter 0.46 nm) were used to confirm encapsulation and to establish the ability of metal-containing GIS and ANA catalysts to select reactants based on size and to protect active sites from large organosulfur poisons. H_2-D_2 (kinetic diameter 0.28 nm) isotopic exchange in the presence and absence of H_2S (kinetic diameter 0.36 nm) was used to probe the ability of metal containing SOD to activate dihydrogen without interference by H_2S.

3.2 Results and Discussion

The direct encapsulation of metal precursors during hydrothermal synthesis requires interactions between metal precursors and incipient aluminosilicate frameworks, which are favored by cationic metal complexes because of the anionic nature of aluminosilicate building blocks [11]. Encapsulation requires the self-assembly of these building blocks around solvated cations [12]. At the high pH (>12) of hydrothermal syntheses, these cations precipitate prematurely as colloidal hydroxides (Supporting Information Table 3.S1, precipitation time for metal precursors in alkaline solution) that cannot be contained within the voids in incipient aluminosilicate frameworks, thus preventing encapsulation. Ammonia and ethylene diamine ligands stabilize cationic precursors and prevent their precipitation, even at higher pH (up to ~13) and temperatures above ambient (up to ~390 K). Additionally, these ligands can act as tethers between cationic complexes and the emerging aluminosilicate moieties that ultimately assemble into zeolite frameworks, thus favoring the inclusion of metal precursors within SOD and GIS zeolite voids as they form. ANA requires higher temperature (~415 K) for crystallization, which leads to rapid formation of metal hydroxides even when metal precursors are stabilized by ligands (Figure 3.S1, Supporting Information). The synthesis of ANA involves the initial formation of GIS, which then converts to ANA [18]. These observations led us to attempt the recrystallization of metal encapsulated within GIS (M/GIS) into metal encapsulated within ANA (M/ANA) while retaining metal clusters within crystallites.

3.2.1 Structural Evidence for Zeolite Phase and for Confinement and Surface Cleanliness of Metal and Oxide Clusters. X-ray diffraction (XRD) patterns for metal-containing zeolites (M/SOD, M/GIS and M/ANA) (Figure 3.2) showed lines corresponding to crystalline forms of the intended zeolite structures, indicating that ligated precursors did not interfere with hydrothermal crystallization processes. Transmission electron micrographs (TEM) for M/GIS and high angle annular dark field scanning transmission electron micrographs (HAADF STEM) (Figure 3.3) after reduction of precursors and passivation of metal clusters showed that they were present as small clusters uniform in size and distributed throughout zeolite crystallites. The metal clusters in SOD were not visible by TEM, but HAADF STEM images show the presence of small clusters (1.0-1.5 nm, Figure 3.3) in Pt/SOD.

H_2 uptakes gave metal dispersions of 0.63-0.70 for Pt, Pd, Ru, and Rh clusters in GIS, 0.50-0.61 for Pt and Ru in ANA, and 0.22-0.39 for Pt, Pd, Ru, and Rh in SOD (Table 3.1) after thermal treatment at 573 K. The dispersion values obtained from H_2-chemisorption in SOD samples are small compared to the values expected on the basis of electron microscopy due to the limited access of even hydrogen to active sites tightly contained within small aperture SOD cages. The agreement between surface-averaged mean diameters from electron micrographs in M/GIS (M = Pt, Pd, Ru, and Rh) and Pt/ANA and those determined from H_2 chemisorption uptakes (assuming spherical clusters; Figure 3.3) indicates that all clusters detectable by microscopy exhibit clean surfaces accessible to these titrants and that the ligands present during hydrothermal synthesis are removed by the thermal treatments used. We conclude from these data that metal clusters surfaces are available for catalytic reactions of any reactants that can diffuse through the microporous frameworks in GIS and ANA zeolites at rates commensurate with those of the surface-catalyzed chemical reactions.

3.2.2 Catalytic Evidence for Encapsulation: Oxidative Dehydrogenation of Methanol and Isobutanol and Hydrogenation of Ethene and Toluene on GIS- and ANA-Supported Catalysts. The molecular dimensions of GIS and ANA apertures allow them to sieve reactants and products based on size, while the intervening intracrystal voids can stabilize specific transition states that maximize their van der Waals contacts with the framework. Oxidative dehydrogenation (ODH) rates of methanol [19] and isobutanol (0.37 nm and 0.55 nm respective kinetic diameter) and hydrogenation of ethene and toluene (0.39 nm and 0.59 nm respective kinetic diameters) were used to confirm the predominant presence of Pt, Pd, Ru and Rh clusters within GIS (0.45 nm x 0.31 nm aperture) and of Pt and Ru clusters within ANA (0.42 nm x 0.16 nm aperture). Methanol and ethene, but not isobutanol and toluene, can access sites encapsulated within GIS or ANA zeolite crystals via diffusion through their interconnected voids and apertures.

The selectivity of encapsulation processes during hydrothermal synthesis was assessed by first measuring the ratio of ODH and hydrogenation rates for the small and large reactants on unconstrained clusters dispersed on SiO_2 ($\chi_{ODH\text{-}SiO_2} = r_{methanol}/r_{isobutanol}$, $\chi_{HYD\text{-}SiO_2} = r_{ethene}/r_{toluene}$) to determine the relative reactivity of the two molecules on unconstrained systems; similar data for the same metal in zeolite samples ($\chi_{i,zeolite}$, i = ODH, HYD) allows the ratio of these relative reactivities to be expressed as an encapsulation selectivity parameter ($\phi = \chi_{i,zeolite}/\chi_{i,SiO_2}$, i = ODH, HYD) for each reaction and reactant pair. This ratio represents a direct measure of the diffusional constraints imposed on larger reactants by the presence of metal clusters within zeolite structures; it is therefore a rigorous indicator of the extent to which the active surfaces are contained within

the microporous networks. This encapsulation selectivity parameter would approach unity for clusters with unimpeded access to reactants, such as those at external zeolite surfaces. Values of ϕ provide the functional definition of the effectiveness of synthetic protocols, as well as the mechanistic and practical manifestation of reactant shape selectivity; values larger than ~5 are taken here as evidence of successful encapsulation.

M/GIS and M/ANA samples gave much larger $\chi_{ODH,zeolite}$ and $\chi_{HYD,zeolite}$ values than for the respective metals dispersed on SiO_2 (Table 3.2, 3.3) and high encapsulation selectivities (ϕ = 8-83, Figure 3.4) for both ODH and hydrogenation reactions, indicating that active sites on these zeolites indeed reside predominantly within locations accessible only to the smaller methanol and ethene reactants. Methanol ODH and ethene hydrogenation turnover rates (per exposed metal atom determined from chemisorption uptakes) were smaller on metals dispersed on GIS and ANA than on SiO_2, indicating that even for small ethene and methanol molecules access to active surface is restricted by diffusion through the zeolite aperture or by limited access to the surface clusters tightly contained within zeolite cages.

3.2.3 Catalytic Evidence for the Protection of Active Sites from Large Sulfur Poisons: Hydrogenation of Ethene in the Presence and Absence of Thiophene in GIS- and ANA-Supported Catalysts. The diffusional constraints that restrict access to active sites by larger reactants also serve to prevent contact between encapsulated metal clusters and larger organosulfur poisons, such as thiophene, which titrate surface atoms and render them unreactive. These expectations were confirmed by measuring ethene (0.39 nm kinetic diameter) hydrogenation rates on Pt/GIS and Pt/ANA and on the respective metals dispersed on SiO_2 in the presence and absence of thiophene (0.46 nm kinetic diameter; 0.4 kPa) (Figure 3.5), an organosulfur titrant that cannot readily diffuse through the small apertures in GIS and ANA.

The addition of thiophene (0.4 kPa) to the reactants decreased ethene hydrogenation rates by a factor of 13 in Pt/GIS, 7 in Pt/ANA and 530 in Pt/SiO_2. After thiophene addition was stopped, ethene hydrogenation rates recovered to 0.85 of initial rate in Pt/GIS and 0.70 in Pt/ANA (Figure 3.5). In sharp contrast, metal clusters dispersed on SiO_2 did not show any detectable increase in hydrogenation rates after removal of thiophene from ethene-H_2 feed. The lower rates observed on Pt/ANA and Pt/GIS after thiophene addition appear to reflect the combined effects of titration of external clusters and diffusional constraints on ethene reactants imposed by thiophene physisorbed on external zeolite surfaces and blocking the zeolite aperture; the latter effects are reversible and disappear upon removal of thiophene.

The essential retention of ethene hydrogenation rates for metal clusters on GIS and ANA zeolites after stopping thiophene confirms that 0.70-0.85 fraction of the active metal cluster surfaces resides within GIS and ANA structures, where such active sites cannot contact the organosulfur compound.

3.2.4 Evidence of Encapsulation and Protection of Active Sites from Toxic Sulfur Compounds: H_2-D_2 Exchange Rates on SOD-Supported Catalysts. The smaller apertures in SOD (0.28 nm) allow the diffusion of H_2 (0.28 nm kinetic diameter) and D_2 (0.28 nm kinetic diameter), but few other molecules [20]. The protection of active sites from H_2S (0.36 nm kinetic diameter) was demonstrated by measuring the H_2-D_2 exchange rates at 373 K in the absence and

presence of H_2S (1 kPa) on Pt, Pd, Ru, and Rh clusters dispersed on SOD and the same metal clusters dispersed on SiO_2.

The addition of H_2S to H_2-D_2 decreased H_2-D_2 exchange rates by a factor of 2.7-9.9 on SiO_2-supported metals, as expected from the titration of exposed surface atoms by sulfur moieties derived from H_2S. In contrast, isotopic exchange rates decreased by much smaller factors (1.3-1.5) on M/SOD samples when H_2S (1 kPa) was present in H_2-D_2 reactants (Figure 3.6). Residual H_2-D_2 exchange rates on SiO_2-supported clusters in the presence of H_2S (Figure 3.6) reflect exchange rates on S-containing surfaces, including exchange between H-atoms from H_2S and D-atoms in D_2. H_2S inhibition of exchange rates in M/SOD reflects the combined effects of irreversible titration of external clusters by chemisorbed sulfur species and reversible H_2S physisorption at external SOD surfaces, which interferes with the diffusion of dihydrogen isotopes. The latter effect is reversible upon removal of H_2S from the H_2-D_2 reactants and leads to the partial recovery of exchange rates (Figure 3.6). The residual rates after H_2S removal rigorously reflect the rates on encapsulated surfaces on M/SOD samples never exposed to H_2S. H_2S removal from H_2-D_2 did not lead to any changes in exchange rates on unprotected clusters dispersed on SiO_2, because inhibition reflects only the titration of active metal surfaces without additional contributions from diffusional effects.

The exchange rates on M/SOD were corrected by rate measured on M/SiO_2 in the presence of H_2S to obtain the rate coming solely from H_2-D_2 exchange on metal clusters encapsulated within SOD framework. These calculations show that a large fraction of the active surfaces (0.64-0.79 fraction) are protected from H_2S in M/SOD samples, apparently because such surfaces reside within SOD crystals that are inaccessible to H_2S. These data show that encapsulated clusters within SOD can be effectively protected against all sulfur poisons, while concurrently demonstrating the high encapsulation selectivity achieved.

3.2.5 Practical Implications. Metal clusters encapsulated within ANA and GIS provide practical catalysts for the selective hydrogenation-dehydrogenation of linear hydrocarbons and oxygenates over branched or cyclic analogs as evidenced from selective oxidative dehydrogenation of methanol and isobutanol and selective hydrogenation of ethene and toluene (Figure 3.4). These catalysts can also very effective prevent inhibition of these reactions by larger and more strongly bound species, such as arenes and organosulfur compounds, as evidenced by the protection of active sites from thiophene poisons in ethene hydrogenation (Figure 3.5). The SOD-encapsulated clusters can potentially extract H_2 via dissociative adsorption from streams containing H_2S at ambient temperatures and subsequent desorption during temperature cycling. These materials reversibly chemisorb H_2 (Table 3.1) and retain their ability to do so in the presence of H_2S during H_2-D_2 exchange reactions (Figure 3.6).

3.3 Conclusion

Encapsulation of noble metals (Pt, Pd, Ru, and Rh) was achieved within small-pore zeolites (SOD and GIS) via direct hydrothermal synthesis using ligands that prevent precipitation as colloidal hydroxides at the high pH required for zeolite crystallization. ANA-encapsulated clusters were prepared by post-synthesis recrystallization of their metal-containing GIS analogs, because the high temperature required for direct ANA synthesis decomposed even ligand-protected

precursors. The relative rates of oxidative dehydrogenation of methanol and isobutanol and of hydrogenation of ethene and toluene on metals clusters in GIS, ANA, and SiO_2 and the similar cluster sizes inferred from chemisorption and TEM show that surfaces of metal clusters are clean and reside predominantly with GIS and ANA, where they are accessible only to the smaller reactants. These conclusions were further confirmed by the ability of these materials to catalyze ethene hydrogenation in the presence of thiophene poisons. Thus, metal clusters encapsulated within ANA and GIS provide effective catalysts for the selective hydrogenation-dehydrogenation of reactants smaller than zeolite apertures over larger ones while protecting the active surfaces from large organosulfur poisons which irreversibly bind the active surfaces. H_2-D_2 exchange rates in the presence of H_2S were much higher on M/SOD than on M/SiO_2, consistent with preferential encapsulation of metal clusters within voids protected from H_2S, making these materials potentially useful to extract H_2 via dissociative adsorption from sulfur-contaminated streams.

3.4 Experimental Section

3.4.1 Materials. Fumed SiO_2 (0.014 μm, 200 ± 25 $m^2 g^{-1}$, Sigma,), $NaAlO_2$ (anhydrous, Riedel-de Haën, technical), NaOH (99.995%, Aldrich), $[Pd(NH_2CH_2CH_2NH_2)_2]Cl_2$ (99.9%, Aldrich), $[Pd(NH_3)_4](NO_3)_2$ (10 wt.% in water, Aldrich), $[Pt(NH_3)_4](NO_3)_2$ (99.99%, Alfa Aesar), $[Rh(NH_3)_5Cl]Cl_2$ (Rh 34.5 % min, Alfa Aesar), $[Rh(NH_2CH_2CH_2NH_2)_3]Cl_3 \cdot 3H_2O$ (≥ 99.5%, Aldrich), $[Ru(NH_3)_6]Cl_3$ (98%, Aldrich), methanol (CH_3OH, 99.9%, Aldrich), isobutanol (i-C_4H_9OH, 99.9%, Aldrich), toluene (≥ 99.9%, Aldrich), He (99.999 %, Praxair), H_2 (99.999%, Praxair), D_2 (99.999%, Praxair), H_2-D_2 mixture (50.05% H_2, 49.95% D_2, Praxair, certified mixture), H_2S (0.5% H_2S/H_2, Praxair, certified mixture), ethene (5% C_2H_4/He, Praxair, CS) and thiophene (99%, Aldrich) were used as received.

3.4.2 Synthesis. Gels with molar composition of 20 Na_2O: 1.0 Al_2O_3: 1.5 SiO_2: 160 H_2O for SOD and 5.5 Na_2O: 1.0 Al_2O_3: 4.0 SiO_2: 190 H_2O for GIS were prepared. $NaAlO_2$ and NaOH were dissolved in demineralized H_2O and mixed with fumed SiO_2. Metal precursors $[Pt(NH_3)_4](NO_3)_2$, $[Rh(NH_2CH_2CH_2NH_2)_3]Cl_3 \cdot 3H_2O$ or $[Ru(NH_3)_6]Cl_3$ were dissolved in 10.0 cm^3 H_2O and added dropwise to the gel at 0.0833 cm^3 s^{-1}. The gel was transferred into a 125 cm^3 polypropylene container (Nalgene), sealed, and homogenized by vigorous magnetic stirring for 600 sec. These gels were stirred in an oil bath at 400 rpm and 373 K for 7 h for SOD and 363 K for 3 d for GIS. The solids were collected on a fritted funnel (Pyrex 36060, 10-15 μm) and washed with deionized water until the rinse liquid reached pH 7-8. The sample was treated in ambient air at 373 K overnight, then heated in air (1.667 $cm^3 g^{-1} s^{-1}$) at 623 K (0.0333 K s^{-1}) for 3 h, and treated in 9% H_2/He (1.667 $cm^3 g^{-1} s^{-1}$, Praxair) at 573 K (0.0333 K s^{-1}) for 2 h. Samples were passivated under 0.5% O_2/He (1.667 $cm^3 g^{-1} s^{-1}$, Praxair) for 1 h at ambient temperature before air exposure.

The successful encapsulation of Pd clusters into SOD and GIS required initially dispersed ligand stabilized metal precursors over the SiO_2 surface. $[Pd(NH_2CH_2CH_2NH_2)_2]Cl_2$ was first dissolved in deionised water and then fumed SiO_2 was added to the mixture. The resulting mixture was stirred at 400 rpm and 333 K for 3 h. Then, a solution of NaOH and $NaAlO_2$ was added and stirred at 400 rpm and 333 K for 1 h. The slurry temperature was raised to the crystallization temperature of the respective zeolite and the slurry was stirred at 400 rpm. Subsequent steps were the same as for the encapsulation of Pt, Ru, and Rh in SOD and GIS.

The procedures described above were unsuccessful in the synthesis of M/ANA zeolite because the high temperatures required for ANA synthesis decomposed the metal precursors to colloidal hydroxides. Instead, M/ANA samples were prepared by adding NaOH (9 cm^3 $g(M/GIS)^{-1}$) to a previously prepared M/GIS sample, and the mixture was placed within a sealed polypropylene container. The mixture was magnetically stirred at 400 rpm for 1 h and recrystallized in a Teflon-lined stainless steel autoclave under static conditions at 413 K for 3 d. The resulting solids were washed, dried, and treated using the procedures reported above for M/GIS samples.

The metal clusters supported on SiO_2 (Davisil®, Grade 646, 300 m^2g^{-1}) were prepared by the incipient wetness impregnation method using aqueous solutions of the metal precursors shown in Table 3.1. Silica supported samples were dried and treated using the same procedures as zeolite supported samples.

3.4.3 Physical Characterization. The identity and phase purity of zeolites and the absence of large metal structures were demonstrated by X-ray diffraction (Cu Kα radiation λ=0.15418 nm, Siemens, D500). Fractional metal dispersions were determined by hydrogen chemisorption using an Autosorb-1 titration apparatus (Quantachrome). Samples were heated to 623 K at 0.0333 K s^{-1} in flowing H_2 (Praxair, 99.999%, 0.2 cm^3 s^{-1} g^{-1}) and held for 1 h and then evacuated for 1 h at 623 K to remove any chemisorbed hydrogen. Dispersions were determined from total and irreversible H_2 uptakes using a 1:1 $H:M_{surface}$ adsorption stoichiometry [21]. Hydrogen adsorption isotherms were measured at 313 K and 5-50 kPa of H_2 for Pt, Ru and Rh samples and at 343 K and 0.4-1.5 kPa of H_2 for Pd samples to prevent formation of bulk β-hydrides in Pd samples [22]. Transmission electron microscopy (TEM) images were taken with Philips 420 TEM operated at 120 kV. Before TEM investigation, the samples were embedded into an adhesive polymer, mechanically thinned, and dimpled and further thinned by Ar ion-milling (Gatan PIP Precision Ion Polishing System, 3.0 kV). High-Angle Annular Dark Field scanning electron microscopy (HAADF STEM) images were taken with JEOL 2100 AC (abreaction-corrected). Before imaging, samples were embedded and microtomed using a diamond knife to approximate thickness of 70 nm. Particle size distributions were determined by counting at least 200 crystallites in the micrographs of each sample. The surface area weighted cluster diameters, $d_{TEM,}$ were calculated using $d_{TEM} = \sum n_i d_i^3 / \sum n_i d_i^2$ [23] and compared to average particle diameter calculated from hydrogen chemisorption measurements to confirm the accessibility of the surface of all clusters and complete removal of ligands.

3.4.4 Catalytic Rate Measurements. Oxidative dehydrogenation (ODH) of alkanols, ethene and toluene hydrogenation and H_2-D_2 exchange rates were measured on catalyst samples diluted with fumed SiO_2 (Cab-O-Sil, HS-5, 310 m^2 g^{-1}) using a quartz reactor with plug-flow dynamics. Dilution was achieved by intimate mixing at a diluent/catalyst mass ratio of 10 and pelleting and sieving the granules to retain aggregates of 0.18-0.25 mm diameter, 5-25 mg sample of which was then mixed with acid-washed quartz granules of similar size (Fluka, acid-purified, 1.0 g) to avoid intrapellet and bed gradients in concentration or temperature. Pre-reduced and passivated samples were treated in flowing H_2 (1.667 cm^3 g^{-1} s^{-1}) by heating to 573 K at 0.0333 K s^{-1} and holding for 1 h before measuring hydrogenation and H_2-D_2 exchange rates and in 20% O_2/He flow at 393 K for 1 h before oxidation rate measurements. Alkanol oxidation rates were measured with 4 kPa of alkanol, 9 kPa of O_2 and 87 kPa of He as diluent at 393 K, toluene hydrogenation at 0.35 kPa of toluene, 99.65 kPa of H_2 at 473 K and ethene hydrogenation at 0.95 kPa of ethene, 5 kPa of H_2, 94 kPa of He as diluent and 0/0.4 kPa of thiophene at 308/315 K. H_2-D_2 exchange rates were measured

using an equimolar H_2-D_2 mixture (50.05 kPa H_2, 49.95 kPa D_2) and 0/1.0 kPa of H_2S at 373 K. Rates are reported as turnover rates, defined as the number of molecules converted per time normalized by the number of surface metal atoms determined from chemisorption measurements. Reactant and product concentrations in oxidation and hydrogenation reactions were measured by gas chromatography (Agilent 6890GC) using a methyl-silicone capillary column (HP-1; 50 m x 0.25 mm, 0.25 μm film thickness) and a Porapak Q packed column (80-100 mesh, 1.82 m × 3.18 mm) connected to flame ionization and thermal conductivity detectors, respectively. H_2-D_2 exchange rates were measured by using on-line mass spectrometry (Leybold Inficon, Transpector Series). Quartz, fumed SiO_2, or metal-free zeolites did not give detectable ODH, hydrogenation or H_2-D_2 exchange rates and rates on M/zeolites did not depend on extent of dilution or change with reaction time.

3.5 Acknowledgments

We thank Dr. Alex Kuperman for technical input and advice, Dr. George D. Meitzner for the technical review of this work, Thomas Rea for HAADF imaging, and Chevron Energy Technology for the financial support for this research.

3.6 Figures and Tables

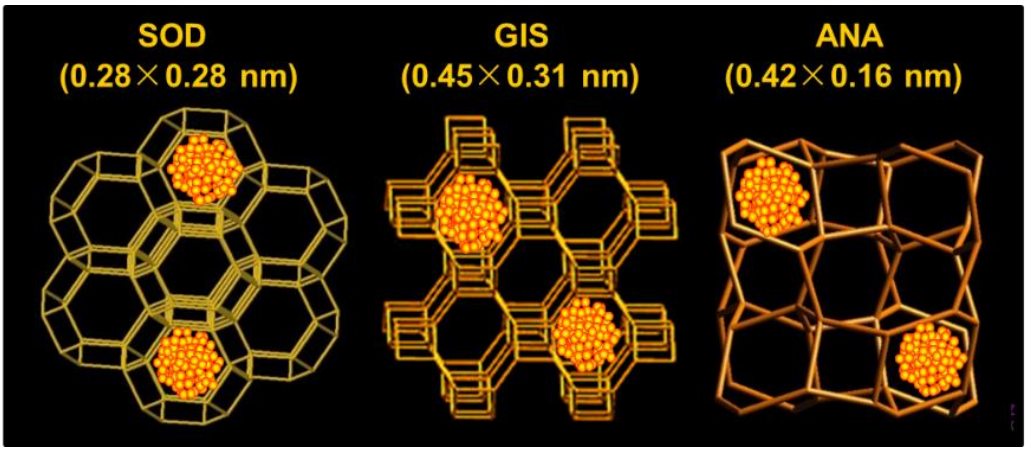

Figure 3.1 Pictorial representation of metal clusters encapsulated within zeolites and zeolite aperture sizes.

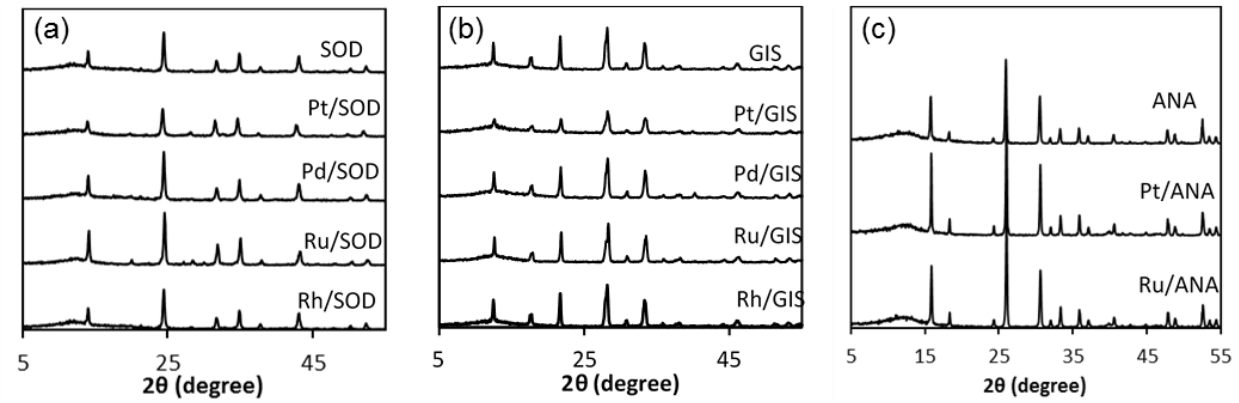

Figure 3.2 X-ray diffraction patterns of (a) M/SOD, (b) M/GIS, and (c) M/ANA samples (M = Pt, Pd, Ru, Rh).

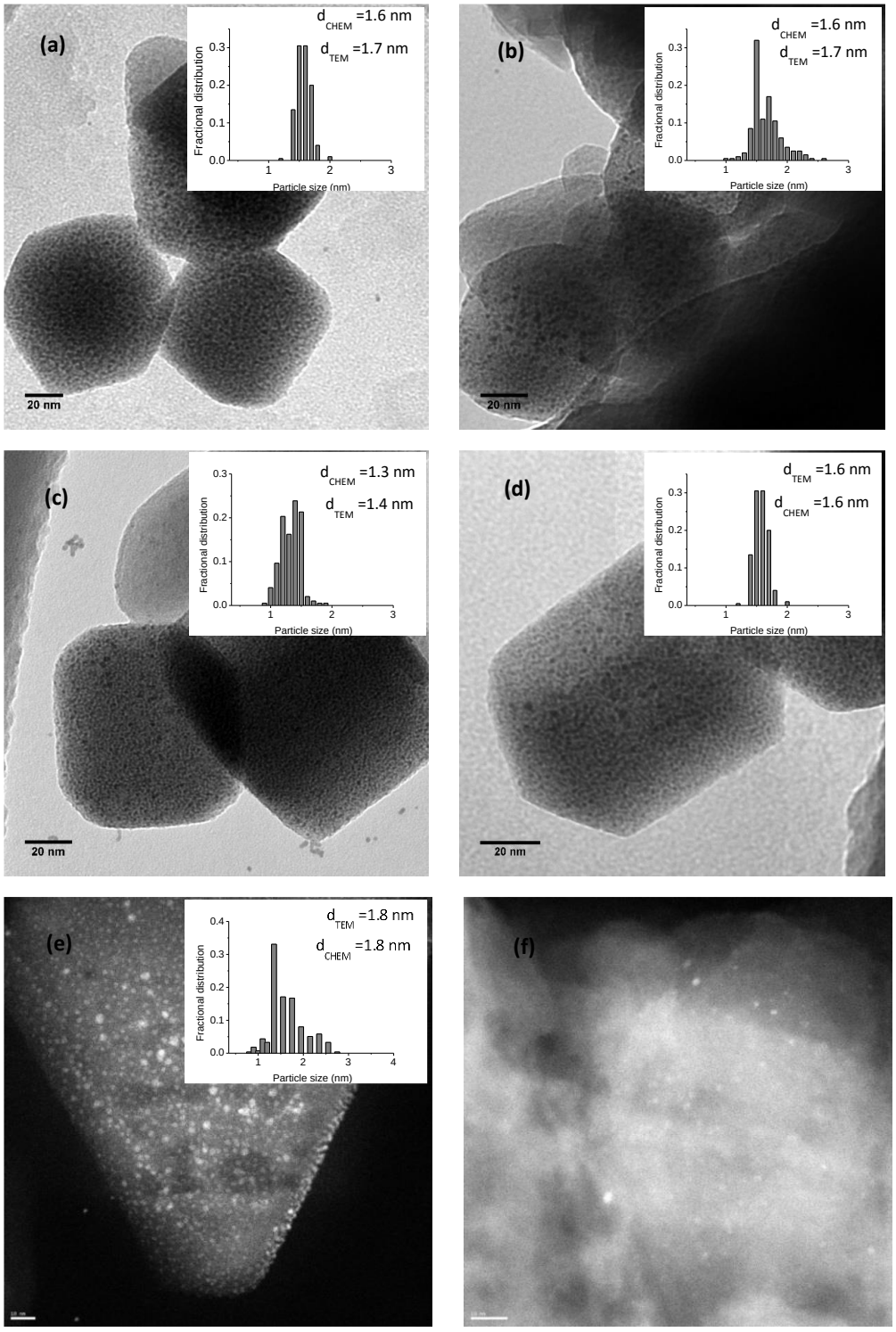

Figure 3.3 Metal clusters size distributions and TEM images of (a) Pt/GIS, (b) Pd/GIS, (c) Ru/GIS, (d) Rh/GIS, and HAADF STEM images of (e) Pt/ANA, and (f) Pt/SOD samples. Surface-weighted metal cluster size diameters, d_{TEM}, were calculated using $d_{TEM} = \sum n_i d_i^3 / \sum n_i d_i^2$. Metal clusters size distribution is not included for Pt/SOD because it was difficult to locate enough platinum clusters to be able to get statistical value for average cluster size.

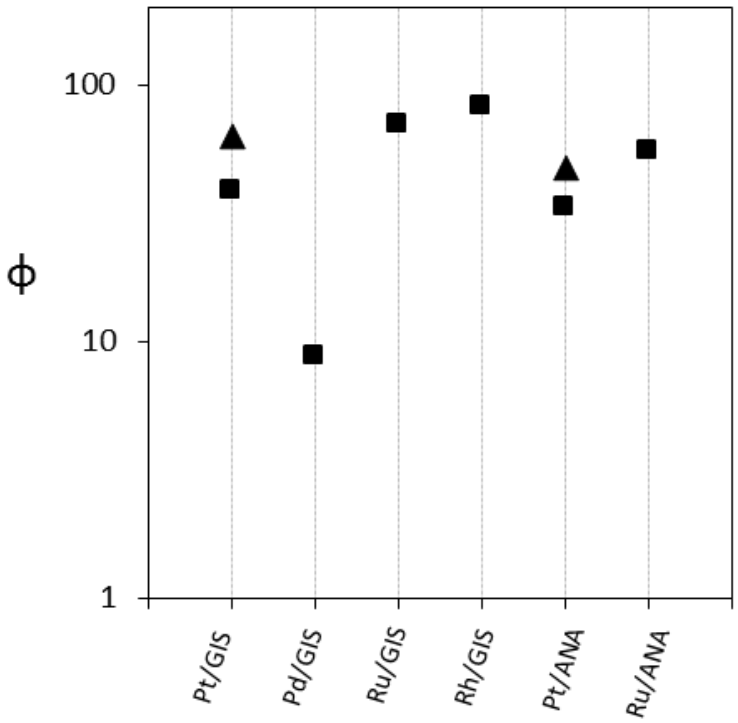

Figure 3.4 Encapsulation selectivity parameter (ϕ), reflecting the shape selectivity for various M/GIS and M/ANA samples (M = Pt, Pd, Ru, Rh) in alkanol oxidative dehydrogenation (ODH) (■) and ethene and toluene hydrogenation (▲). ϕ values larger than unity indicate the preferential containment of clusters within zeolite micropores that can sieve reactants based on size.

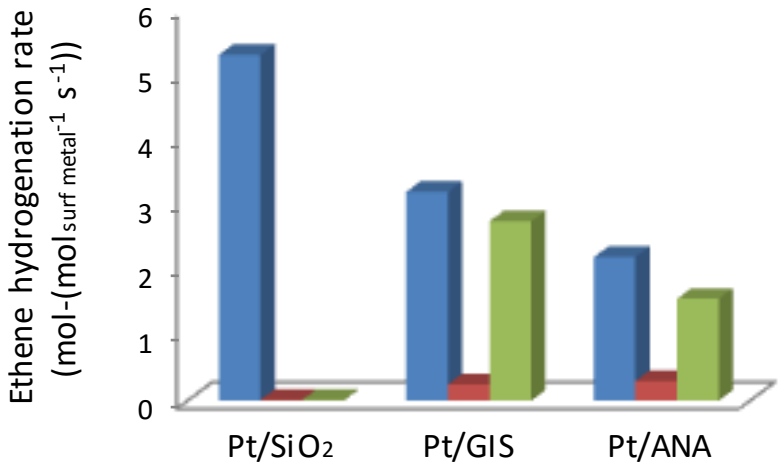

Figure 3.5 Ethene hydrogenation rate in Pt/SiO_2, Pt/GIS, and Pt/ANA samples without thiophene (blue) with 0.4 kPa thiophene added for 1 h (red), and after stopping thiophene injection (green). Ethene hydrogenation reaction was carried out with 0.95 kPa ethene, 5 kPa H_2 and 0 kPa/0.4 kPa thiophene at 315 K. Reaction turnover rate is defined as ethene hydrogenation rate per mol of surface metal atoms per second.

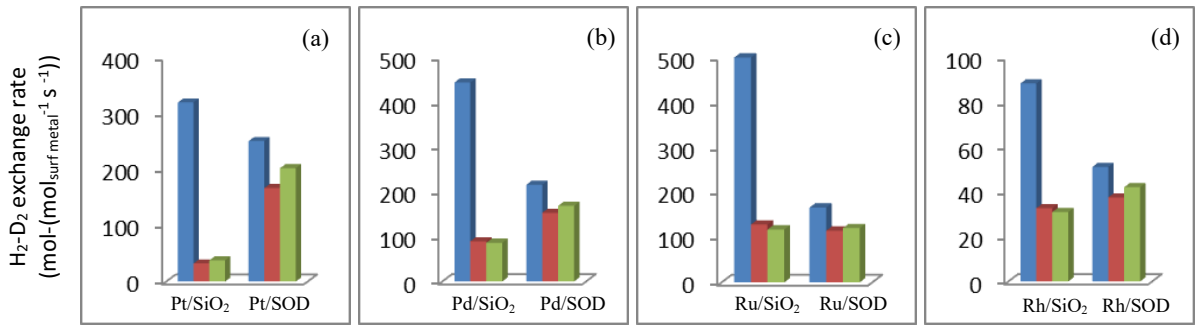

Figure 3.6 H_2-D_2 exchange rate in (a) Pt, (b) Pd, (c) Ru, and (d) Rh clusters dispersed on SiO_2 and SOD without H_2S (blue), with 1.0 kPa H_2S added for 1 h (red) and after stopping H_2S injection (green). H_2-D_2 exchange reactions were carried out with 50.05 kPa H_2, 49.95 kPa D_2 and 0 kPa/1 kPa H_2S at 373 K. Reaction turnover rate is defined as H_2-D_2 exchange rate per mol of surface metal atoms per second.

Table 3.1 Metal precursors, loadings, and dispersions of metal clusters (Pt, Pd, Ru, Rh) dispersed in SiO_2, SOD, GIS, and ANA samples

Sample	Precursor used	Metal loading[a] (wt%)	Metal dispersion[b] (fraction)
Pt/SiO_2	$[Pt(NH_3)_4](NO_3)_2$	0.79	0.61
Pd/SiO_2	$[Pd(NH_3)_4](NO_3)_2$	0.55	0.69
Ru/SiO_2	$[Ru(NH_3)_6]Cl_3$	0.50	0.50
Rh/SiO_2	$[Rh(NH_3)_5Cl]Cl_2$	1.10	0.60
Pt/SOD	$[Pt(NH_3)_4](NO_3)_2$	0.10	0.38
Pd/SOD	$[Pd(NH_2CH_2CH_2NH_2)_2]Cl_2$	0.10	0.23
Ru/SOD	$[Ru(NH_3)_6]Cl_3$	0.034	0.22
Rh/SOD	$[Rh(NH_2CH_2CH_2NH_2)_3]Cl_3 \cdot 3H_2O$	0.045	0.39
Pt/GIS	$[Pt(NH_3)_4](NO_3)_2$	0.86	0.70
Pd/GIS	$[Pd(NH_2CH_2CH_2NH_2)_2]Cl_2$	0.85	0.68
Ru/GIS	$[Ru(NH_3)_6]Cl_3$	0.40	0.63
Rh/GIS	$[Rh(NH_2CH_2CH_2NH_2)_3]Cl_3 \cdot 3H_2O$	0.24	0.67
Pt/ANA	$[Pt(NH_3)_4](NO_3)_2$	1.00	0.61
Ru/ANA	$[Ru(NH_3)_6]Cl_3$	0.50	0.50

[a]Analyzed by inductively coupled plasma optical emission spectroscopy.
[b] Metal dispersions estimated from H_2 chemisorptions.

Table 3.2 Catalytic properties of metal clusters (Pt, Pd, Ru, Rh) dispersed in GIS, ANA, and SiO_2 in oxidative dehydrogenation of alkanols[a]

Samples	$r_{methanol}$[b] (mol-($mol_{surf\text{-}metal}^{-1}$ s^{-1})	$r_{isobutanol}$[b] (mol-($mol_{surf\text{-}metal}^{-1}$ s^{-1})	$\chi_{ODH,j}$[c] j = zeolite, SiO2	ϕ[d]
Pt/GIS	3.56	0.0191	186.4	38.5
Pt/SiO_2	7.02	1.45	4.8	
Pd/GIS	0.20	0.0104	19.4	8.8
Pd/SiO_2	0.51	0.23	2.2	
Ru/GIS	0.13	0.0017	76.4	70.0
Ru/SiO_2	0.05	0.04	1.2	
Rh/GIS	0.17	0.0016	107.6	82.7
Rh/SiO_2	0.19	0.15	1.3	
Pt/ANA	0.33	0.0021	160.9	33.2
Pt/SiO_2	7.02	1.45	4.8	
Ru/ANA	0.02	0.0003	66.6	55.5
Ru/SiO_2	0.05	0.04	1.2	

[a] Alkanol oxidative dehydrogenation reactions were carried out with 4 kPa alkanols and 9 kPa O_2 at 393 K.
[b] Reaction turnover rate is defined as mole of reactant converted per mol of surface metal atoms per second.
[c] $\chi_{ODH,j} = r_{methanol} / r_{isobutanol}$, j = zeolite, SiO_2.
[d] $\phi = \chi_{ODH,zeolite}/\chi_{ODH,SiO2}$.

Table 3.3 Catalytic properties of Pt dispersed in GIS, ANA, and SiO_2 in hydrogenation of ethene[a] and toluene[b].

Samples	r_{ethene}[c] (mol-($mol_{surf\text{-}metal}^{-1}$ s^{-1})	$r_{toluene}$[c] (mol-($mol_{surf\text{-}metal}^{-1}$ s^{-1})	$\chi_{HYD,j}$[d] j = zeolite, SiO2	ϕ[e]
Pt/GIS	2.90	0.012	241.6	63.4
Pt/SiO_2	5.26	1.38	3.8	
Pt/ANA	2.00	0.011	181.8	47.7
Pt/SiO_2	5.26	1.38	3.8	

[a] Ethene hydrogenation reactions were carried out with 0.95 kPa ethene and 5 kPa H_2 at 308 K .
[b] Toluene hydrogenation reactions were carried out with 0.35 kPa toluene, 99.65 kPa H_2 at 473 K.
[c] Reaction turnover rate is defined as mole of reactant converted per mol of surface metal atoms per second.
[d] $\chi_{HYD,j} = r_{ethene} / r_{toluene}$, j = zeolite, SiO_2.
[e] $\phi = \chi_{HYD,zeolite} / \chi_{HYD,SiO2}$.

3.7 Supporting Information

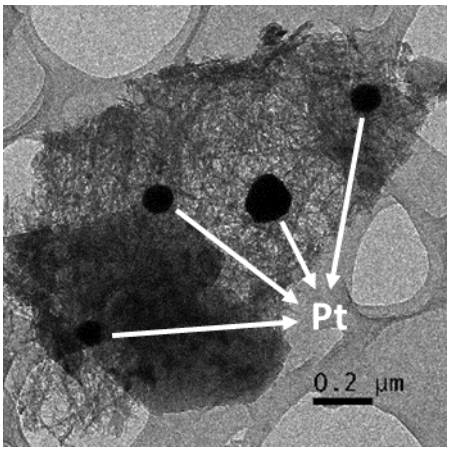

Figure 3.S1 TEM image of Pt/ANA sample synthesized by direct hydrothermal synthesis using amine-stabilized metal precursor ($[Pt(NH_3)_4](NO_3)_2$).

Table 3.S1 Stability of various metal precursors in the alkaline solution at 373 K.

Metal	**Precursors (10^{-2} mol/L)**	**Behavior in alkaline solution (pH=13)**
Pt	$Pt(NO_3)_2$	Precipitation < 10 min
	$[Pt(NH_3)_4](NO_3)_2$	Stable
Ru	$RuCl_3$	Precipitation < 10 min
	$[Ru(NH_3)_6]Cl_3$	Stable
Rh	$RhCl_3$	Precipitation < 10 min
	$[Rh(NH_3)_6]Cl_3$	Precipitation < 30 min
	$[Rh(NH_2CH_2CH_2NH_2)_3]Cl_3$	Stable
Pd	$Pd(NO_3)_2$	Precipitation < 10 min
	$[Pd(NH_3)_4](NO_3)_2$	Precipitation < 60 min
	$[Pd(NH_2CH_2CH_2NH_2)_2]Cl_2$	Stable

3.8 References

(1) Gallezot, P. *Post-Synthesis Modification I* 2002, 257.
(2) Sachtler, W. M. H. *Acc. Chem. Res.* 1993, 26, 383.
(3) Guczi, L.; Kiricsi, I. *Appl. Catal., A* 1999, 186, 375.
(4) Zhan, B.-Z.; Iglesia, E. *Angew. Chem. Int. Ed.* 2007, *46*, 3697.
(5) Zhan, B.-Z.; White, M. A.; Sham, T. K.; Pincock, J. A.; Doucet, R. J.; Rao, K. V. R. Rao, Robertson, K. N.; Cameron, T. S. *J. Am. Chem. Soc.* 2003, 125, 2195.
(6) Csicsery, S. M. *Zeolites* 1984, 4, 202.
(7) Weisz, P. B.; Frilette, V. J.; Maatman, R. W.; Mower, E. B. *J. Catal.* 1962, 1, 307.
(8) Creyghton, E.; Downing, R. *J. Mol. Catal. A: Chemical* 1998, 134, 47.
(9) Altwasser, S.; Gläser, R.; Weitkamp, J. *Microporous Mesoporous Mater.* 2007, 104, 281.
(10) Yang, H.; Chen, H.; Chen, J.; Omotoso, O.; Ring, Z. *J. Catal*. 2006, 243, 36.
(11) Balkus, K. J.; Gabrielov, A. G. *J. Inclusion Phenom. Mol. Reco. Chem.* 1995, 21, 159.
(12) Choi, M.; Wu, Z.; Iglesia, E. *J. Am. Chem. Soc*. 2010, 132, 9129.
(13) Wu, Z.; Goel S.; Choi, M.; Iglesia, E. *J. Catal.* 2014, 311, 458.
(14) Cundy, C. S.; Cox, P. A. *Microporous Mesoporous Mater*. 2005, 82, 1.
(15) Barrer, R. M. *Zeolite Synthesis*; American Chemical Society: Washington, DC, 1989; Vol. 398, p 11.
(16) Baerlocher, C.; McCusker, L. B. Database of Zeolite Structures: http://www.iza-structure.org/databases/.
(17) Zones, S. I. *J. Chem. Soc., Faraday Trans*. 1991, 87, 3709.
(18) Kohoutkova, M.; Klouzkova, A.; Maixner, J.; Mrazova, M. *Ceramics-Silikáty* 2007, 51, 9.
(19) Liu, H.; Iglesia, E. *J. Phys. Chem. B* 2005, 109, 2155.
(20) Weitkamp, J.; Fritz, M.; Ernst, S. *Int. J. Hydrogen Energy* 1995, 20, 967.
(21) Bergeret, G.; Gallezot, P. *Handbook of Heterogeneous Catalysis;* Wiley-VCH Verlag GmbH & Co. KgaA: New York, 2008.
(22) Aben, P. *J. Catal*. 1968, 10, 224.
(23) Schneider, M.; Duff, D.; Mallat, T.; Wildberger, M.; Baiker, A. *J. Catal*. 1994, 147, 500.

Chapter 4

Encapsulation of Metal Clusters within MFI via Interzeolite Transformations and Direct Hydrothermal Syntheses and Catalytic Consequences of Their Confinement

Abstract

The encapsulation of metal clusters (Pt, Ru, Rh) within MFI was achieved by exchanging cationic metal precursors into a parent zeolite (BEA, FAU), reducing them with H_2 to form metal clusters, and transforming these zeolites into daughter structures of higher framework density (MFI) under hydrothermal conditions. These transformations required MFI seeds or organic templates for FAU parent zeolites, but not for BEA, and occurred with the retention of encapsulated clusters. Clusters uniform in size (1.3-1.7 nm) and exposing clean and accessible surfaces formed in BEA and FAU zeolites; their size remained essentially unchanged upon transformation into MFI. Encapsulation selectivities, determined from the relative hydrogenation rates of small (toluene) and large (alkyl arenes) molecules and defined as the ratio of the surface areas of all the clusters in the sample to that of external clusters, were very high (8.1-40.9) for both parent and daughter zeolites. Encapsulation into MFI via direct hydrothermal syntheses was unsuccessful because metal precursors precipitated prematurely at the pH and temperatures required for MFI synthesis. Delayed introduction of metal precursors and F^- (instead of OH^-) as the mineralizing agent in hydrothermal syntheses increased encapsulation selectivities, but they remained lower than those achieved via interzeolite transformations. These interconversions provide a general and robust strategy for encapsulation of metals when precursors can be introduced via exchange into a zeolite that can be transformed into target daughter zeolites with higher framework densities, whether spontaneously or by using seeds or structure-directing agents (SDA).

4.1 Introduction

Zeolites are ordered microporous aluminosilicates with well-defined crystal structures. Voids of molecular dimensions allow zeolites to catalyze chemical reactions with unique reactivities and selectivities [1-6]. Synthesis protocols for encapsulating metals [7-18] within zeolites can expand the diversity of catalytic chemistries, made possible by the ability of microporous solids to select reactants, transition states, and products based on their molecular size and shape, and to protect active sites from larger species that act as poisons by titrating active sites. General protocols for encapsulating metal clusters within zeolites of different void size and geometry can be used to tailor or select zeolite structures for specific catalytic applications; the methods include ion exchange [10-12], incipient wetness [10, 12], and incorporation of metal precursors during synthesis [9, 10, 13-18].

The apertures within small and medium-pore zeolites preclude post-synthetic encapsulation protocols via ion-exchange from aqueous media, which require the migration of solvated metal-oxo oligomers that cannot diffuse through the small apertures in such zeolites [9, 13-18]. Recently, we have developed encapsulation methods that exploit the use of ligand-stabilized metal precursors to prevent the premature precipitation of metal precursors as colloidal oxyhydroxides

at the high pH and temperatures required for hydrothermal zeolite crystallization [15-18]. These protocols have led to the successful encapsulation of Pt, Pd, Rh, Ir, Re, and Ag clusters within LTA [17] and Pt, Pd, Ru, and Rh clusters within GIS and SOD [18]. Some zeolites require synthesis temperatures that decompose even ligand-stabilized metal precursors; in such cases, we have enforced encapsulation by first placing metal clusters within zeolites that form at milder conditions (parent structure) and then subjecting the sample to the conditions that convert this parent zeolite to the intended framework (daughter structure), while preserving encapsulation. These protocols have led to the successful encapsulation of Pt and Ru clusters within ANA [18].

MFI (ZSM-5) is a medium-pore silica-rich zeolite that typically requires high crystallization temperatures (423-473 K) and pH (>11) for its template-free synthesis; encapsulation in such materials remains inaccessible via procedures involving direct hydrothermal synthesis using ligand-stabilized metal precursors [15-18], as well as post-synthesis exchange [14], except in the case of monovalent or divalent cations. Here, we report a general strategy for the encapsulation of metal clusters within MFI by exploiting interzeolite transformations of BEA or FAU zeolites (parent structures) into MFI zeolite (daughter structure), without organic SDA, and describe the catalytic consequences of the selective encapsulation of metal clusters (Pt, Ru, Rh) within the void spaces of MFI frameworks.

Interzeolite transformations [19, 20] provide a general and convenient route for the encapsulation of clusters within microporous solids in those cases for which the successful placement of precursors can be accomplished within a parent zeolite structure via post-synthesis exchange or during hydrothermal crystallization. This parent structure, containing metal clusters within its microporous voids, can then be recrystallized without loss of encapsulation into a daughter structure of higher framework density, in this case MFI, for which more direct methods of encapsulation are unavailable or impractical (Scheme 4.1). We also report evidence for the factors that influence the encapsulation selectivity in direct hydrothermal synthesis protocols. Such direct methods lead to low encapsulation yields, making interzeolite transformations the method of choice for the encapsulation of metal clusters within MFI.

4.2 Experimental Section

4.2.1 Reagents and Materials. Fumed SiO_2 (Cab-O-Sil, HS-5, 310 $m^2 g^{-1}$), NaOH (99.995%, Sigma Aldrich), FAU (CBV780, Zeolyst, H-FAU, Si/Al = 40), BEA (CP811E-75, Zeolyst, H-BEA, Si/Al = 37.5), tetrapropylammonium bromide (TPABr; 98%, Sigma Aldrich), $NaAlO_2$ (anhydrous, Riedel-de Haen, technical), $Al(NO_3)_3.9H_2O$ (> 98%, Strem Chemical), NH_4F (> 98%, Fluka), tetraethylorthosilicate (TEOS; 98%, Sigma Aldrich), $[Pt(NH_3)_4](NO_3)_2$ (99.99%, Alfa Aesar), $[Rh(NH_2CH_2CH_2NH_2)_3]Cl_3 \cdot 3H_2O$ (≥ 99.5%, Aldrich), $RuCl_3$ (45-55% wt. Ru, Sigma Aldrich), Ludox AS-30 colloidal silica (30% wt. suspension in H_2O, Sigma Aldrich), $[Ru(NH_3)_6]Cl_3$ (98%, Aldrich), toluene (≥ 99.9%, Aldrich), 1,3,5-trimethyl benzene (98%, Aldrich), 1,3,5-triisopropyl benzene (98%, Aldrich), He (99.999%, Praxair), Air (99.999%, Praxair), 0.5% O_2/He (99.999%, Praxair), 9% H_2/He (99.999%, Praxair) and H_2 (99.999%, Praxair) were used as received.

4.2.2 Synthesis Procedures

4.2.2.1 MFI Seed Crystals. In a typical synthesis, 649 g of water, 740 g of 1 mol dm^{-3} NaOH (Baker Reagent), 98 g of tetrapropylammonium bromide (Kodak Chemicals) were added to 872 g of Ludox AS-30 colloidal SiO_2 (Dupont). The synthesis mixture was then transferred into a Hastelloy-lined stainless steel autoclave (3.8 dm^3), pressure tested and held at 423 K for 4 days in a convection oven under rotation (78 rpm). After 4 days, the autoclave was cooled, and the resulting solid was collected by filtration and washed with deionized water (17.9 MΩ·cm resistivity) until the rinse liquids reached a pH of 7-8. The resulting product was crystalline MFI (confirmed by powder X-ray diffraction (XRD)) with Si/Al ~ 300 (by Inductively-coupled plasma atomic emission spectroscopy (ICP-AES) analysis) and ~6 μm sized zeolite crystals (by transmission electron microscopy (TEM)).

4.2.2.2 Synthesis of MFI via Interzeolite Transformations of Parent BEA or FAU Zeolites. In a typical synthesis, zeolite BEA (Si/Al = 37.5) or FAU (Si/Al = 40) was added (1.0 g) to an aqueous NaOH solution, into which the MFI seed crystals or structure-directing agents (TPABr) were added to prepare final mixtures with molar compositions listed in Table 4.1. These mixtures were placed within sealed polypropylene containers (Nalgene, 125 cm^3) and homogenized by vigorous magnetic stirring (400 rpm; IKA RCT Basic) for 1 h at ambient temperature. The mixture was then transferred into a Teflon-lined stainless steel autoclave and held at 423 K for 24-40 h under static conditions. The resulting solids were collected by filtration through a fritted disc Buchner filter funnel (Chemglass, 150 ml, F) and washed with deionized water (17.9 MΩ·cm resistivity) until the rinse liquids reached a pH of 7-8. The sample was heated in convection oven at 373 K overnight and the solid yield of the resulting product was defined as

$$Yield\ (\%) = \frac{Product\ (g)}{Parent\ zeolite\ (g) + Seed\ (g)} \times 100 \qquad \textbf{(1)}$$

The resulting product was then treated in flowing air (1.67 $cm^3\ g^{-1}\ s^{-1}$) to 623 K at 0.03 K s^{-1} and held at this temperature for 3 h. The samples after treatment were denoted as MFI_B, MFI_B-T, MFI_B-S, when synthesized from BEA, and MFI_F, MFI_F-T, MFI_F-S, when synthesized from FAU, in the direct, template-assisted and seed-assisted interzeolite transformations, respectively.

4.2.2.3 Encapsulation of Metal Clusters within BEA and FAU by Ion Exchange Method. Parent zeolites (FAU or BEA) were added to an aqueous solution of NaCl (>99.0%, Sigma-Aldrich, 1 g zeolite per 100 cm^3 1 M solution) while stirring (400 rpm; IKA RCT Basic) at 353 K for 8 h. The exchange was repeated a total of three times to yield Na-Zeolite, and the solids were recovered by filtration, washed with deionized water and dried overnight in convection oven at 373 K and the resulting materials were used for subsequent ion exchange with metals. Metals (M = Pt, Ru, Rh) encapsulated within BEA or FAU were prepared by ion exchange from aqueous solutions of $[Pt(NH_3)_4](NO_3)_2$, $[Rh(NH_2CH_2CH_2NH_2)_3]Cl_3 \cdot 3H_2O$, or $[Ru(NH_3)_6]Cl_3$ (10:1 mass ratio of H_2O/zeolite, to achieve ~1% wt metal content) at 353 K by magnetic stirring (400 rpm; IKA RCT Basic) for 8 h. The solids obtained were collected by filtration through a fritted disc Buchner filter funnel (Chemglass, 150 mL, F) and washed with deionized water until the rinse liquids reached a pH of 7–8. These samples were then heated in convection oven at 373 K overnight and treated in flowing air (1.67 $cm^3\ g^{-1}\ s^{-1}$) to 623 K at 0.03 K s^{-1} and held for 3 h; the metal precursors were then exposed to a flow of 9% H_2/He (1.67 $cm^3\ g^{-1}\ s^{-1}$) and heated to 573 K

at 0.03 K s^{-1} and held for 2 h. After this treatment, the samples were passivated in 0.5% O_2/He flow (1.67 cm^3 g^{-1} s^{-1}) for 1 h at room temperature before exposure to ambient air. The resulting samples after treatment were denoted as M/BEA and M/FAU (M = Pt, Ru, Rh), synthesized from BEA and FAU, respectively.

4.2.2.4 Encapsulation of Metal Clusters within MFI via Interzeolite Transformations of Parent BEA. The encapsulation of metal clusters within MFI was achieved by interzeolite transformations of M/BEA (M= Pt, Ru), using M/BEA samples as parent zeolites. M/BEA (M = Pt, Ru) samples (1.0 g) were added to an aqueous NaOH solution (0.35 NaOH: 1.0 SiO_2: 0.0133 Al_2O_3: 65 H_2O) to prepare mixtures with molar compositions listed in Table 4.1. These mixtures were placed within sealed polypropylene containers (Nalgene, 125 cm^3) and homogenized by vigorous magnetic stirring (400 rpm; IKA RCT Basic) for 1 h at ambient temperature. The mixture was then transferred into a Teflon-lined stainless steel autoclave and held at 423 K under static conditions for 40 h. The resulting solids were collected by filtration through a fritted disc Buchner filter funnel (Chemglass, 150 ml, F) and washed with deionized water until the rinse liquids reached a pH of 7-8. These samples were heated in ambient air at 373 K overnight and then treated in flowing air (1.67 cm^3 g^{-1} s^{-1}) to 673 K at 0.03 K s^{-1} and held for 3 h; the metal precursors were then exposed to a flow of 9% H_2/He (1.67 cm^3 g^{-1} s^{-1}) and heated to 623 K at 0.03 K s^{-1} and held for 2 h. After this treatment, the samples were passivated in 0.5% O_2/He flow (1.67 cm^3 g^{-1} s^{-1}) for 1 h at room temperature before exposure to ambient air. The resulting samples after treatment were denoted as M/MFI_B (M = Pt, Ru), synthesized via interzeolite transformations of M/BEA parent zeolites.

4.2.2.5 Encapsulation of Metal Clusters within MFI via Interzeolite Transformations of Parent FAU. The encapsulation of metal clusters within MFI was also achieved by interzeolite transformations of M/FAU (M= Pt, Ru, Rh), using M/FAU samples as parent zeolites. M/FAU (M = Pt, Ru, Rh) samples (1.0 g) were added to an aqueous NaOH solution (0.5 NaOH: 1.0 SiO_2: 0.0125 Al_2O_3: 95 H_2O) along with 10 % wt. MFI seeds (% wt. based on parent FAU) to prepare mixtures with molar compositions listed in Table 4.1. All of the subsequent synthesis and treatment steps were identical to those described for M/MFI_B samples synthesized via interzeolite transformation of M/BEA samples. The resulting samples after treatment were denoted as M/MFI_F (M = Pt, Ru, Rh), synthesized via interzeolite transformations of M/FAU parent zeolites.

4.2.2.6 Encapsulation of Metal Clusters within MFI via Direct Hydrothermal Syntheses. The encapsulation of metal clusters within MFI was studied at various synthesis conditions, shown in Table 4.5, during hydrothermal syntheses, adapted from [21, 22]. Synthesis gels with the molar compositions shown in Table 4.5 were prepared. In a typical experiment, alumina source ($NaAlO_2$ or $Al(NO_3)_3.9H_2O$) and NaOH were dissolved in deionized H_2O (17.9 MΩ·cm resistivity) and mixed with SiO_2 source (Ludox AS-30 or TEOS) and other necessary reagents (e.g., TPABr, NH_4F or HF) to prepare the mixtures of molar composition shown in Table 4.5. The resultant gel was transferred into a 125 cm^3 polypropylene container (Nalgene), sealed, and homogenized by magnetic stirring at 400 rpm (IKA RCT Basic) for 1 h at ambient temperature. The mixture was then transferred into a Teflon-lined stainless steel autoclave and held at desired crystallization temperature under static conditions for a total synthesis time shown in Table 4.5. The resulting solids were collected by filtration through a fritted disc Buchner filter funnel (Chemglass, 150 ml, F) and washed with deionized water (17.9 MΩ·cm resistivity) until the rinse liquids reached a pH

of 7-8. All of the subsequent treatment steps were identical to those described for M/MFI$_B$ samples synthesized via interzeolite transformations of M/BEA samples.

4.2.2.7 Silica-Supported Metal Clusters. The metal clusters dispersed on SiO_2 (Davisil®, Grade 646, 300 m^2g^{-1}) were prepared by the incipient wetness impregnation methods [16] using aqueous solutions of the same metal precursors as for the ion-exchanged zeolites (BEA or FAU). Silica supported metal samples were also treated using the same procedures as the ion-exchanged BEA or FAU samples (subsection 4.2.2.3).

4.2.3 Structural Characterization. The identity and phase purity of product zeolites as well as the absence of large metal clusters were demonstrated by powder X-ray diffraction (Cu Kα radiation λ =0.15418 nm, 40 kV, 40 mA, Bruker D8 Advance). Diffractograms were measured for 2θ values of 5-50^o at 0.02^o intervals with a 2 s scan time. Si, Al, Na, and metal (Pt, Ru, or Rh) contents were measured by inductively-coupled plasma atomic emission spectroscopy (IRIS Intrepid spectrometer; Galbraith Laboratories). The dispersion of the metal clusters was determined by H_2 chemisorption uptakes using volumetric methods. Samples were heated to 623 K at 0.03 K s^{-1} in flowing H_2 (1.67 cm^3 s^{-1} g^{-1}) and held for 1 h and then evacuated for 1 h at 623 K to remove any weakly-adsorbed hydrogen before being cooled to 298 K. Hydrogen chemisorption uptakes were measured at 298 K and 5-50 kPa of H_2 on metal containing samples. Dispersions were determined from the difference between total and irreversible H_2 uptakes, extrapolated to zero pressure, using a 1:1 H:$M_{surface}$ (M = Pt, Ru, Rh) adsorption stoichiometry [23]. Transmission electron microscopy (TEM) images were taken with Philips/FEI Tecnai 12 microscope operated at 120 kV. Before TEM analysis, the samples were suspended in ethanol and dispersed onto ultrathin carbon/holey carbon films supported on 400 mesh Cu grids (Ted Pella Inc.). Size distributions of metal clusters were determined from measuring more than 300 clusters for each sample. Surface-averaged cluster diameters, d_{TEM} [23], were calculated using

$$d_{TEM} = \frac{\sum n_i {d_i}^3}{\sum n_i {d_i}^2} \qquad (2)$$

where n_i is the number of clusters having a diameter d_i. TEM-derived size distributions were also used to calculate the dispersity index (DI) of the metal clusters. The DI value is given by surface-averaged diameter (d_{TEM}; Eq. 2) divided by the number-averaged diameter ($d_n=\sum n_i d_i/\sum n_i$) [24].

$$Dispersity\ Index\ (DI) = \frac{d_{TEM}}{d_n} = \frac{(\frac{\sum n_i {d_i}^3}{\sum n_i {d_i}^2})}{(\frac{\sum n_i d_i}{\sum n_i})} \qquad (3)$$

This parameter is a measure of the cluster size heterogeneity of metal clusters, with a value of unity reflecting unimodal clusters and values smaller than 1.5 indicating relatively uniform size distributions [23-25].

4.2.4 Catalytic Rate Measurements. Toluene, 1,3,5-trimethyl benzene (1,3,5-TMB), and 1,3,5-triisopropyl benzene (1,3,5-TIPB) hydrogenation rates were measured on catalyst samples diluted with fumed SiO_2 (Cab-O-Sil, HS-5, 310 m^2 g^{-1}) using a quartz tubular reactor with plug-flow dynamics. Dilution was achieved by intimate mixing at a diluent/catalyst mass ratio of 10, pelletizing and sieving the granules to retain aggregates of 0.18-0.25 mm diameter. These granules (5-25 mg) were then mixed with acid-washed quartz granules of similar size (Fluka, acid-purified, 1.0 g, 0.18-0.25 mm). Such dilution was used to avoid intrapellet or bed concentration and temperature gradients.

Pre-reduced and passivated samples were treated in flowing H_2 (1.67 $cm^3\ g^{-1}\ s^{-1}$) by heating to 623 K at 0.03 K s^{-1} and holding for 1 h prior to measuring hydrogenation rates. Arene hydrogenation rates were measured with 0.35 kPa toluene or 0.26 kPa 1,3,5-TMB or 0.15 kPa 1,3,5-TIPB and 100 kPa H_2 at 473 K. Toluene (0.59 nm kinetic diameter [26]), but not 1,3,5-TMB (0.74 nm kinetic diameter [27]) for MFI (~0.55 nm aperture [28]) and 1,3,5-TIPB (0.84 nm kinetic diameter [27]) for BEA (~0.70 nm aperture [28]) and FAU (0.74 nm aperture [28]), can diffuse through the apertures of zeolites and access active sites contained within the zeolitic voids. Rates are reported as turnover rates, defined as hydrogenation rates normalized by the number of surface metal atoms determined from hydrogen chemisorption uptakes. Reactant and product concentrations were measured by gas chromatography (Agilent 6890GC) using a methyl-silicone capillary column (HP-1; 50 m x 0.25 mm, 0.25 μm film thickness) connected to a flame ionization detector. Quartz, fumed SiO_2 or metal-free zeolites did not give detectable hydrogenation rates for any of these reactants and measured rates did not depend on the extent of dilution or on time on stream for any of the catalysts, consistent with absence of temperature or concentration gradients and of detectable deactivation.

4.3 Results and Discussion

The encapsulation of monovalent and divalent cations within medium-pore zeolites, such as MFI, can be achieved by post-synthesis methods involving aqueous or vapor phase exchange or even incipient wetness impregnation [10-12]. These methods fail, however, for trivalent and higher-valent metals (e.g., Ru, Rh, Ir, etc.), which cannot enter medium-pore and small-pore zeolites as solvated cations or anions, because of their larger size and their extended charge-balancing double-layer, or even as volatile complexes [13-18]. Thus, the encapsulation of higher-valent metal precursors within these materials requires that precursors be placed and retained within microporous frameworks during their hydrothermal synthesis and subsequent thermal treatment. In such cases, interzeolite transformations can provide an alternate synthetic route for the encapsulation of metal clusters within zeolitic voids, when a zeolite of lower framework density and larger apertures can be used to initially contain metal precursors or clusters; such materials can then be subsequently converted to a zeolite with higher framework density and smaller apertures while retaining the encapsulated species within the zeolitic voids.

Interzeolite transformations [19, 20] can convert structures with lower framework densities into those with higher framework densities, which tend to be thermodynamically more stable. These interconversions may avoid costly organic templates and/or decrease crystallization times; they may also provide more general routes for encapsulating clusters within those zeolites that would otherwise require synthesis temperatures that lead to the decomposition of metal precursors during hydrothermal syntheses, even for precursors containing protecting ligands. Thermodynamics typically allow transformations that increase the zeolite framework density (FD; reported here as T atoms/nm^3 [28, 29], where T stands for Si or Al atoms in the zeolite framework), but not all such processes are kinetically-accessible under the hydrothermal conditions that are required for the synthesis of daughter structures.

BEA (FD 15.3 [28]) and FAU (FD 13.3 [28]) can be recrystallized to zeolites with higher framework densities in aqueous NaOH solution at temperatures above those that cause their own respective crystallizations from amorphous silica–alumina precursors under hydrothermal

conditions (360–400 K). Crystalline MFI (FD 18.4 [28]) samples were successfully synthesized here from BEA, in the presence or absence of MFI seeds or organic structure directing agents (X-ray diffractograms; Figure 4.1i), using aqueous NaOH solutions (0.35 NaOH: 1.0 SiO_2: 0.0133 Al_2O_3: 65 H_2O, Table 4.1) under autogenous pressures at 423 K. Thus, we conclude that this transformation can occur spontaneously, without significant kinetic hindrance, and even in the absence of MFI seeds or organic structure-directing agents (SDA).

In contrast, FAU to MFI transformations required the presence of either MFI seeds or tetrapropylammonium bromide (TPABr) as SDA (X-ray diffractograms; Figure 4.1ii) in aqueous NaOH at 423 K under hydrothermal conditions (0.5 NaOH: 1.0 SiO_2: 0.0125 Al_2O_3: 95 H_2O, Table 4.1). In the absence of seeds or SDA, FAU converted to amorphous solids, but MFI crystals were obtained when FAU was transformed in the presence of TPABr (SDA) or MFI seeds (10% wt seeds, ~6 μm seed crystals) (X-ray diffraction pattern; Figure 4.1ii). These results show that SDA and MFI seeds help to overcome the kinetic hurdles prevalent in the formation of thermodynamically favored MFI structures from parent FAU zeolites.

We note that the framework structures and composite building units (CBU) of the parent BEA and daughter MFI zeolites include a common *mor* structural motif [28], while FAU and MFI lack such a common CBU. It seems plausible, therefore, that a CBU, present in BEA and required to form MFI, remains essentially intact within the BEA-derived intermediates during its conversion to MFI; this CBU may aid the local nucleation of MFI and, in doing so, reduce kinetic hurdles, thus allowing the BEA transformation into MFI to occur without seeds or SDA. As a consequence, BEA to MFI transformations (X-ray diffractograms, Figure 4.1i), containing *mor* as a common CBU, become kinetically feasible. This common CBU could serve as kinetic mediator [30, 31] for nucleating the daughter structure, suggesting that zeolites containing common CBU elements may be able to overcome kinetic barriers that obstruct their interconversions in the direction dictated by the thermodynamic tendency of zeolites to form structures with greater framework densities. In contrast, SDA moieties or MFI seeds are required to convert parent FAU to product MFI (X-ray diffractograms, Figure 4.1ii), apparently to provide the kinetic mediation [32] required in the absence of any common CBU.

The solid yields of products (Table 4.1, eq 1) were 46.4% for BEA to MFI transformation in the absence of SDA or seeds, 47.1% for seed-assisted and 47.3% for template-assisted BEA to MFI transformations and 47.1% for seed-assisted and 57.9% for template-assisted FAU to MFI transformations. These yields (Table 4.1) and Si/Al ratios of the product zeolites (22-23; Table 4.1) in direct and seed-assisted transformations indicate that nearly all the Al atoms in the parent BEA (Si/Al = 37.5) or FAU (Si/Al = 40) are incorporated into the MFI crystals. BEA and FAU transformations to MFI required 24-40 h (Table 4.1), while direct hydrothermal syntheses of MFI starting from Si and Al sources typically require 2–15 days with or without SDA [33]. Thus, the presence of a common CBU between parent and product zeolites or in the absence of it, product seeds in the synthesis assist the nucleation of MFI crystals and do so more effectively from intermediates formed from parent zeolites than from amorphous silica and alumina gels, resulting in significantly shorter synthesis times. As a result, such protocols may provide alternate routes to the synthesis of some zeolites; such routes may shorten crystallization times and decrease the cost and environmental impact associated with organic moieties.

Next, we show how such interzeolite transformations can be used to encapsulate metal clusters within MFI via interzeolite transformations of BEA and FAU zeolites containing encapsulated clusters as the parent materials. We first provide evidence for the encapsulation of metal clusters within these parent zeolites, which are then transformed to MFI with retention of encapsulated clusters.

4.3.1 Encapsulation of Metal Clusters within BEA and FAU Parent Zeolites via Aqueous Exchange Methods

4.3.1.1 Assessment of Cluster Size and Uniformity in BEA and FAU Parent Zeolites

This section describes the synthesis, structural characterization, and catalytic properties of Pt, Ru and Rh clusters within BEA and FAU parent zeolites, with the intent to use these materials for subsequent conversion to MFI. BEA and FAU containing metals (M/BEA and M/FAU, respectively; M = Pt, Ru, Rh) were synthesized via ion-exchange with Pt, Rh, and Ru precursors in aqueous solutions of $[Pt(NH_3)_4](NO_3)_2$, $[Ru(NH_3)_6]Cl_3$ or $[Rh(NH_2CH_2CH_2NH_2)_3]Cl_3 \cdot 3H_2O$ at 353 K (using the procedures described in subsection 4.2.2.3).

TEM images of Pt clusters dispersed on BEA and FAU zeolites after exchange and thermal treatment in flowing air at 623 K for 3 h and in H_2 at 573 K for 2 h are shown in Figure 4.2. These images show the presence of small Pt clusters in BEA (d_{TEM} = 1.6 nm; Table 4.2, calculated using eq 2) and FAU (d_{TEM} = 1.7 nm; Table 4.2); these clusters are narrowly distributed in size (DI = 1.07 and 1.03 for BEA and FAU, respectively; Table 4.2, from eq 3) and reside throughout zeolite crystals. Chemisorptive titrations of metal surfaces with H_2 gave Pt fractional dispersions of 0.88 for Pt/BEA and 0.78 for Pt/FAU (Table 4.2); these values correspond to mean cluster diameters (d_{chem}) of 1.3 and 1.4 nm, respectively, when clusters are spherical and have the bulk density of Pt metal [23]. In contrast, Pt clusters at similar loading and prepared by incipient wetness impregnation of mesoporous SiO_2 with same metal precursor are larger (d_{TEM} = 2.4 nm, d_{chem} = 1.8 nm; Table 4.2) and more broadly distributed (DI = 1.96; Table 4.2) than in Pt/BEA and Pt/FAU samples, suggesting that confinement within small zeolite voids inhibits sintering and the concomitant broadening of the cluster size distribution. The chemisorption-derived Pt cluster diameters (1.3–1.4 nm) in these zeolitic samples agree well with those measured by TEM (1.6–1.7 nm), indicating that the clusters detectable by microscopy contain clean surfaces accessible for chemisorption by H_2 titrants and that the ligands present during synthesis were completely removed by the thermal treatments used. Similarly, Ru clusters dispersed in BEA, and Ru and Rh clusters in FAU show d_{TEM} values of 1.4, 1.7, and 1.5 nm, DI values of 1.08, 1.16, and 1.09, and d_{chem} values of 1.4, 1.5, and 1.3 nm, respectively; consistent with the presence of small, uniform and clean metal clusters dispersed throughout the BEA and FAU parent zeolites.

4.3.1.2 Catalytic Evidence for Encapsulation of Metal Clusters in BEA and FAU Parent Zeolites

The small apertures in zeolites allow them to sieve reactants and products based on their molecular size. The relative reaction rates for small and large reactants at sites residing within accessible and inaccessible locations can be used to assess the fraction of the metal surface area that resides within zeolite voids. The rates of hydrogenation of toluene and 1,3,5-TIPB reactants

(0.59 [26] and 0.84 nm [27] respective kinetic diameters) were used to confirm the predominant presence of metal (Pt, Ru, Rh) clusters within the parent BEA (~0.70 nm aperture) and FAU (0.74 nm aperture) materials. Toluene, but not 1,3,5-TIPB, can access active metal sites encapsulated within BEA and FAU voids via diffusion through their interconnected voids and apertures [27].

Encapsulation selectivities were determined by first measuring the rates of hydrogenation of small (toluene) and large (1,3,5-TIPB) reactants on unconstrained clusters dispersed on SiO_2 ($\chi_{SiO_2} = r_{toluene}/r_{1,3,5\text{-}TIPB}$); this rate ratio reflects the relative reactivity of these two reactant molecules in the absence of diffusional constraints. A similar measurement of this ratio on metal-zeolite samples ($\chi_{zeolite}$) can then be used to determine the encapsulation selectivity parameter ($\phi = \chi_{zeolite}/\chi_{SiO_2}$), which reflects the ratio of the surface area of all the clusters in the sample to that of clusters at (fully accessible) locations outside zeolite crystals. The encapsulation selectivity is therefore a rigorous indicator of the extent to which the active surfaces are contained within microporous networks, which toluene (but not 1,3,5-TIPB) can access. This encapsulation selectivity parameter approaches unity for clusters with unimpeded access to reactants, such as those at external zeolite surfaces. Values of ϕ much larger than unity (~10, indicating > 90% of the active metal surfaces reside within zeolitic voids), in contrast, provide evidence that metal clusters predominantly reside within regions that restrict access to the large reactants and, therefore, are taken here as evidence of successful encapsulation.

Toluene and 1,3,5-TIPB hydrogenation reactions led to the respective exclusive formation of methyl cyclohexane and (*cis*- and *trans*-) 1,3,5-triisopropyl cyclohexane on all samples. Table 4.3 shows arene hydrogenation turnover rates on Pt, Ru, and Rh clusters dispersed on BEA (M/BEA), FAU (M/FAU), and SiO_2 (M/SiO_2). Toluene hydrogenation turnover rates were very similar on Pt/BEA and Pt/FAU than on Pt/SiO_2 (Table 4.3), consistent with the absence of cluster size effects or diffusional constraints for toluene reactions. In contrast, 1,3,5-TIPB turnover rates were much lower on Pt/BEA and Pt/FAU than on Pt/SiO_2 (by factors of 44 and 38, respectively, Table 4.3), indicating that 1,3,5-TIPB cannot access most of the clusters in BEA and FAU samples. The ratios of toluene to 1,3,5-TIPB hydrogenation turnover rates were therefore much higher on Pt/BEA and Pt/FAU (by factors of 180 and 160, respectively) than on Pt/SiO_2 (4.4), resulting in encapsulation selectivity parameters (ϕ) of 40.9 and 36.4 for Pt/BEA and Pt/FAU, respectively (Table 4.3). Encapsulation selectivity parameters (Table 4.3) were 14.3 and 15.4 for Ru clusters in BEA and FAU parent zeolites, respectively, and 21.8 for Rh clusters in FAU samples. These large encapsulation selectivity values confirm that clusters of all these metals reside preferentially within the void structures of BEA or FAU zeolites when such samples are prepared using ion exchange and reduction procedures reported here. These materials are therefore well-suited to assess whether encapsulated metal clusters can (i) interfere with FAU or BEA transformations to MFI and/or (ii) be retained during interzeolite transformations.

4.3.2 MFI-Encapsulated Metal Clusters via Interzeolite Transformations of BEA and FAU

4.3.2.1 Assessment of the Size and Uniformity of Metal Clusters in MFI

M/BEA and M/FAU (M = Pt, Ru, Rh) zeolites containing metal clusters (subsection 4.2.2.3) are used here as precursor materials to form MFI using the hydrothermal protocols described in subsections 4.2.2.4 and 4.2.2.5, and shown to be successful in the absence of metal clusters (section

4.3). The resulting samples are denoted here as M/MFI$_B$ (derived from M/BEA) and M/MFI$_F$ (derived from M/FAU). Neither seeds nor SDA were used in M/BEA to M/MFI transformations; MFI seeds were used (instead of SDA) in M/FAU to M/MFI transformations so as to avoid electrostatic and van der Waals interactions that may cause SDA species to dislodge clusters from intracrystalline MFI voids during hydrothermal interconversion protocols [14].

BEA and FAU zeolites were successfully transformed into MFI with or without encapsulated clusters in the parent zeolites (X-ray diffractograms; without metals, Figure 4.1; with metals, Figure 4.S1). Subsequent treatments in flowing air at 673 K for 3 h and then in flowing H_2 at 623 K for 2 h did not cause detectable changes in MFI crystallinity. X-ray diffractograms also did not show any lines for metal or oxide phases in M/MFI (M = Pt, Ru, Rh; Figure 4.S1) after H_2 treatment at 623 K for 2 h (1.01–1.55% wt metal; Table 4.2), consistent with the absence of large metal crystallites in MFI daughter structures.

TEM images of reduced and passivated M/MFI samples (M = Pt, Ru, Rh) detected small clusters uniform in size (Pt/MFI$_B$ and Pt/MFI$_F$ in Figure 4.3, Ru/MFI$_B$, Ru/MFI$_F$, and Rh/MFI$_F$ in Figure 4.S2). The surface-averaged mean cluster diameters and DI values obtained from TEM measurements (Table 4.2) were 1.7 nm and 1.41 for Pt/MFI$_B$ (vs 1.6 nm and 1.07 in parent Pt/BEA) and 1.0 nm and 1.09 for Pt/MFI$_F$ (vs 1.7 nm and 1.03 in parent Pt/FAU). The DI values of parent zeolites were only slightly larger than the corresponding product zeolites, suggesting that significant sintering or coalescence did not occur during interzeolite transformations. H_2 chemisorption measurements on Pt/MFI gave an average cluster diameter of 1.4 when it was prepared from Pt/BEA (d_{chem} = 1.3) and 1.5 when synthesized from Pt/FAU (d_{chem} = 1.4). These chemisorption-derived mean cluster diameters agree well with surface-averaged cluster diameters from TEM (1.0–1.7; Table 4.2), suggesting the absence of residues deposited from synthesis mixtures and not removed during post-synthesis treatments. The sizes of these metal clusters, however, are larger than the intersection voids of MFI (0.64 nm included sphere diameter [28]), which reflect the local disruption of the crystal structures near the location of the clusters. These locations represent only 0.4-0.5% of the void volume; as a result, they are not detectable in diffractograms and do not disrupt the ability of the void structure to sieve molecules based on size over the relevant distance for diffusion (crystal diameter). In contrast, Pt/SiO_2 showed a d_{TEM} value of 2.4 nm, a d_{chem} value of 1.8 nm, and a DI value of 1.96; these sizes and dispersities are significantly larger than those for the clusters dispersed on parent (Pt/BEA and Pt/FAU) and product (Pt/MFI) zeolite samples, suggesting that confining environments are essential for the synthesis of small and uniform metal clusters.

Similarly, DI values (1.09-1.16 (vs 1.08-1.16 for parent zeolites); Table 4.2), TEM-derived surface-averaged cluster diameters (1.3-1.5 (vs 1.4-1.7 for parent zeolites); Table 4.2) and chemisorption-derived mean cluster diameters (1.1-1.2 (vs 1.3-1.5 for parent zeolites); Table 4.2) for Ru/MFI$_B$, Ru/MFI$_F$, and Rh/MFI$_F$ were also consistent with the presence of small, uniform and clean metal clusters within MFI voids and with the retention of encapsulation during transformations from parent BEA or FAU materials.

4.3.2.2 Assessment of Encapsulation Selectivity of MFI-Encapsulated Metal Clusters from Selective Hydrogenation of Arenes

Hydrogenation rates of toluene and 1,3,5-TMB (0.59 nm and 0.74 nm kinetic diameters) were used to assess the extent of confinement of Pt, Ru, and Rh clusters within product MFI zeolites (~0.55 nm apertures). Toluene (but not 1,3,5-TMB) can access active sites encapsulated within MFI voids via diffusion through their interconnected voids and apertures [34].

1,3,5-TMB hydrogenation reaction led to the exclusive formation of (*cis*- and *trans*-) 1,3,5-trimethyl cyclohexane on all catalysts. Table 4.4 shows turnover rates for the hydrogenation of these arenes on metal clusters (M = Pt, Ru, Rh) clusters dispersed on SiO_2 (M/SiO_2) and MFI (M/MFI_B and M/MFI_F). Toluene hydrogenation turnover rates were somewhat lower on Pt/MFI_B and Pt/MFI_F than on Pt/SiO_2 samples (by factors of 1.2 and 2.7, respectively, Table 4.4), possibly because access to metal clusters was restricted by diffusion through the MFI apertures (~ 0.55 nm), which are similar to the size of toluene (0.59 nm kinetic diameter [26]) or due to the partial blockage of the pore entrances by the impervious debris or amorphous solids, present in small amount in these materials. In contrast, 1,3,5-TMB turnover rates were much smaller on Pt/MFI_B and Pt/MFI_F than on Pt/SiO_2 samples (by factors of 10 and 50, respectively, Table 4.4), suggesting that most of the active surfaces reside within MFI voids inaccessible to 1,3,5 TMB. Pt/MFI_B and Pt/MFI_F, synthesized via interzeolite transformations of Pt/BEA and Pt/FAU, respectively, gave much higher χ values (22.4 and 50.0 for Pt/MFI_B and Pt/MFI_F, respectively) for selective hydrogenation of toluene and 1,3,5-TMB than for the Pt clusters dispersed on SiO_2 (χ_{SiO2} = 2.7; Table 4.4); these values lead, in turn, to high encapsulation selectivities (ϕ= 8.3 and 18.5, respectively; Table 4.4), consistent with the preferential encapsulation of Pt clusters within MFI voids. The encapsulation selectivity value was 8.3 for Pt/MFI_B (vs. 40.9 for Pt/BEA) and 18.5 for Pt/MFI_F (vs. 36.4 for Pt/FAU); these encapsulation selectivities for product zeolites are lower than the values of their respective parent zeolite, consistent with the retention of most of the clusters within zeolitic pores during transformations, and consistent with slight increase in DI values from parent to product zeolites. Ru/MFI_B, Ru/MFI_F and Rh/MFI_F synthesized also gave much larger χ values (150, 60 and 17, respectively; Table 4.4) than for the respective metals dispersed on SiO_2 (6.6 and 2.1 for Ru and Rh, respectively; Table 4.4) and consequently, high encapsulation selectivities for hydrogenation reactions (22.7, 9.1 and 8.1, respectively (vs. 14.3, 15.4, 21.8 for their corresponding parent zeolite); Table 4.4), indicating that Ru and Rh clusters on these zeolitic samples indeed reside predominantly within locations accessible only to the smaller toluene reactant and that the encapsulation of these clusters within zeolitic voids was preserved during interzeolite transformations.

The high encapsulation selectivity values (8-23; Table 4.4) for M/MFI samples also indicate that for all these samples more than 88 % of the metal surface areas are contained within locations accessible to toluene but not to 1,3,5-TMB. These data, taken together with the TEM- and chemisorption-derived mean cluster diameters and size uniformity, suggest that most of the metal clusters initially present within BEA or FAU voids remained inside the zeolitic pores during the transformations, retaining encapsulation in the resulting MFI samples, that can select reactant based on molecular size and allow access to active sites only by the reactants smaller than the MFI aperture sizes.

Next, we address the challenges of direct hydrothermal crystallization approaches for encapsulation within MFI, which can be circumvented, as we have shown in this section, using interzeolite transformation protocols.

4.3.3 Synthesis of MFI-Encapsulated Metal Clusters and Identification and Control of Key Parameters that Affect Encapsulation

The successful synthesis of encapsulated clusters requires that MFI nucleation and growth from basic media occur before insoluble colloidal hydroxides form via reactions of metal precursors with OH^- species at the high pH required for synthesis. We seek here synthesis conditions that promote nucleation and growth, while inhibiting the premature precipitation of metal precursors. A schematic depiction of how synthesis strategies and conditions may accomplish such objectives is shown in Figure 4.4. In what follows, we examine these synthesis parameters according to the regions depicted in Figure 4.4 (e.g., whether OH^- or F^- are used as the mineralizing agents) with the objective of controlling the relative rates of zeolite nucleation and precursor precipitation. Additional details of the synthesis conditions used are given in Table 4.5, together with the encapsulation selectivity values of the catalytic materials formed. The encapsulation selectivity for these metal-zeolite materials are reported from the rates of hydrogenation of toluene and 1,3,5-TMB, as done for the materials prepared by interzeolite transformations of BEA or FAU into MFI.

In region III (Figure 4.4), the synthesis was carried out at high pH and temperature (pH 12, 433 K), which favors fast nucleation and crystallization of MFI, but also the rapid formation of insoluble hydroxides from the metal precursors. The encapsulation selectivity parameter values for the products formed at these conditions was near unity (0.95 for Ru using $RuCl_3$ precursor; M1 and 0.98 for Pt using $Pt(NH_3)_4(NO_3)_2$ precursor; M2, Table 4.5), suggesting the prevalence of external zeolitic clusters. The use of SDA moieties (tetrapropylammonium bromide) also promotes rapid and selective MFI crystallization, but such species can fill the intracrystalline voids, thus preventing the encapsulation of the metal precursors, even as solvated monomers. The selectivity parameter for the product in this case was, again, near unity (0.85 for Pt using $Pt(NH_3)_4(NO_3)_2$ precursor; M3, Table 4.5), indicating that the clusters formed do not reside during intracrystalline MFI voids. As a result, the use of SDA species must be avoided (or their concentration kept very low) during synthesis, while also maintaining conditions that disfavor the formation of colloidal hydroxides of metal precursors. Using the minimal amount of SDA required to fill the intracrystalline voids, while keeping low temperatures (383 K) but high OH^- levels (pH 12.9), did not lead to crystallization of MFI structures (M4, Table 4.5) and the amorphous solids formed did not provide any access constraints (0.90 encapsulation selectivity; Table 4.5).

These findings led us to consider the introduction of the metal precursors after hydrothermal treatments of the alumina and silica precursors at conditions (region II; Figure 4.4) but before the nucleation of MFI, which formed only after several days (M5, Table 4.5), with the aim to limit the time that metal precursors were subjected to conditions conducive to precipitation. During the initial period of hydrothermal treatments, MFI nuclei form slowly and crystals then grow much more rapidly [35, 36], and often require milder conditions of temperature or pH. These experiments (M5, Table 4.5) involved the treatment of the starting aluminosilicate gel (Si/Al = 166) at 383 K and pH 12.9 for 5 days, after which the autoclave contents were briefly cooled to ambient

temperature and a solution of the metal complex ($Pt(NH_3)_4(NO_3)_2$, Pt precursor/SiO_2 = 0.05) was added to the contents of the autoclave. This autoclave was sealed again, heated to 383 K, and held at this temperature for 10 days (X-ray diffraction patterns, Figure 4.S3). The Pt encapsulation selectivity parameter for this sample was 5.0 (Table 4.5), compared to the much smaller values for the synthesis protocols described earlier in this section (0.85–0.98; M1–M4, Table 4.5). The modest encapsulation selectivity in this case indicates that Pt clusters were preferentially encapsulated within MFI voids. This encapsulation selectivity value, however, is much smaller than that achieved by interzeolite transformation protocols (8-23; Table 4.4), where the large pore zeolites containing metal clusters were converted to MFI, while retaining the encapsulation.

Lower temperatures and OH^- concentrations, as well as the substitution of OH^- with F^-, were also explored. At the low temperature and pH of region I (403-523 K, 7-11, Figure 4.4), metal precursors are stable but so are the silicate species that assemble into MFI frameworks, causing synthesis times, in this case, to be very long, in some reported cases on the order of several months [37].

Region IV (Figure 4.4) involves the use of fluoride instead of hydroxide anions, which leads to MFI synthesis mixtures at near neutral pH conditions [22]; these conditions are likely to preserve metal precursors in solution throughout hydrothermal crystallization of MFI structures. Indeed, such synthesis protocols (M6, Table 4.5; 443 K, pH 7), in the presence of $Pt(NH_3)_4(NO_3)_2$precursors (Pt precursor/SiO_2 = 0.05, Table 4.5), led to an even higher encapsulation selectivity parameter (ϕ = 12; Table 4.5) than the delayed introduction protocols described in the previous paragraph. The fraction of the metal in the synthesis mixture that was retained in the solids products (0.08), however, was very small, leading to Pt contents below 0.1% wt (from ICP analysis) in the final Pt/MFI sample. We conclude that the neutral pH conditions allowed by the use of F^- anions prevented the precipitation of metal precursors as hydroxides, but also appeared to cause the replacement of the ligands in the solvated precursors with F^- anions, possibly leading to the formation of neutral or anionic complexes that resisted occlusion within MFI nuclei as they incipiently formed.

Thus, encapsulation was achieved via direct hydrothermal synthesis protocols by introducing metal precursors later in the zeolite synthesis or by decreasing the pH using F^- instead of OH^-as mineralizing agents. These methods led to modest encapsulation selectivities (ϕ = 5-12; Table 4.5) using delayed precursor addition and direct hydrothermal synthesis in fluoride media and to low encapsulation yields (Pt contents < 0.1% wt) using fluoride synthesis. Interzeolite transformation protocols, in contrast, circumvent the encapsulation challenges in direct hydrothermal syntheses and, in doing so, provide a general method for the encapsulation of metal clusters within the voids of MFI crystals with high selectivities (ϕ = 8-23; Table 4.4) and metal contents (1.01-1.55% wt; Table 4.2); such protocols merely require that such cations be able to exchange into a parent zeolite with voids larger than MFI and exhibiting a lower framework density (here BEA or FAU), which can be subsequently converted into a daughter zeolite (here MFI), for which exchange or more direct methods of encapsulation are not feasible. It seems reasonable to infer that such interzeolite transformation approaches for the containment of metal clusters can be generally extended to any metals with cationic complexes in aqueous media and to any interconversions that increase zeolite framework density, whether they occur spontaneously or through the use of kinetic aids (e.g., seeds or organic structure-directing agents) under hydrothermal conditions.

4.4 Conclusion

Successful encapsulation of metal clusters (Pt, Ru, Rh) within MFI voids was achieved via interzeolite transformations of metal containing BEA or FAU zeolites, by low temperature hydrothermal synthesis with controlled point of addition of metal precursors, and direct hydrothermal synthesis in fluoride media. Interzeolite transformations provide an opportunity to synthesize zeolites with less time and cost, and represent a more economical and environmentally conscious approach, compared to direct hydrothermal synthesis methods, and do so by assisting the nucleation of the desired product zeolite and avoiding the use of organic structure directing agents during synthesis. These interzeolite transformation methods also led to the successful encapsulation of metal clusters within MFI zeolites, where encapsulation was not otherwise feasible by developed protocols involving direct hydrothermal synthesis with ligand-stabilized metal precursors and post-synthesis exchange. X-ray diffraction, electron microscopy, and H_2 chemisorption measurements, when combined, confirmed the transformation of parent zeolites to MFI and the presence of small, uniform, and clean metal clusters. The relative rates of hydrogenation of toluene and 1,3,5-TMB on metal clusters dispersed on MFI and SiO_2 showed that the metal clusters in the zeolitic samples reside predominately within MFI voids, where they were accessible only to the smaller toluene reactant. We expect that the developed interzeolite transformation approach for the synthesis of MFI with/without encapsulated metal clusters can be extended further to zeolites of different frameworks, void environments, and framework compositions and to encapsulate clusters of other metals, metal oxides, and metal sulfides of catalytic importance.

4.5 Acknowledgments

We thank Reena Zalpuri (EML lab) for help with the TEM instrument and Chevron Energy Technology Company for the financial support for this research.

4.6 Figures, Tables and Scheme

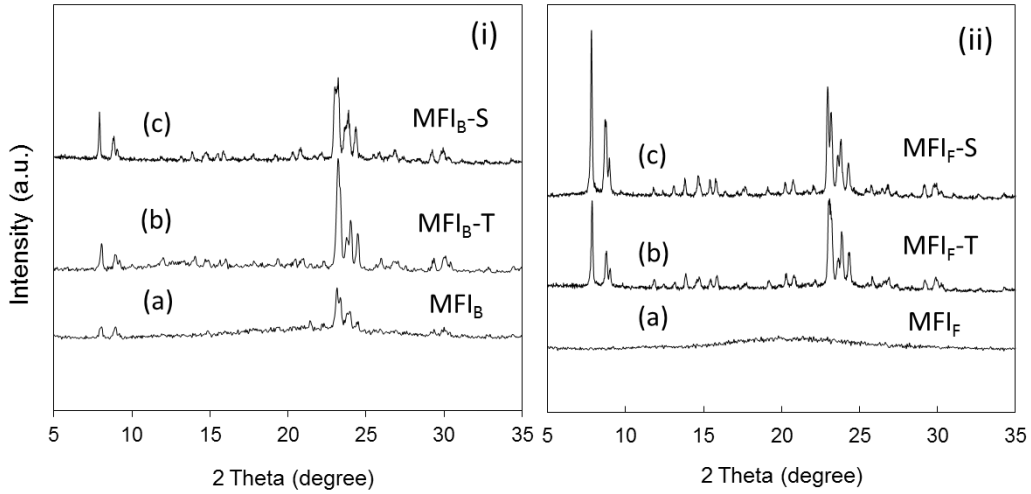

Figure 4.1 X-ray diffraction patterns of MFI products synthesized from (i) BEA (Si/Al = 37.5) and (ii) FAU (Si/Al = 40) parent zeolites via (a) direct, (b) template-assisted (using TPABr), and (c) seed-assisted transformations (using MFI seeds). Syntheses were carried out at molar ratio 0.35 NaOH: 1.0 SiO_2: 0.0133 Al_2O_3: 65 H_2O for 24 h from parent BEA and 0.5 NaOH: 1.0 SiO_2: 0.0125 Al_2O_3: 95 H_2O for 40 h from parent FAU at 423 K (Table 4.1). Product yields are shown in Table 4.1.

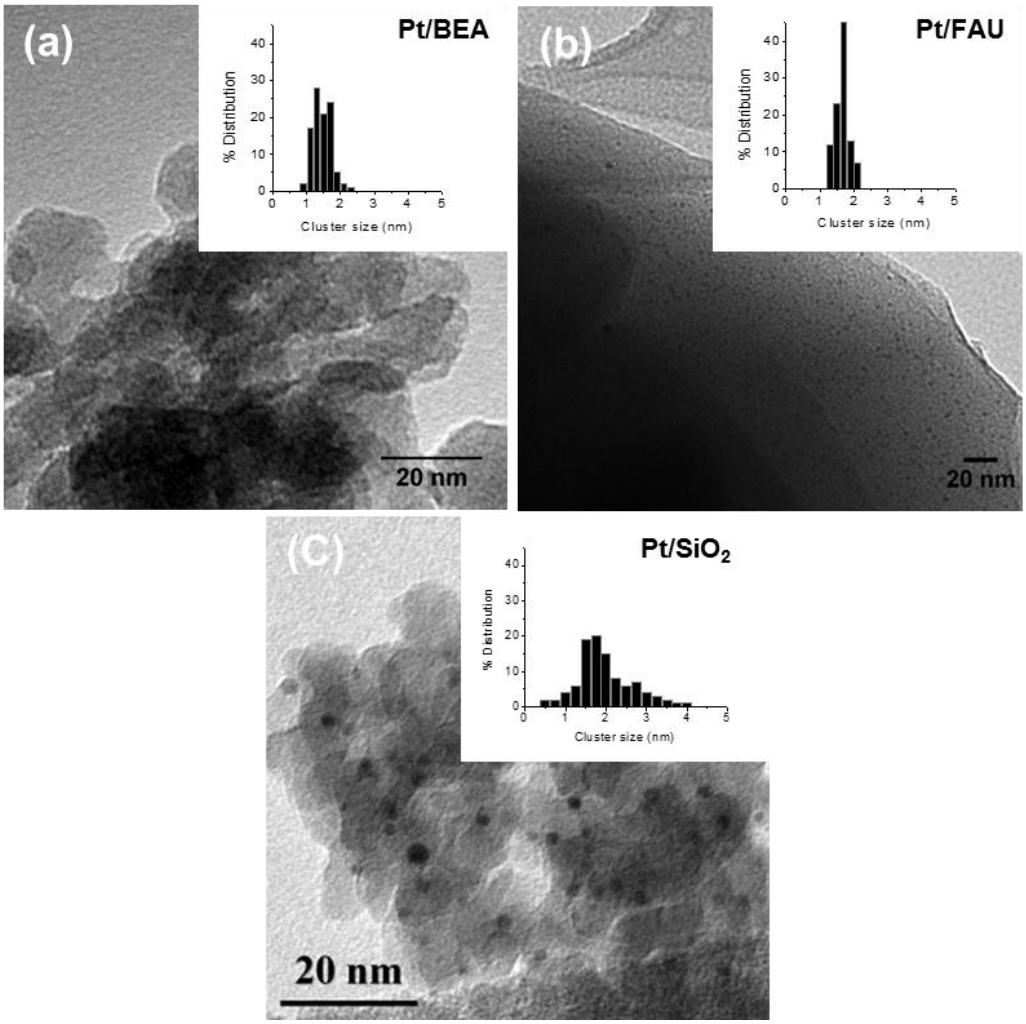

Figure 4.2 TEM images and metal cluster size distributions of parent (a) BEA and (b) FAU zeolites containing Pt clusters, synthesized by ion exchange methods and (c) Pt clusters dispersed on SiO_2, synthesized by incipient wetness impregnation method.

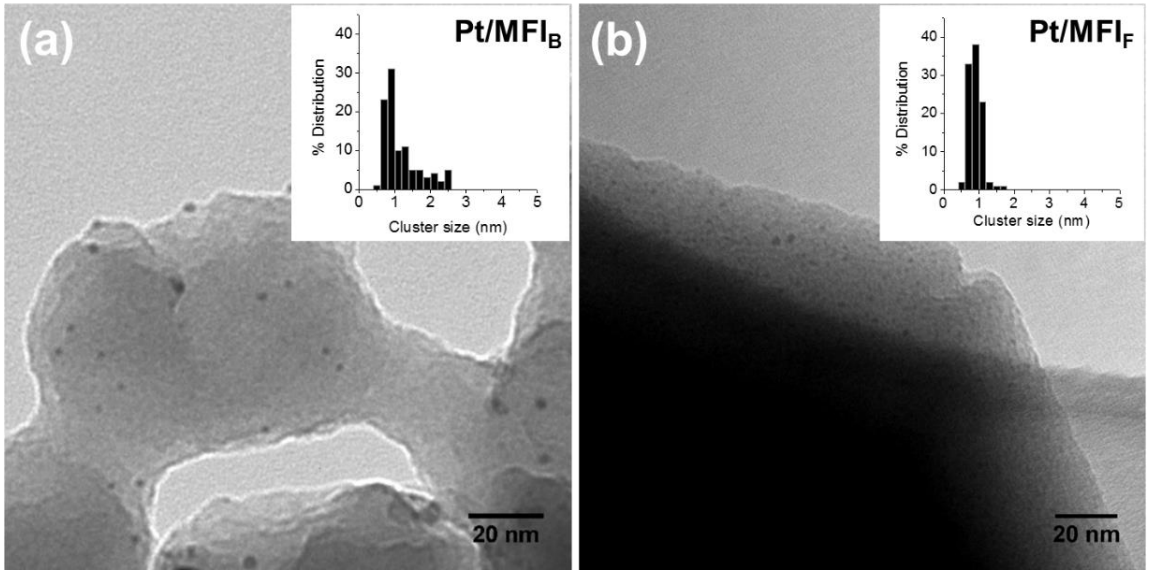

Figure 4.3 TEM images and metal cluster size distributions of Pt containing MFI samples synthesized by interzeolite transformations of (a) BEA and (b) FAU zeolites containing Pt clusters as parent materials.

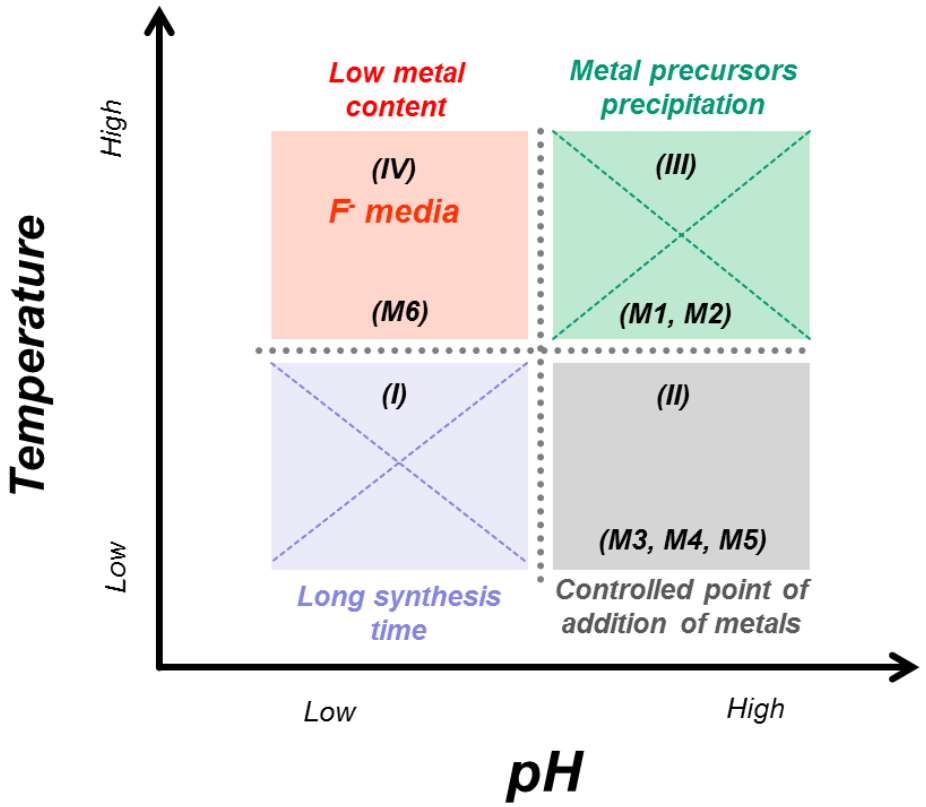

Figure 4.4 Schematic representation of the synthesis factors that limit encapsulation of metal clusters within MFI over a broad range of synthesis conditions. Where, Mi represents the synthesis method used (Table 4.5).

Table 4.1 Initial synthesis molar compositions of the samples.[a]

Sample Name	Parent zeolite (Si/Al)	Time of Synthesis (h)	Additional (SDA/Seed)[b]	Product Phase	Yield[c] (%)	Product (Si/Al)[d]
MFI_B	BEA(37.5)	24	-	MFI	46.4	22
MFI_B-T	BEA(37.5)	24	TPABr (0.05)[e]	MFI	47.3	35
MFI_BS	BEA(37.5)	24	10% wt. MFI Seeds	MFI	47.1	23
Pt/MFI_B	Pt/BEA(37.5)	30	-	MFI	47.7	-
Ru/MFI_B	Ru/BEA(37.5)	30	-	MFI	47.3	-
MFI_F	FAU(40)	40	-	Amor.	75.5	-
MFI_F-T	FAU(40)	40	TPABr (0.05)[e]	MFI	57.9	33
MFI_F-S	FAU(40)	40	10% wt. MFI Seeds	MFI	47.1	22
Pt/MFI_F	Pt/FAU(40)	40	10% wt. MFI Seeds	MFI	48.5	29
Ru/MFI_F	Ru/FAU(40)	40	10% wt. MFI Seeds	MFI	56.8	25
Rh/MFI_F	Rh/FAU(40)	40	10% wt. MFI Seeds	MFI	56.2	28

[a] Molar ratios 0.35NaOH: 1.0SiO_2: 0.0133 Al_2O_3: 65H_2O for transformations of BEA and 0.5NaOH: 1.0SiO_2: 0.0125 Al_2O_3: 95H_2O from FAU at 423 K and excludes the SiO_2 amount of seed materials.

[b] $Seed\ (wt.\%) = \frac{Seed\ material\ (g)}{Parent\ zeolite\ (g)}\ x\ 100$

[c] $yield\ (\%) = \frac{Product\ (g)}{Parent\ zeolite\ (g)+Seed\ (g)}\ x\ 100$

[d] Analyzed by inductively coupled plasma optical emission spectroscopy.

[e] Values in parentheses show molar composition of TPABr relative to SiO_2.

Table 4.2 Metal loadings, dispersions, mean sizes, and dispersity of metal clusters dispersed on SiO_2, BEA, FAU, and MFI.

Sample	Metal loading (% wt.)[a]	D[b]	d_{chem}[c] (nm)	d_{TEM}[d] (nm)	Dispersity Index (DI)
Pt/SiO_2	0.79	0.61	1.8	2.4	1.96
Ru/SiO_2	0.51	0.22	3.7	4.8	-
Rh/SiO_2	1.10	0.60	1.8	2.1	-
Pt/BEA	0.85	0.88	1.3	1.6	1.07
Ru/BEA	0.64	0.63	1.4	1.4	1.08
Pt/FAU	1.23	0.78	1.4	1.7	1.03
Ru/FAU	0.95	0.59	1.5	1.7	1.16
Rh/FAU	0.80	0.85	1.3	1.5	1.09
Pt/MFI_B	1.01	0.80	1.4	1.7	1.41
Ru/MFI_B	1.23	0.70	1.2	1.3	1.16
Pt/MFI_F	1.23	0.75	1.5	1.0	1.09
Ru/MFI_F	1.33	0.72	1.2	1.5	1.16
Rh/MFI_F	1.55	0.96	1.1	1.5	1.09

[a]Analyzed by inductively coupled plasma optical emission spectroscopy.
[b] Metal dispersion estimated from H_2 chemisorptions.
[c]Mean cluster diameter estimated from the metal dispersion obtained from H_2 chemisorption measurements [23].
[d] Surface-area-weighted mean cluster diameter (d_{TEM}) estimated from TEM analysis, $d_{TEM} = \sum n_i d_i^3 / \sum n_i d_i^2$ [25], the mean cluster diameters of metal supported on SiO_2 samples are quoted from [16].

Table 4.3 Catalytic properties of metal containing BEA, FAU and SiO_2 samples in hydrogenation of arenes.[a]

Sample	$r_{toluene}$[b] (mol ($mol_{surf\text{-}metal}^{-1}$ s^{-1}))	$r_{1,3,5\text{-}TIPB}$[b] (mol ($mol_{surf\text{-}metal}^{-1}$ s^{-1}))	χ_j[c] j=zeolite, SiO_2	ϕ[d]
Pt/BEA	1.26	0.007	180.0	40.9
Pt/FAU	1.28	0.008	160.0	36.4
Pt/SiO_2	1.35	0.306	4.4	1.0
Ru/BEA	0.112	0.001	112.0	14.3
Ru/FAU	0.120	0.001	120.0	15.4
Ru/SiO_2	0.173	0.022	7.8	1.0
Rh/FAU	0.019	0.0003	63.3	21.8
Rh/SiO_2	0.023	0.008	2.9	1.0

[a] Hydrogenations were carried out with 0.35 kPa toluene/0.15 kPa 1,3,5-TIPB and 100 kPa H_2 at 473 K.
[b] Reaction turnover rate is defined as mole of reactant converted per mol of surface metal atoms per second.
[d] $\chi_j = r_{toluene}/r_{1,3,5\text{-}TIPB}$, j=zeolite, SiO_2.
[d] $\phi = \chi_{zeolite}/\chi_{SiO_2}$

Table 4.4 Catalytic properties of metal containing MFI and SiO_2 samples in hydrogenation of arenes.[a]

Sample	$r_{toluene}$[b] (mol ($mol_{surf\text{-}metal}^{-1}$ s^{-1}))	$r_{1,3,5\text{-}TMB}$[b] (mol ($mol_{surf\text{-}metal}^{-1}$ s^{-1}))	χ_j[c] j=MFI, SiO_2	ϕ[d]
Pt/MFI_B	1.12	0.05	22.4	8.3
Pt/MFI_F	0.50	0.01	50.0	18.5
Pt/SiO_2	1.35	0.50	2.7	1.0
Ru/MFI_B	0.015	0.0001	150.0	22.7
Ru/MFI_F	0.012	0.0002	60.0	9.1
Ru/SiO_2	0.173	0.0260	6.6	1.0
Rh/MFI_F	0.017	0.001	17.0	8.1
Rh/SiO_2	0.023	0.011	2.1	1.0

[a] Hydrogenations were carried out with 0.35 kPa toluene/0.26 kPa 1,3,5-TMB and 100 kPa H_2 at 473 K.
[b] Reaction turnover rate is defined as mole of reactant converted per mol of surface metal atoms per second.
[d] $\chi_j = r_{toluene}/r_{1,3,5\text{-}TMB}$, j=MFI, SiO_2.
[d] $\phi = \chi_{MFI}/\chi_{SiO_2}$.

Table 4.5 Synthesis procedures and encapsulation selectivities for metal-containing MFI synthesized by direct hydrothermal syntheses.

Name	Sample	Composition	Metal precursor (composition)[a]	T (K)	t[b] (d)	Preparation method	Φ[c]	Comments
M1	Ru/MFI	$70SiO_2 : 1.0Al_2O_3 : 11.5Na_2O : 2800H_2O$	$RuCl_3$ (1.9)	433	3	Direct hydrothermal synthesis with added $RuCl_3$	0.95	Metal precursor decomposed in the synthesis
M2	Pt/MFI	$70SiO_2 : 1.0Al_2O_3 : 11.5Na_2O : 2800H_2O$	$Pt(NH_3)_4(NO_3)_2$ (3.5)	433	3	Direct hydrothermal synthesis with ligand-stabilized metal precursor	0.98	Metal precursor decomposed in the synthesis
M3	Pt/MFI	$0.04TPABr : 0.003Al_2O_3 : 1SiO_2 : 120H_2O : 0.322OH^-$	$Pt(NH_3)_4(NO_3)_2$ (0.05)	383	12	Low T synthesis with excess amount of template	0.85	Competition between metal precursor and SDA
M4	Pt/MFI	$0.02TPABr : 0.003Al_2O_3 : 1SiO_2 : 120H_2O : 0.322OH^-$	$Pt(NH_3)_4(NO_3)_2$ (0.05)	383	15	Low T synthesis with sub-stoichiometric amount of template	0.90	Poor crystallization of resulted MFI, metal precursor precipitation
M5	Pt/MFI	$0.03TPABr : 0.003Al_2O_3 : 1SiO_2 : 120H_2O : 0.322OH^-$	$Pt(NH_3)_4(NO_3)_2$ (0.05)	383	15	Metal precursor added after 5 days of synthesis	5	Successful Encapsulation
M6	Pt/MFI	$0.07TPABr : 1.0TEOS : 0.012NaAlO_2 : 1.2NH_4F : 80H_2O$	$Pt(NH_3)_4(NO_3)_2$ (0.05)	443	7	High T, low pH synthesis in fluoride media	12	Successful encapsulation, low metal loading

[a] Metal precursor molar compositions are reported relative to SiO_2.
[b] t = time required for synthesis in days.
[c] $\phi = \chi_{zeolite}/\chi_{SiO_2}$, $\chi_j = r_{toluene}/r_{1,3,5\text{-}TMB}$, j=MFI, SiO_2.

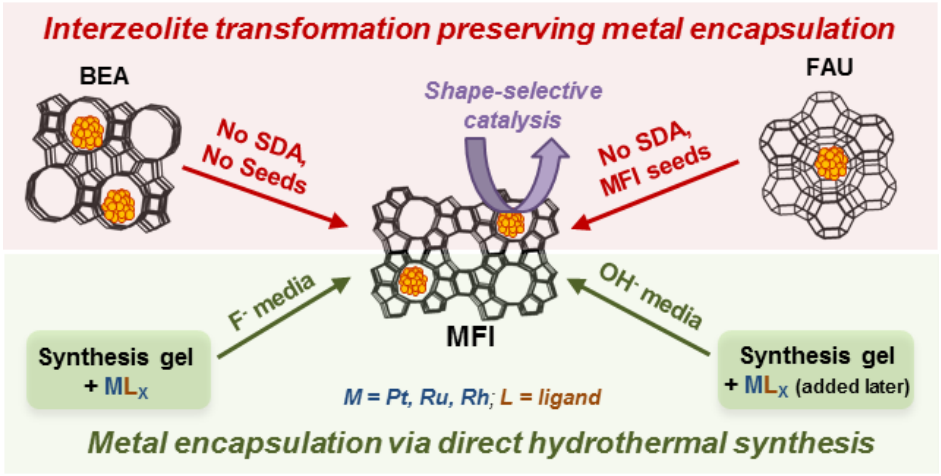

Scheme 4.1 Schematic representation of the encapsulation of metal clusters within MFI via interzeolite transformations and direct hydrothermal syntheses.

4.7 Supporting Information

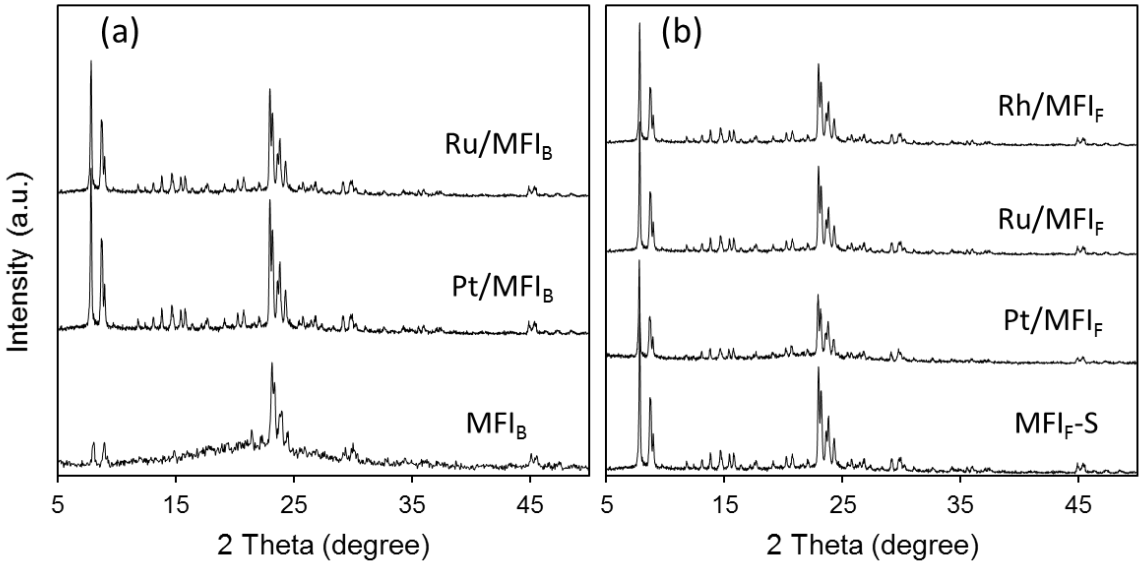

Figure 4.S1 X-ray diffraction patterns of MFI products synthesized by interzeolite transformations of (a) BEA and (b) FAU containing metal clusters as parent zeolites. Syntheses were carried out at molar composition 0.35NaOH: 1.0SiO_2: 0.0133Al_2O_3: 65.0H_2O from BEA without seeds and 0.50NaOH: 1.0SiO_2: 0.0125Al_2O_3: 95.0H_2O from FAU with 10 % wt. MFI seeds at 423 K (Table 4.1).

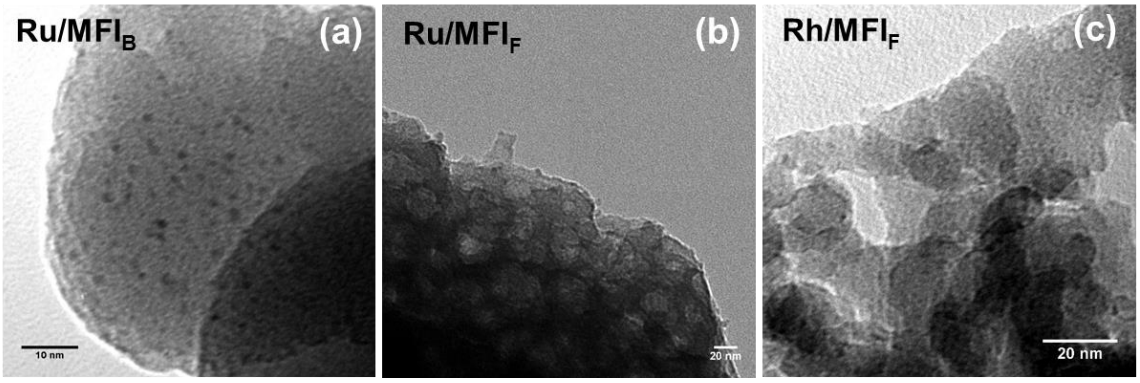

Figure 4.S2 TEM images of MFI zeolites containing (a) Ru clusters, synthesized by transformations of Ru/BEA, and (b) Ru and (c) Rh clusters, synthesized by transformations of Ru/FAU and Rh/FAU as parent zeolites, respectively.

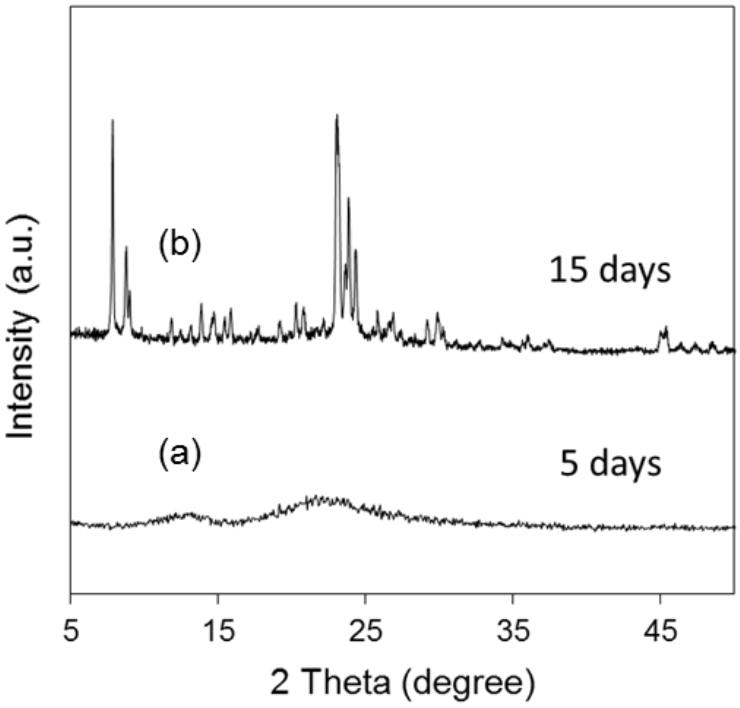

Figure 4.S3 X-ray diffraction pattern of the product obtained after (a) 5 and (b) 15 days of hydrothermal synthesis using method M5 (Table 4.5). The synthesis was carried out at molar composition of the gel 0.03TPABr: $0.003Al_2O_3$: $1.0SiO_2$: $120H_2O$: $0.322OH^-$: $0.05Pt(NH_3)_4(NO_3)_2$ at 383 K.

4.7 References

(1) Csicsery, S. M. *Zeolites* 1984, 4, 202.
(2) Weisz, P. B.; Frilette, V. J.; Maatman, R. W.; Mower, E. B. *J. Catal.* 1962, 1, 307.
(3) Davis, M. E.; Lobo, R. F. *Chem. Mater.* 1992, *4*, 756.
(4) Davis, M. E. *Chem. Mater.* 2014, 26, 239-245.
(5) Bhan, A.; Tsapatsis, M. *Curr. Opin. Chem. Eng.* 2013, 2 (3), 320-324.
(6) Moliner, M.; Martínez, C.; Corma, A. *Chem. Mater.* 2014, 26, 246-258.
(7) Gates, B. C. *Chem. Rev.* 1995, *95*, 511.
(8) Flytzani-Stephanopoulos, M.; Gates, B. C. *Annu. Rev. Chem. Biomol. Eng.* 2012, *3*, 545.
(9) Wu, J. C. S.; Goodwin Jr., J. G.; Davis, M. *J. Catal.* 1990, 125, 488.
(10) Gallezot, P. *Post-Synthesis Modification I* 2002, 257.
(11) Sachtler, W. M. H. *Acc. Chem. Res.* 1993, 26, 383.
(12) Guczi, L.; Kiricsi, I. *Appl. Catal., A* 1999, 186, 375.
(13) Zhan, B.-Z.; White, M. A.; Sham, T. K.; Pincock, J. A.; Doucet, R. J.; Rao, K. V. R. Rao, Robertson, K. N.; Cameron, T. S. *J. Am. Chem. Soc.* 2003, 125, 2195.
(14) Altwasser, S.; Gläser, R.; Lo, A. S.; Liu, P.-H.; Chao, K.-J.; Weitkamp, J. *Micropor. Mesopor. Mater.* 2006, 89, 109.
(15) Zhan, B.-Z.; Iglesia, E. *Angew. Chem. Int. Ed.* 2007, *46*, 3697-3700.
(16) Choi, M.; Wu, Z.; Iglesia, E. *J. Am. Chem. Soc*. 2010, 132, 9129.
(17) Wu, Z.; Goel S.; Choi, M.; Iglesia, E. *J. Catal.* 2014, 311, 458-468.
(18) Goel, S.; Wu, Z.; Zones, S. I.; Iglesia, E. *J. Amer. Chem. Soc.* 2012, *134* (42), 17688.
(19) Zones, S. I. *J. Chem. Soc., Faraday Trans*. 1991, 87, 3709.
(20) Sano T., Itakura M., Sadakane M. *J. Japan Petro. Inst.* 2013, 56 (4), 183-197.
(21) Kiyozumi, Y.; Suzuki, K.; Shin, S.; Okado, H.; Noguchi, K. US4579994 A, April 1, 1986.
(22) Louis, B.; Kiwi-Minsker, L. Microporous Mesoporous Mater. 2004, 74, 171.
(23) Bergeret, G.; Gallezot, P. In *Handbook of Heterogeneous Catalysis;* Wiley-VCH Verlag GmbH & Co. KgaA: New York, 2008.
(24) Stepto, R. F. T. *Pure Appl. Chem.* 2009, 81, 351.
(25) Schneider, M.; Duff, D.; Mallat, T.; Wildberger, M.; Baiker, A. *J. Catal*. 1994, 147, 500.
(26) Somiya, S., Ed. *Handbook of Advanced Ceramics: Materials, Applications, Processing, and Properties*; Academic Press: Waltham, MA, 2013.
(27) Caro, J.; Noack, M. In *Advances in Nanoporous Materials*; Ernst, S., Ed.; Elsevier: New York, 2010; Vol. 1, pp 1–96.
(28) Baerlocher, C.; McCusker, L. B. Database of Zeolite Structures: http://www.iza-structure.org/databases/.
(29) Maldonado, M.; Oleksiak, M. D.; Chinta, S.; Rimer, J. D. *J. Am. Chem. Soc.* 2013, *135*, 2641.
(30) Itabashi, K.; Kamimura, Y.; Iyoki, K.; Shimojima, A.; Okubo, T. A *J. Amer. Chem. Soc*. 2012, 134, 11542.
(31) Iyoki, K.; Itabashi, K.; Okubo, T. *Microporous Mesoporous Mater.* 2014, *189*, 22.
(32) Xie, B.; Song, J.; Ren, L.; Ji, Y.; Li, J.; Xiao, F.-S. *Chem. Mater.* 2008, 20, 4533.
(33) Moore, R. M.; Katzer, J. R. *AIChE J.* 1972, *18*, 816.

(34) Davis T. M., Drews T. O., Ramanan H., He C., Dong J., Schnablegger H., Katsoulakis M. A., Kokkoli E., McCormick A. V., Penn R. L., Tsapatsis M. *Nat Mater* 2006, 5, 400-408.
(35) Cundy, C. S.; Cox, P. A. *Microporous Mesoporous Mater.* 2005, 82, 1.
(36) Barrer, R. M. *Zeolite Synthesis*; American Chemical Society: Washington, DC, 1989; Vol. 398, p 11.
(37) Auerbach, S. M.; Carrado, K. A.; Dutta, P. K. Handbook of Zeolite Science and Technology; CRC Press: Boca Raton, FL, 2003.

Chapter 5

Synthesis of Zeolites via Interzeolite Transformations without Organic Structure-Directing Agents

Abstract

We report synthetic protocols and guiding principles inspired by mechanistic considerations for the synthesis of crystalline microporous solids via interzeolite transformations that avoid direct intervention by organic structure-directing agents. These protocols are specifically implemented to synthesize high-silica MFI (ZSM-5), CHA (chabazite), STF (SSZ-35), and MTW (ZSM-12) zeolites from FAU (faujasite) or BEA (beta) parent materials. These transformations succeed when they lead to daughter structures with higher framework densities, and their nucleation and growth become possible by the presence of seeds or of structural building units common to the parent and target structures, leading, in the latter case, to spontaneous transformations by choosing appropriate synthesis conditions. These protocols allow the synthesis of high-silica frameworks without the use of organic templates otherwise required. The $NaOH/SiO_2$ ratio and Al content in reagents are used to enforce synchronization between the swelling and local restructuring within parent zeolite domains with the spalling of fragments or building units from seeds of the target structure. Seed-mediated interconversions preserve the habit and volume of the parent crystals because of the incipient nucleation of the target structure at the outer regions of the parent domains. The pseudomorphic nature of these transformations requires the concurrent nucleation of mesopores within daughter zeolite crystals because their framework density is larger than that for the parent zeolites. The approach and evidence described shows, for the first time, that a broad range of zeolites rich in silica, and thus more useful as catalysts, can be made without the organic templates originally used to discover them.

5.1 Introduction

Aluminosilicate zeolites are crystalline microporous solids with diverse framework structures and void networks constructed by arrangements of SiO_4^{4-} and AlO_4^{5-} tetrahedral units; these materials are widely used in adsorption, catalysis, and ion-exchange processes [1-4]. Zeolites are typically synthesized by hydrothermal treatment of amorphous aluminosilicate gels in the presence of inorganic (e.g., Na^+, K^+, etc.) and/or organic structure-directing agents (OSDA) in hydroxide or fluoride media [5-8]. OSDA reagents, in particular, increase the cost and the environmental burden of many large-scale zeolite syntheses.

Much effort has been devoted to the development of OSDA-free synthesis protocols to decrease such costs as well the emissions of toxic species in gaseous and water streams generated during the synthesis or subsequent treatments required to decompose organic species contained within zeolite voids. The assembly-disassembly-organization-reassembly (ADOR) mechanism has been developed recently [9, 10] as a method of zeolite manipulation without OSDA, in which the selective disassembly of a parent zeolite followed by reassembly can lead to a new topology, but the method is limited in application, as the parent zeolite requires the presence of a hydrolytically sensitive dopant element (e.g., Ge) incorporated within the framework at a specific site, which

allows the chemically selective removal of the units containing the dopant. Recently, several groups have reported improved protocols for seed-assisted hydrothermal synthesis of zeolites from amorphous aluminosilicate gels without the use of OSDA species [11-17]. These methods use large concentrations of alkali cations to stabilize the target frameworks and, as a result, have succeeded mostly in the synthesis of Al-rich frameworks (Si/Al < 10). Similar protocols remain unavailable for OSDA-free synthesis of target zeolites (e.g., CHA, STF, MTW, MFI, etc.) with lower Al content, which are often preferred because of their greater structural and acid site stability. In some instances, it has not even been possible to form some target frameworks (e.g., STF, MTW, etc.) with Si/Al ratios below 10.

Zeolites are kinetically (but not thermodynamically) stable toward conversion to denser framework structures (e.g., α-quartz); as a result, their synthesis often involves the formation of structures of intermediate stability in the course of forming the ultimate target structures, which are often rendered stable only by the use of specific organic or inorganic cations. Transformations of one zeolite structure into another, interzeolite transformations, have been explored because they can provide a strategy for the selective synthesis of specific structures, often with shorter synthesis times; the mechanistic details of such interzeolite transformations, however, remain unclear [17-25], and predictions of their success remain largely empirical.

Most reported interconversions use OSDA moieties to induce the nucleation of frameworks that are in fact of lower framework densities and thus less stable than that of the parent zeolite [26, 27] or to form structures that would not form at all without the presence of an OSDA [27, 28]. Several studies have used seeds to assist the formation of desired structures without the aid of OSDA species [18, 20, 22, 24, 25], and others have induced interzeolite transformations in the presence of both seeds and OSDA [19, 22, 28]. Successful interzeolite transformations without either seeds or OSDA have been reported only for zeolites with low Si/Al ratios (Si/Al = 4-10) [21-23]; to date, target materials with higher Si/Al ratios (Si/Al > 10) do not appear to have been synthesized via interzeolite transformations without the aid of OSDA species.

The present study reports the successful synthesis of high-silica (Si/Al = 11–23) MFI, CHA, STF, and MTW zeolites via OSDA-free interzeolite transformation methods (Scheme 5.1). Parent zeolites BEA (framework density (FD) 15.3; defined as T atom/nm^3, where T stands for Si or Al atoms in the zeolite framework [29]) or FAU (FD 13.3) were transformed into target daughter structures MFI (FD 18.4), CHA (FD 15.1), STF (FD 16.9), or MTW (FD 18.2) via recrystallization in aqueous NaOH under hydrothermal conditions. Structures with lower framework densities were successfully transformed into more stable structures with higher framework densities. Concomitant kinetic hurdles required the presence of a common composite building unit (CBU) between parent and target structures or, in their absence, the addition of either seeds or OSDA moieties for successful transformations.

We propose a plausible synthesis mechanism, pseudomorphic in nature, for seed-assisted transformations that is consistent with the observed effects of the parent Si/Al ratio, the $NaOH/SiO_2$ ratio, and the required synthesis temperature and time, as well as with the crystal habit and intracrystal mesoporous voids in the daughter structures. The resulting concepts and strategies provide predictive guidance for synthesizing a broad range of zeolite frameworks in the direction

dictated by thermodynamics and with kinetics mediated by either common structural units along the reaction coordinate or by seeds of the target product.

5.2 Experimental Section

5.2.1 Reagents and Materials. Fumed SiO_2 (Cab-O-Sil, HS-5, 310 $m^2\ g^{-1}$), NaOH (99.995%, Sigma Aldrich), FAU (CBV780, Zeolyst, Si/Al = 40, H-FAU), FAU (CBV712, Zeolyst, Si/Al = 6, NH_4^+-FAU), BEA (CP811E-75, Zeolyst, Si/Al = 37.5, H-BEA), BEA (CP814E, Zeolyst, Si/Al = 12.5, NH_4^+-BEA), and tetrapropylammonium bromide (TPABr, 98%, Sigma Aldrich) were used as received.

5.2.2 Synthesis Procedures

5.2.2.1 MFI, CHA, STF and MTW Seeds. The materials used as seeds were prepared using previously described synthesis procedures for MFI (S_1) [30], CHA [31], STF [32] and MTW [33] zeolites. MFI (S_2) was synthesized by dissolving $Al(OH)_3$ (53% Al_2O_3, Reheis F-2000 dried gel, 0.44 g) in a solution containing deionized H_2O (38 g), tetrapropyl ammonium hydroxide (TPAOH, 40 wt%, Aldrich, 7.5 g) and KOH (1 M solution in deionized H_2O, Fisher, 15 g). Ludox AS-30 colloidal silica (18 g) was added to the solution and the mixture was then transferred into a Teflon-lined stainless steel autoclave (Parr, 125 cm^3) and held at 423 K for 3 days under static conditions. The resulting solids were collected by filtration through a fritted disc Buchner filter funnel (Chemglass, 150 ml, F) and washed with deionized water (17.9 MΩ·cm resistivity) until the rinse liquids reached a pH of 8-9 and the sample was heated in convection oven at 373 K overnight.

5.2.2.2 Synthesis of MFI via Transformations of BEA or FAU Zeolites. In a typical synthesis, zeolite BEA or FAU was added (0.5-1.0 g) to an aqueous NaOH solution, into which the MFI seed crystals or structure-directing agents (TPABr) were added to prepare final mixtures with molar compositions listed in Table 5.1. These mixtures were placed within sealed polypropylene containers (Nalgene, 125 cm^3) and homogenized by vigorous magnetic stirring (400 rpm; IKA RCT Basic) for 1 h at ambient temperature. The mixture was then transferred into a Teflon-lined stainless steel autoclave and held at 423 K for 24-40 h under static conditions. The resulting solids were collected by filtration through a fritted disc Buchner filter funnel (Chemglass, 150 ml, F) and washed with deionized water (17.9 MΩ·cm resistivity) until the rinse liquids reached a pH of 8-9. The sample was heated in a convection oven at 373 K overnight. The solid yields of the resulting products were defined as

$$Yield\ (\%) = \frac{Product\ (g)}{Parent\ zeolite\ (g) + Seeds\ (g)} \times 100 \qquad (1)$$

The samples were then treated in a tube furnace in flowing dry air (1.67 $cm^3\ g^{-1}\ s^{-1}$) to 623 K at 0.03 $K\ s^{-1}$ and held at this temperature for 3 h. The samples, after treatment, were denoted as MFI_B-D, MFI_B-T, MFI_B-S, when synthesized from BEA, and MFI_F-D, MFI_F-T, MFI_F-S, when synthesized from FAU, in the direct (-D), template-assisted (-T), and seed-assisted (-S) interzeolite transformations, respectively.

5.2.2.3 Synthesis of CHA, STF and MTW via Transformations of FAU. The synthesis of CHA, STF, and MTW zeolites was achieved by transformations of FAU as parent material. FAU (0.5-

1.0 g) was added to an aqueous NaOH solution to achieve molar compositions of *x* NaOH: 1.0 SiO_2: 0.0125 Al_2O_3: 95 H_2O (*x* = 0.50, 0.68, 0.85), into which 10% wt. (% wt. based on parent FAU) seed crystals (CHA, STF, or MTW) were added to prepare final mixtures with molar compositions listed in Table 5.2. These mixtures were placed within sealed polypropylene containers (Nalgene, 125 cm^3) and homogenized by vigorous magnetic stirring (400 rpm; IKA RCT Basic) for 1 h at ambient temperature. These mixtures were then transferred into a Teflon-lined stainless steel autoclave and held at the desired crystallization temperature (423, 428, or 433 K) for 40 h under static conditions. The resulting solids were collected by filtration through a fritted disc Buchner filter funnel (Chemglass, 150 ml, F) and washed with deionized water (17.9 MΩ·cm resistivity) until the rinse liquids reached a pH of 8-9. The samples were heated in a convection oven at 373 K overnight. The samples were then treated in tube furnace in flowing dry air (1.67 $cm^3\,g^{-1}\,s^{-1}$) to 873 K at 0.03 K s^{-1} and held at this temperature for 10 h. The resulting samples after treatment were denoted as CHA_F-S, STF_F-S, MTW_F-S, synthesized via interzeolite transformations of FAU using seeds of CHA, STF, and MTW, respectively.

For the synthesis of the H-form of these zeolites, the treated Na-zeolite samples were added to an aqueous NH_4NO_3 solution (>98%, Sigma-Aldrich, 1 g zeolite per 100 cm^3 of 0.1 M solution) while stirring at 353 K for 4 h. The solids were recovered by filtration, and this process was repeated two more times to yield NH_4-zeolite. The resulting samples were then treated in tube furnace in flowing dry air (1.67 $cm^3\,g^{-1}\,s^{-1}$) to 873 K at 0.03 K s^{-1} and held at this temperature for 3 h to form H-zeolite.

5.2.3 Characterization of Framework Structures and Crystallinity. The identity and phase purity of the product zeolites were demonstrated by powder X-ray diffraction (XRD) measurements (Cu Kα radiation λ=0.15418 nm, 40 kV, 40 mA, Bruker D8 Advance). Diffractograms were collected for 2Θ values of 5-35^o at 0.02^o intervals with a 2 s scan time. The crystallinity was calculated using MgO as an internal standard in powder XRD. The ratio of the sum of areas of three major peaks in the target material to that of their corresponding seed material (100% crystalline) was defined as the percentage crystallinity of each sample. Si, Al, and Na contents of the samples were measured by ICP-AES (IRIS Intrepid spectrometer; Galbraith Laboratories). TEM images were taken on Philips/FEI Tecnai 12 microscope operated at 120 kV. Before TEM analysis, the samples were suspended in ethanol and dispersed onto ultrathin carbon/holey carbon films supported on 400 mesh Cu grids (Ted Pella Inc.). Nitrogen and argon adsorption-desorption measurements of zeolite products were performed on ASAP 2020 (Micromeritics) at 77 and 87 K, respectively. Prior to the measurements, all samples were degassed at 623 K for 4 h under vacuum. The final pH values were measured at ambient temperature using an Orion Ross combination electrode (Orion 8103BNUMP) with an Orion Star A215 meter (calibrated using buffer solutions of pH 7.00, 10.01 and 12.00).

5.3 Results and Discussion

5.3.1 Synthesis of MFI via Transformations of Parent BEA

Parent BEA zeolites with low Si content (Si/Al = 12.5) formed only amorphous solids in aqueous NaOH ($NaOH/SiO_2$ = 0.35, H_2O/SiO_2 = 65; Table 5.1) at 423 K under hydrothermal conditions (X-ray diffractogram; Figure 5.1(i)a); MFI frameworks preferentially form in gels with

high Si/Al contents because abundant five-membered rings in MFI are disfavored at high Al contents [34].

MFI crystals readily formed, however, from parent BEA zeolites with lower Al contents (Si/Al = 37.5; X-ray diffractogram; Figure 5.1(i)b, 46% yield (eq 1); Table 5.1) in aqueous NaOH solution ($NaOH/SiO_2$ = 0.35, H_2O/SiO_2 = 65; Table 5.1) under autogenous pressures at 423 K. Interestingly, this transformation occurred spontaneously, without requiring the presence of either seeds or OSDA. The Si/Al ratio in the MFI product (Si/Al = 22; Table 5.1) was lower than in the parent BEA (Si/Al = 37.5), and the solids yield was 46% (Table 5.1), suggesting that nearly all of the Al in the parent BEA was incorporated into the product MFI, whereas some SiO_2 remained dissolved in solution at the high final pH (11.8, Table 5.1). Crystalline MFI was obtained also from template-assisted (with TPABr) and seed-assisted (with 10 wt % MFI seeds (S_1)) transformations of parent BEA (Si/Al = 37.5) (X-ray diffractograms; Figure 5.1(i)c, 1(i)d, 47% yield (eq 1) for both; Table 5.1). Thus, we conclude that parent BEA zeolites with high Si content (Si/Al = 37.5) successfully transformed to MFI spontaneously and in the presence of either MFI seeds or OSDA (TPABr) at Si/Al ratios in the parent BEA that favor MFI frameworks.

We note that the framework structures and CBU of the parent BEA and product MFI include a common *mor* structural motif [29]. It seems plausible, therefore, that a CBU, present in BEA and required to form MFI, remains essentially intact within BEA-derived intermediates during the conversion of BEA to MFI; this CBU may assist the local nucleation of MFI and, in doing so, minimize inherent kinetic hurdles and allow BEA to MFI transformations to occur without seeds or OSDA. This common CBU may serve as a kinetic mediator [12, 30] for nucleating the daughter structure, suggesting that zeolites containing common CBU may be able to overcome kinetic barriers that impede their interconversions in the direction dictated by the thermodynamic tendency of zeolites to form structures with greater framework densities. MFI zeolites were obtained after 24 h from parent BEA zeolites (Figure 5.1(i)), whereas hydrothermal MFI syntheses from amorphous aluminosilicate gels, with or without OSDA, typically require 2–15 days [35]. Thus, the presence of the BEA structure, plausibly because of its common CBU with MFI, shortens synthesis times because of rapid nucleation.

Next, we explore the implications of this common CBU hypothesis for assisting nucleation of target frameworks, first by attempting the synthesis of MFI from FAU, within which a common CBU is absent, under similar conditions that led to the spontaneous transformation of BEA into MFI. From these resulting observations, we propose a set of requirements for successful zeolite interconversions and the validation of these guidelines by the synthesis of CHA, STF, and MTW zeolites from parent FAU zeolite.

5.3.2 Synthesis of MFI via Transformations of Parent FAU

Parent FAU zeolites with Si/Al ratios of 6 and 40 gave only amorphous solids in hydrothermal aqueous NaOH environments ($NaOH/SiO_2$ = 0.5, H_2O/SiO_2 = 95; Table 5.1) at 423 K (X-ray diffractograms; Figure 5.1(ii)a,(ii)b), consistent with kinetic hurdles that cannot be overcome despite favorable thermodynamics (FAU, FD 13.3; MFI, FD 18.4), possibly because of the lack of a common CBU. MFI formed, however, when FAU (Si/Al = 40) was treated in similar hydrothermal environments but with TPABr (OSDA) or MFI seeds in the synthesis mixture (X-

ray diffractograms; Figure 5.1(ii)c,(ii)d, 58 and 47% yield (eq 1), respectively; Table 5.1). These findings contrast the ability of BEA precursors to form MFI even in the absence of such kinetic mediation as OSDA or seeds, which are required in the case of parent FAU zeolites, to assist the nucleation of the favored MFI structures. These data, taken together, provide compelling but circumstantial evidence for the role of common CBU motifs in assisting nucleation in lieu of the more frequent strategies that use OSDA or seeds as the nucleation sites or centers.

Figure 5.2 shows TEM images of two MFI seed materials of different crystal size (~6 μm, seed S_1; Figure 5.2a and ~0.2 μm, seed S_2; Figure 5.2b) and of the MFI products formed from FAU parent zeolites using each of these seeds (Figure 5.2c,d, respectively). The crystal habit and size of the MFI products using S_1 (TEM, Figure 5.2c) and S_2 (TEM, Figure 5.2d) seeds are similar (~0.7 μm diameter) and differ markedly from those of the MFI seeds used (TEM, Figure 5.2a,b), which do not remain intact as they mediate MFI nucleation from parent FAU crystals. These seeds do not serve as intact nucleation sites but instead provide CBU species or shed small fragments, as in the case of homogeneous nucleation and growth during seed-assisted hydrothermal synthesis from amorphous aluminosilicate gels [6, 28]. The products crystals are in fact smaller (~0.7 μm crystals, Figure 5.2c) than the S_1 seed crystals (~6 μm crystals, Figure 5.2a), making epitaxial growth [6, 28] of MFI crystals onto seeds implausible.

FAU diffraction lines disappeared after synthesis times of 4 h, whereas MFI lines were detectable at all times (4-40 h; Figure 5.3a-f) in transformations of FAU using MFI seeds (S_1). The amorphous background in the diffractograms (Figure 5.3; 2θ = 20-30°) disappeared and the MFI diffraction lines became the only discernible features after 24 h. These data indicate that FAU crystals lose their long-range order in NaOH media within a time scale that still preserves the identity of MFI seeds, which provide essential components for the ultimate recrystallization of FAU parent structures into MFI.

The size and shape of MFI crystals formed from seed-assisted FAU conversion to MFI did not change significantly during synthesis (4-40 h; TEM; Figure 5.4b-f) and resemble those of the parent FAU zeolite (TEM; Figure 5.4a). MFI mean crystal sizes are only slightly larger than those in the FAU parent zeolites (crystal size histograms; Figure 5.5). These findings would be consistent with a seed-assisted growth mechanism in which FAU structures loosen to form structures without local order and spalled MFI fragments from MFI seeds induce the nucleation of MFI frameworks at their outer surfaces, thus fixing an outer crust that allow it to preserve the habit and size of the parent crystals (Scheme 5.2). Such volume-conserving (pseudomorphic) transformations reflect the exclusive contact of seed fragments with the outer surface of locally disrupted, but otherwise intact, FAU domains, which nucleate MFI from the outer to the inner regions of these FAU domains.

The pseudomorphic nature of these processes requires the nucleation of voids in order to account for higher framework density of MFI relative to FAU. Such voids are evident in the TEM images of the product crystals (Figure 5.4b–f). The mechanistic hypothesis depicted in Scheme 5.2 would suggest that successful transformations require the synchronization of the local disruption of the FAU structure and the shedding of nucleating fragments from the MFI seeds. The requirement for high-silica FAU parent zeolites to form high-silica MFI products further implicates such synchronization because the lower solubility of higher Al-content FAU structures

may preclude local disruptions before the complete dissolution and loss of the local structures and CBU moieties of the MFI seeds (Si/Al ~ 300). The full dissolution of either FAU or MFI before interactions between seed fragments and locally disrupted FAU domains would prevent these seed-assisted pseudomorphic transformations.

The crystallinity of the MFI products calculated from the resulting diffractograms (with MgO as an internal standard) was 98%. The micropore volume from nitrogen adsorption data was 0.116 cm^3/g for MFI products (from MFI seeds (S_2)), similar to the pore volume of MFI seeds S_2 (0.12 cm^3/g) measured by the same method. Ar adsorption–desorption measurements on MFI crystals from seed-assisted transformations of FAU (using MFI seeds (S_1)) show hysteresis behavior at P/P_o (P_o is the saturation pressure at 87 K) values of ~0.4 (Figure 5.6), indicative of capillary condensation within mesopores [37, 38]; such behavior is not observed for MFI seed materials prepared by hydrothermal synthesis using structure-directing agents (TPABr; Section 5.2.2.1). Thus, we conclude that seed-assisted FAU to MFI transformations lead to the formation of mesopores directly during MFI crystallization, without requiring post-synthesis desilication [37]. Such mesopores are useful in practice because they decrease the diffusion distances prevalent for intact crystals; they also provide compelling evidence for the pseudomorphic (space-conserving) nature of seed-assisted interzeolite transformations.

We conclude that FAU-derived species retain their physical integrity, but as quasi-amorphous domains, and that incipient nucleation occurs at the outer regions of such domains by spalled subunits or CBU species derived from MFI seeds, which retain the local MFI structure required to assist the transformation of FAU-derived domains into MFI crystals. The space-conserving nature of the transformation requires, in turn, the nucleation of mesoscopic voids within the formed MFI crystals because their framework density is higher than that of the parent FAU. Any premature full dissolution of either seeds or parent zeolite into amorphous silica–alumina gels would prevent such seed-assisted interzeolite transformations, as we show in the next section, in which we propose a set of specific guidelines for successful transformations based on these mechanistic insights and on the observed spontaneous BEA conversion into MFI. Then, we assess the validity and usefulness of these guidelines by carrying out the synthesis of high-silica CHA, STF, and MTW zeolites via transformations of FAU and by varying the relevant synthesis conditions so as to achieve the intended transformations.

5.3.3 Requirements for Successful Zeolite Interconversions

The findings and mechanistic inferences described thus far have suggested that successful interzeolite transformations require (i) favorable thermodynamics- a parent zeolite of lower framework density than the target structure; (ii) a kinetic route to the target structure- nucleation assisted by either a common CBU between parent and target zeolites or seeds of the target zeolite; (iii) synthesis conditions that favor the target structure, instead of alternate structures, when common CBU are used to assist the transformation; (iv) high Si/Al parent zeolites when high-silica target structures are sought to allow complete conversion of locally amorphous parent domains; (v) synchronization of the spalling of the fragments or CBU moieties from seeds and the swelling and local restructuring of parent zeolite domains; (vi) $NaOH/SiO_2$ and Si/Al ratios that balance solubilization of seeds and parent zeolites so as to enforce synchronization in (v); and (vii)

chemical composition of the gel and synthesis conditions conducive to the formation of only the desired target structure in highly crystalline form.

FAU to MFI transformations were attempted for a range of $NaOH/SiO_2$ ratios (0.23 and 0.85 compared to 0.50 in Section 5.3.2) to probe the effects of synchronization or lack thereof between the local restructurings of the parent and seed zeolites. Diffractograms showed that $NaOH/SiO_2$ ratios of 0.23 led to essentially amorphous solids with only trace amounts of MFI crystals. In contrast, $NaOH/SiO_2$ ratios of 0.50 (Section 5.3.2) and 0.85 gave highly crystalline solids (98 and 100%, respectively). The lower solid yields achieved at higher $NaOH/SiO_2$ ratios (from 47 to 18% for $NaOH/SiO_2$ ratios of 0.50 and 0.85, respectively; Table 5.1), and the concomitant lower Si/Al ratios in MFI products (from 22 to 11; Table 5.1) indicate that a substantial fraction of SiO_2 in the parent FAU and the MFI seeds dissolved at the high final pH (12.0, Table 5.1) prevalent in synthesis protocols at the highest $NaOH/SiO_2$ ratio (0.85; Table 5.1). Such findings are consistent with the premature dissolution of one or both precursors before seed-derived MFI fragments contact locally disrupted FAU structures in the parent zeolite crystals.

Next, we explore the extension of these mechanism-based guidelines to the synthesis of high-silica CHA (FD 15.1), STF (FD 16.9), and MTW (FD 18.2) zeolites via interzeolite transformations of FAU (FD 13.3) and the synthesis conditions required for the effective synchronization required for successful transformations.

5.3.3.1 Synthesis of CHA via Transformations of FAU

CHA (FD 15.1) has a denser framework structure than FAU (FD 13.3) and contains a common*d6r* CBU; thus, we surmise that their interconversion can proceed without the assistance of seeds. As a result, we have attempted to form high-silica crystalline CHA from transformations of FAU under the same synthesis conditions as those used in transformations of FAU to MFI.

FAU (Si/Al = 40) formed only amorphous solids in the absence of seeds (0.5 NaOH: 1.0 SiO_2: 0.0125 Al_2O_3: 95 H_2O; Table 5.1), as shown in Figure 5.1, indicating that these synthesis conditions are not conducive to CHA formation. Thus, the synthesis condition was changed to that used previously [17] for synthesis of CHA from amorphous aluminosilicate gel, although without the use of an organic structure-directing agent. Crystalline CHA products with high Al content (Si/Al ~ 2.5) were obtained (X-ray diffraction patterns; Figure 5.S1) by transformations of high Al FAU (Si/Al = 2.5) in aqueous KOH under these conditions (KOH/SiO_2 = 0.54, H_2O/SiO_2 = 20, 403 K). The use of NaOH or of high-silica FAU, however, did not lead to the spontaneous formation of CHA (X-ray diffraction patterns; Figure 5.S1), suggesting that both K^+ and high Al FAU are required for spontaneous transformations of FAU into CHA and that there are significant kinetic barriers that prevent the formation of Na-CHA or high-silica CHA in the absence of seeds or OSDA species.

The use of CHA seeds with FAU parent zeolites with low Al contents may, however, circumvent the difficult nucleation suggested by the formation of amorphous structures in the presence of only common CBU species. Challenges may persist, though, as seed-assisted strategies require synchronization between the spalling of small structures or CBU species from CHA seeds and the local disruption of the FAU parent crystals. The addition of 10 wt % CHA seeds (0.5

NaOH: 1.0 SiO_2: 0.0125 Al_2O_3: 95 H_2O; Table 5.2) to FAU (Si/Al = 40) led to the formation of crystalline CHA zeolite (Si/Al = 19) after 40 h at 423 K (Figure 5.7) under conditions similar to those used for seed-assisted synthesis of MFI from FAU. The yield of solids (46%; Table 5.2) was similar to that measured for direct BEA to MFI conversion or seed-assisted FAU to MFI conversion (46–47%; Table 5.1). These similar yields reflect the solution equilibrium [39] under the synthesis conditions, which dissolves excess Si species, and result in similar yields (~47%) in all cases. The solids formed contain some amorphous materials, as shown by the broad background in their diffractograms (2θ = 20–30°; Figure 5.7), in contrast with the absence of substantial amorphous solids in the MFI products formed from BEA or FAU parent zeolites.

Higher $NaOH/SiO_2$ ratios (0.68 vs 0.50; Figure 5.7) led to CHA products with higher crystallinity (66 vs 50%; Table 5.2), possibly because the concomitantly higher pH favors faster disruptions of both CHA seeds and FAU parent crystals (without resulting in a full dissolution of FAU or of CHA seeds), leading to more effective synchronization. The solids yield and Si/Al ratio of the products formed (Table 5.2), in turn, decreased from 46 to 25% and 19 to 11, respectively, when $NaOH/SiO_2$ ratios increased from 0.50 to 0.68 because of the higher amounts of SiO_2 species dissolved in the liquid phase at the higher pH in the silica-rich synthesis gel. In contrast, amorphous aluminosilicate gels under similar synthesis conditions (0.68 NaOH: 1.0 SiO_2: 0.0125 Al_2O_3: 95 H_2O) with 10 wt % CHA seeds led to a mixture of CHA and MOR zeolites as products with only 6% yield (Figure 5.S2), confirming that the parent FAU zeolites in these interzeolite transformations do not dissolve completely and form amorphous aluminosilicate species.

CHA products were 66% crystalline, measured by powder XRD using MgO as an internal standard (Table 5.2); yet, the micropore volume, obtained from N_2 adsorption measurements, of these CHA products was 0.094 cm^3/g (per g of total solids), which is smaller than the theoretical void space of CHA (0.242 cm^3/g [36]), consistent with the presence of some amorphous solids in the final material but inconsistent with the crystallinity measurements from XRD. The H-CHA sample, synthesized by ammonium ion exchange of Na-CHA sample followed by thermal treatment in air to remove NH_3 (Section 5.2.2.3), showed no significant differences in the amount of nitrogen adsorbed (micropore volume 0.095 cm^3/g, Table 5.S1) compared to that of Na-CHA, suggesting that the pore blocking is not caused by localization of alkali cations at the pore entrances but perhaps by the presence of amorphous solids that can lead to a narrowing of pore openings or extra framework debris that can cause pore filling.

Formation of amorphous solids may reflect the imperfect synchronization of the local disruption of the FAU crystals and the disintegration of CHA seeds into nucleating moieties, a likely consequence of the higher Al content (and lower solubility) of CHA seeds (Si/Al = 15) compared with those in the FAU parent zeolite (Si/Al = 40) and the seeds used in MFI synthesis (Si/Al ~ 300) from FAU; the higher Al content in CHA seeds could delay the spalling of nucleation centers to a point after the parent FAU crystals lose their structural integrity. Thus, higher $NaOH/SiO_2$ ratios, which increase the solubility of CHA seeds without dissolving the parent FAU completely, may achieve more effective synchronization. A further increase in $NaOH/SiO_2$ ratio (to 0.85) leads to the formation of mixtures of CHA and MOR phases (Figure 5.7), indicating that high synthesis pH values lead to faster incipient nucleation of several frameworks as a result of the premature dissolution of parent or seed materials and rapid growth, thus making such high pH conditions inappropriate for the selective synthesis of a single zeolite framework. Thus, the

synthesis of high-silica CHA (Si/Al = 11) was achieved from transformations of FAU with CHA seeds using the developed synthesis guidelines; further investigations are needed, however, to understand the low micropore volume from nitrogen adsorption measurements in the final CHA products leading to the blocking of some pores. Next, we discuss the synthesis of high-silica STF and MTW zeolites via transformations of FAU based on the proposed synthesis guidelines for the success of these transformations.

5.3.3.2 Synthesis of STF via Transformations of FAU

STF structures are denser than FAU and thus thermodynamically favored, but these two frameworks do not share a common CBU, suggesting that FAU transformations into STF would require the assistance of STF seeds.

FAU (Si/Al = 40) formed only amorphous solids in the absence of any seeds under the synthesis conditions used (0.5 NaOH: 1.0 SiO_2: 0.0125 Al_2O_3: 95 H_2O; Table 5.1), as shown in Figure 5.1. STF zeolites, however, formed in synthesis mixtures containing parent FAU zeolite (Si/Al = 40) and 10 wt % STF seeds (Si/Al = 20) after 40 h at 423 K, conditions similar to those used for FAU to MFI transformations (0.5 NaOH: 1.0 SiO_2: 0.0125 Al_2O_3: 95 H_2O; Table 5.2), but the solids formed were of lower crystallinity than in the case of MFI (Figure 5.8 and Table 5.2). Higher $NaOH/SiO_2$ ratios (0.68 and 0.85 vs 0.50) led to more crystalline STF solids, similar to the pH effects observed in seed-assisted CHA synthesis from FAU (Figure 5.7). At the 0.68 $NaOH/SiO_2$ ratio, high-silica STF (Si/Al = 11) formed (Figure 5.9a) with solid yields of 26% (Table 5.2), similar to those measured in seed-assisted FAU conversion to CHA (Si/Al = 11, 25% yield, Table 5.2). The STF product was 78% crystalline, measured by powder XRD using MgO as an internal standard (Table 5.2); yet, its micropore volume (from N_2 adsorption) was 0.027 cm^3/g (Table 5.S1), a value much smaller than the theoretical value for STF structure (0.20 cm^3/g [36]). Possible reasons for the low micropore volumes and efforts to increase the pore volume of the STF sample are discussed in the next section.

Higher temperatures (428 K) in seed-assisted FAU conversions to STF did not cause detectable changes in the intensity of STF diffraction lines (Figure 5.8) or in the product yield or Si/Al ratio (Table 5.2). Further increase in the temperature (433 K) led to the formation of the denser MFI structures instead of STF (Figure 5.8), suggesting that STF crystals derived from FAU with the assistance of seeds are metastable and form MFI by overcoming kinetic hurdles to form denser structures at higher temperatures. STF and MFI zeolites share the *cas* structural motif, suggesting that *cas* moieties in STF seeds or in STF crystals formed from FAU can also assist MFI nucleation from parent FAU crystals at these higher temperatures.

The synthesis of high-silica STF (Si/Al = 11) was achieved from transformations of FAU using STF seeds; the STF products showed micropore volume lower than that expected from the STF crystal structure and the XRD crystallinity data; we explore plausible causes and potential solutions for this low micropore volume accessibility in STF products in the next section. First, we discuss the synthesis of high-silica MTW zeolites via transformations of FAU.

5.3.3.3 Synthesis of MTW via Transformations of FAU

MTW structures are also denser than FAU and thus thermodynamically favored, but they do not share a common CBU with FAU; thus, we expect that FAU conversion to MTW will require the presence of MTW seeds in the synthesis mixture. Indeed, FAU (Si/Al = 40) formed only amorphous solids in the absence of any seeds under the synthesis conditions used (0.5 NaOH: 1.0 SiO_2: 0.0125 Al_2O_3: 95 H_2O; Table 5.1), as shown previously in Figure 5.1. MTW zeolites formed in synthesis mixtures containing parent FAU zeolites (Si/Al = 40) and 10 wt % MTW (Si/Al = 30) seeds after 40 h at 423 K under conditions similar to those used for FAU to MFI, CHA, and STF transformations (0.5 NaOH: 1.0 SiO_2: 0.0125 Al_2O_3: 95 H_2O; Table 5.2), but the solids formed had significant amorphous phase present, similar to that for STF and CHA syntheses. High-silica MTW (Si/Al = 12) formed, from transformation of FAU using MTW seeds, with solid yield of 29% (Table 5.2) at a $NaOH/SiO_2$ ratio of 0.68 (Figure 5.9), similar to those measured for seed-assisted FAU conversion to CHA (Si/Al = 11, 25% yield, Table 5.2) and STF (Si/Al = 11, 26% yield, Table 5.2). This MTW product was 60% crystalline (Table 5.2), measured by powder XRD using MgO as an internal standard, but the micropore volume (from N_2 adsorption) was 0.006 cm^3/g (Table 5.S1), much smaller than the theoretical value for MTW structure (0.11 cm^3/g [36]) and inconsistent with the relatively higher crystallinity value obtained from XRD measurements.

The small values of accessible micropore volumes (Table 5.S1) in the STF and MTW zeolites formed via seed-assisted synthesis from FAU are not consistent with their crystalline nature and may reflect ubiquitous channel blockages that have been reported for one-dimensional zeolites, such as STF and MTW. Previous studies on MOR zeolites [40, 41] have concluded that such blockages account for the inability of MOR structures (with 0.65 × 0.70 nm channels along the [001] direction and 0.57 × 0.26 nm along the [011] direction) to adsorb molecules with kinetic diameters larger than ~0.4 nm [40]; such blockages have been attributed to intrachannel amorphous debris and to cations or defects along the main channels in MOR. These factors may also account for the low accessible micropore volumes reported here for STF and MTW zeolites.

H-STF and H-MTW samples, prepared by exchanging the seed-assisted Na-STF and Na-MTW samples with NH_4^+ cations and treatment in air at 873 K (Section 5.2.2.3), did not lead to higher N_2 uptake than that of the Na-containing samples (micropore volumes; Table 5.S1). We conclude that any channel blockages are not caused by Na cations but may reflect instead the presence of amorphous intrachannel debris or structural defects that may form within the one-dimensional channels during crystal growth. The extensive twinning and faulting in MTW frameworks, caused by the incoherent stacking of polymorphs, have been reported in MTW prepared via OSDA-assisted [42] and OSDA-free [15] protocols from amorphous aluminosilicate gels. Stacking faults may also form during synthesis without OSDA, but such effects cannot be detected via powder XRD due to their local nature and their small number. Further studies are currently underway using magic angle spinning (MAS) NMR and high-resolution electron microscopy (HREM) to better understand the reduced micropore volume behavior of these materials.

The metastable nature of seed-mediated synthesis products (toward conversion to denser structures) was confirmed by examining the evolution of various crystalline structures with increasing synthesis time. Products from transformations of FAU using MFI, CHA, STF, or MTW

seeds converted to denser structures as time proceeded and led to mixtures of dense zeolite phases after 10 days of synthesis (X-ray diffraction patterns; Figure 5.S3).

Next, we test one of the proposed guidelines for the kinetic route to the target zeolite: nucleation assisted by either a common CBU between parent and product zeolites or seeds of the desired zeolite help to overcome the kinetic barriers during transformations by probing the conversion of FAU and BEA zeolite mixture into the product MFI, where BEA can either generate the *mor* CBU common with MFI or directly transform to MFI seeds (as described in Section 5.3.1), which can promote the transformation of FAU.

5.3.3.4 Synthesis of MFI via Transformations of FAU and BEA Zeolite Mixtures

BEA converts to MFI in the absence of MFI seeds or OSDA, but either seeds or OSDA are required to successfully form MFI from FAU, apparently because of their lack of a common CBU. The presence of small amounts of BEA in a mixture with the parent FAU zeolite may allow the in situ formation of either MFI seed crystals or *mor* structural units (from BEA).

Indeed, MFI formed from FAU–BEA mixtures (50-50 wt %) regardless of whether MFI seeds were present (10 wt %; Figure 5.10a) or not (Figure 5.10b) ($NaOH/SiO_2$ = 0.45, H_2O/SiO_2 = 80). MFI structures formed even for 5 or 10 wt % BEA in such mixtures (Figure 5.10c,d). MFI product yields (46-48%) were similar to those observed in spontaneous BEA to MFI transformation and seed-assisted FAU to MFI interconversions (46-47%, Table 5.1). These data show that BEA assists the nucleation of MFI structures from FAU, through its ability to lower kinetic barriers in FAU to MFI transformations by providing either *mor* structural units (common to MFI) or MFI seed crystals. In this manner, the on-purpose synthesis and addition of seeds of the target structure (or OSDA requirements) are avoided, in general, by exploiting a spontaneous transformation of a minority component of a zeolite with a common CBU with the target zeolite to effect the conversion of a parent zeolite that lacks a common CBU with the target framework structure. This general strategy is consistent with the guidelines developed in the previous sections and shows that target seeds and/or common CBU can be formed in situ, thus avoiding the specific addition of target seeds to parent zeolites that require kinetic assistance because of the lack of a common CBU with target structures.

These data, together with the effect of synthesis temperature, confirm that products of the interzeolite transformations are metastable structures for a certain set of synthesis conditions; these structures, with time or temperature, will convert to thermodynamically more stable structures (dense phases). These transformations, taken together, provide evidence for the key role of the Si/Al ratio of the parent zeolite in determining their ability to restructure and form high-silica zeolites, of NaOH to SiO_2 ratios of the synthesis gel to ensure the synchronized decomposition of the parent and the seed structures, and of temperature and time to form metastable desired structures. The successful synthesis of high-silica CHA, STF, and MTW zeolites supports the validity of the synthesis guidelines; further investigations for pore unblocking are, however, required to form accessible highly crystalline products. We expect that the interzeolite transformation protocols developed here for the synthesis of high-silica zeolites can be extended further to zeolites of different frameworks, void environments, and framework compositions, based on their framework density and CBU components. These methods not only synthesize

zeolites without OSDA but also form mesoporous crystals, which are known to improve the accessibility of reactant molecules to the zeolite micropores [41] in chemical reactions catalyzed within such micropores and thus have the potential to enhance the turnover rates and tune the selectivity to desired products.

5.4 Conclusion

We have demonstrated a general strategy and a set of guiding rules for the synthesis of microporous solids without the use of organic structure-directing agents (OSDA) via interzeolite transformation protocols. Parent structures with lower framework densities (FAU or BEA) were successfully transformed into thermodynamically favored more stable structures with higher framework densities (MFI, CHA, STF, and MTW) via recrystallization in aqueous NaOH under hydrothermal conditions. Successful transformations required that we overcome kinetic hurdles while exploiting the thermodynamic tendency of microporous solids to increase their framework density. Transformation of BEA to MFI occurred spontaneously without any significant kinetic and thermodynamic hurdles, whereas the conversion of FAU to MFI, CHA, STF, and MTW required the product seeds, suggesting the absence of sufficient kinetic driving forces in these cases. A plausible synthesis mechanism, pseudomorphic in nature (transformations that conserve the volume occupied by the parent crystals, leading to similar size and crystal shape in products), for seed-assisted transformations is consistent with the observed effects of the parent Si/Al ratio, the $NaOH/SiO_2$ ratio, and the required synthesis temperature and time, as well as with the crystal habit and intracrystal mesoporous voids in the product crystals. Such phenomena reflect incipient nucleation of new structures occurring at the outer regions of the parent crystals and leading to the formation of mesoporosity during such transformations as a natural consequence of the space-conserving nature of the structural changes and of the higher density of the daughter frameworks. Specific guidelines for successful transformations are inferred from the mechanistic insights of seed-assisted FAU to MFI transformation and from the spontaneous BEA conversion into MFI. The findings and mechanistic inferences suggest that successful interzeolite transformations require (i) favorable thermodynamics- a parent zeolite of lower framework density than the target structure; (ii) a kinetic route to the target structure- nucleation assisted by either a common CBU between parent and target zeolites or seeds of the target zeolite; and (iii) chemical composition of gel and synthesis conditions conducive to the formation of only the desired target structure, instead of alternate structures, in highly crystalline form. The synthesis mechanism and the guidelines developed here enable us to design the synthesis conditions required for desired zeolites, which previously required OSDA for the synthesis, and will expand the diversity of framework types of zeolites that can be synthesized via these methods.

5.5 Acknowledgments

We thank Reena Zalpuri (Electron Microscope Lab) for help with the TEM instrument, Dr. Prashant Deshlahra, Stanley Herrmann, Edwin Yik, and Dr. Xueyi Zhang for the careful review of this writing, and Chevron Energy Technology Company for the financial support for this research.

5.6 Figures, Tables and Schemes

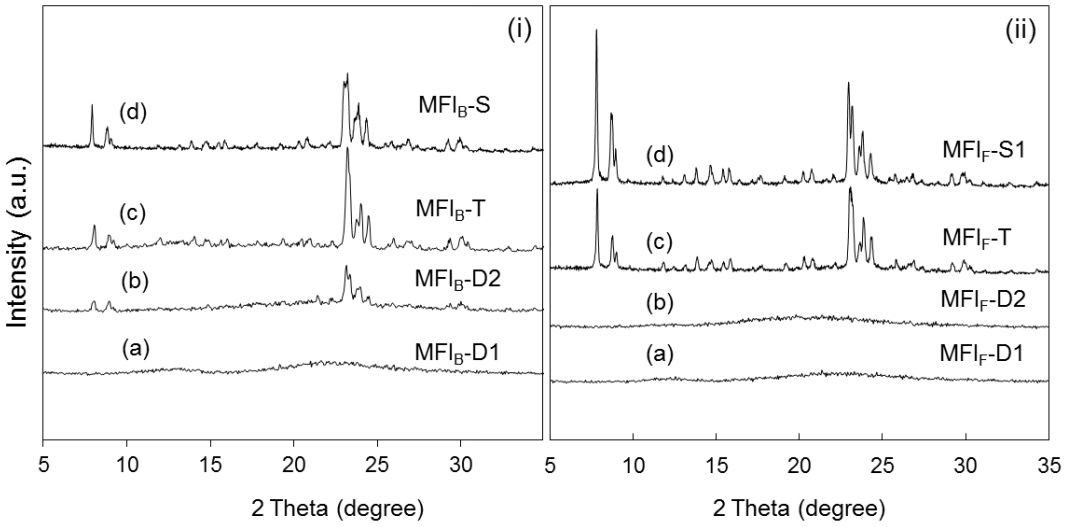

Figure 5.1 X-ray diffractograms of the products synthesized from parent (i) BEA and (ii) FAU via (a, b) direct, (c) template-assisted and (d) seed-assisted (using MFI seeds (S_1)) transformations. Syntheses were carried out at 423 K, $NaOH/SiO_2$ = 0.35 (from BEA) and 0.50 (from FAU) and H_2O/SiO_2 = 65 (from BEA) and 95 (from FAU) (Table 5.1).

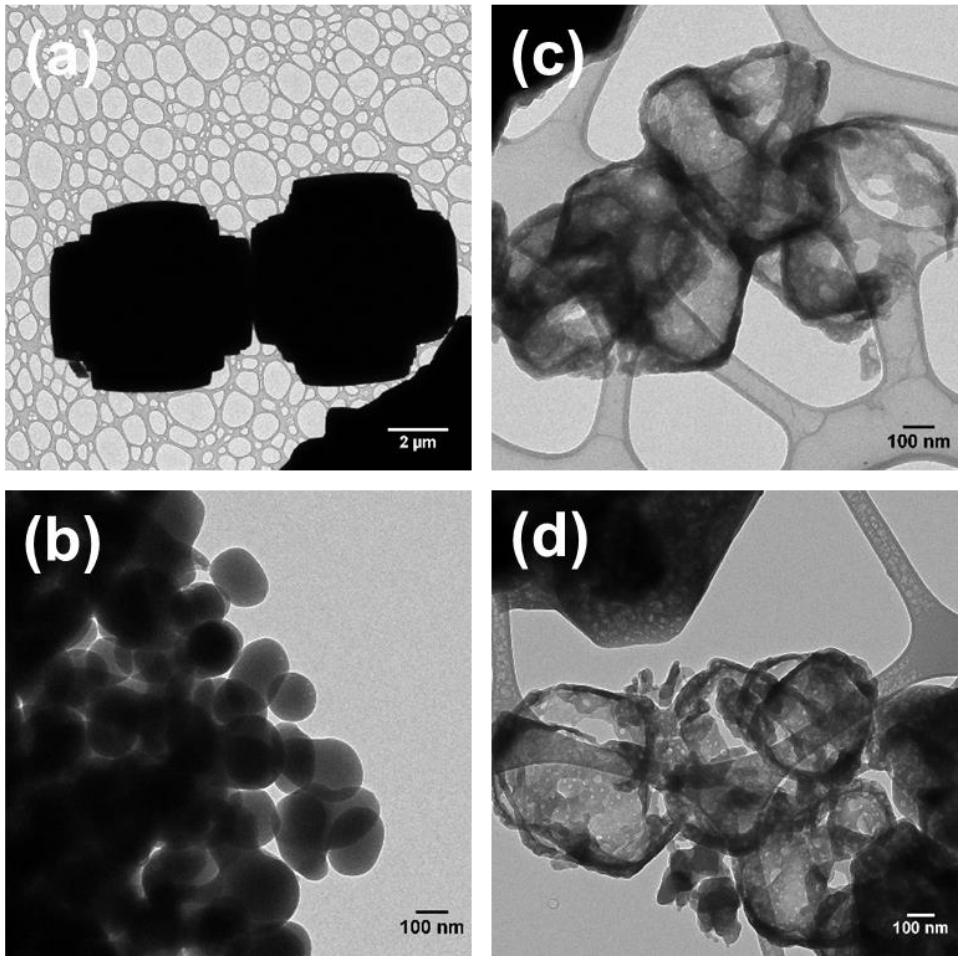

Figure 5.2 TEM images of MFI seeds (a) S_1 (~ 6 µm) and (b) S_2 (~ 0.2 µm) and products synthesized via transformations of parent FAU (Si/Al = 40) using (c) S_1 and (d) S_2 MFI seeds. The syntheses were carried out at 423 K, $NaOH/SiO_2 = 0.5$, $H_2O/SiO_2 = 95$ for 40 h with 10% wt. MFI seeds.

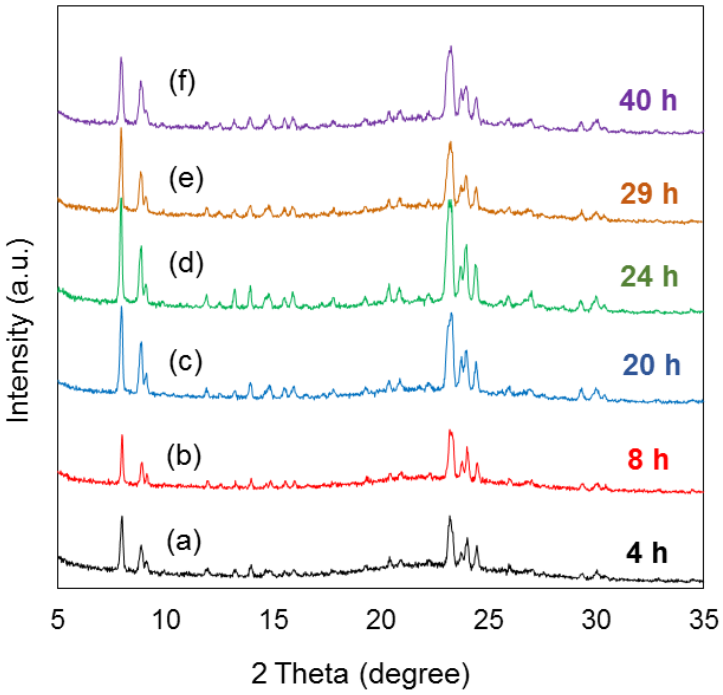

Figure 5.3 X-ray diffractograms of the products synthesized via seed-assisted transformations of parent FAU (Si/Al = 40) at synthesis times of (a) 4, (b) 8, (c) 20, (d) 24, (e) 29, and (f) 40 h. Syntheses were carried out at 423 K, $NaOH/SiO_2 = 0.5$, $H_2O/SiO_2 = 95$ with 10% wt. MFI seeds (S_1).

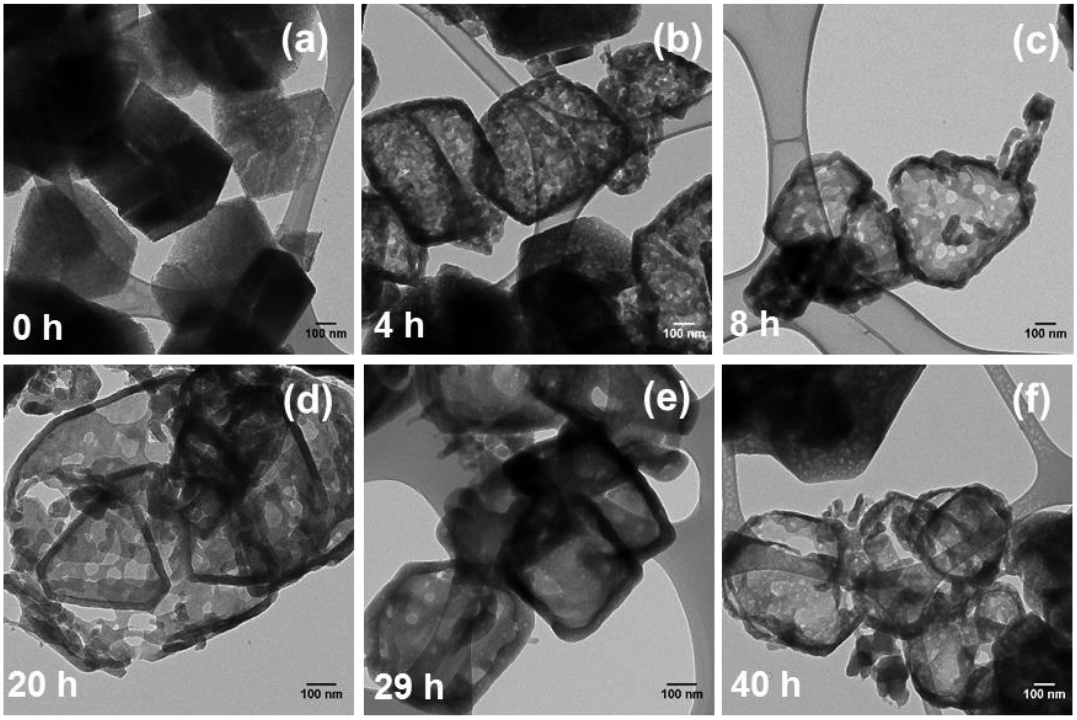

Figure 5.4 TEM images of the products synthesized via seed-assisted transformations of parent FAU (Si/Al = 40) at synthesis times of (a) 0 (parent FAU), (b) 4, (c) 8, (d) 20, (e) 29, and (f) 40 h. Syntheses were carried out at 423 K, $NaOH/SiO_2 = 0.5$, $H_2O/SiO_2 = 95$ with 10 % wt. MFI seeds (S_1).

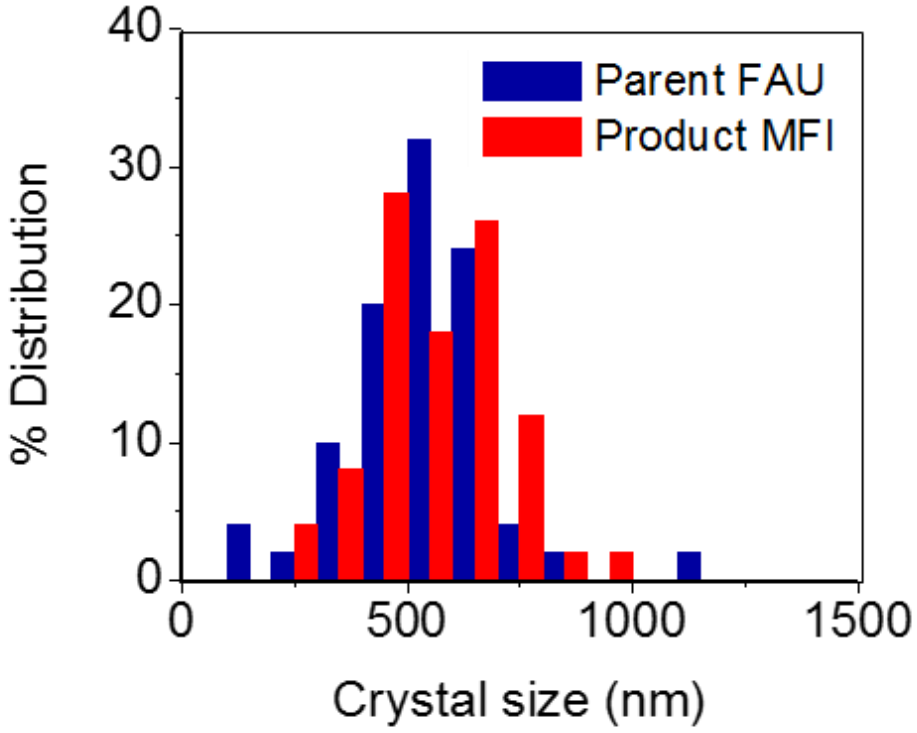

Figure 5.5 Crystal size distributions of parent FAU and product MFI zeolites (MFI_F-S1), synthesized via seed-assisted transformations of FAU (Si/Al = 40). The synthesis was carried out at 423 K, $NaOH/SiO_2$ = 0.5, H_2O/SiO_2 = 95 for 40 h with 10 % wt. MFI seeds (S_1).

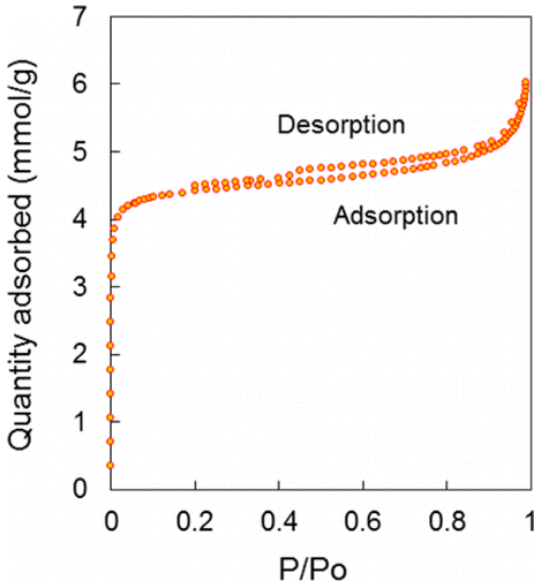

Figure 5.6 Ar adsorption and desorption isotherms for the product MFI zeolite (MFI_F-S1) synthesized via seed-assisted transformations of FAU (Si/Al =40). The synthesis was carried out at 423 K, $NaOH/SiO_2$=0.5, H_2O/SiO_2=95 for 40 h with 10% wt. MFI seeds (S_1).

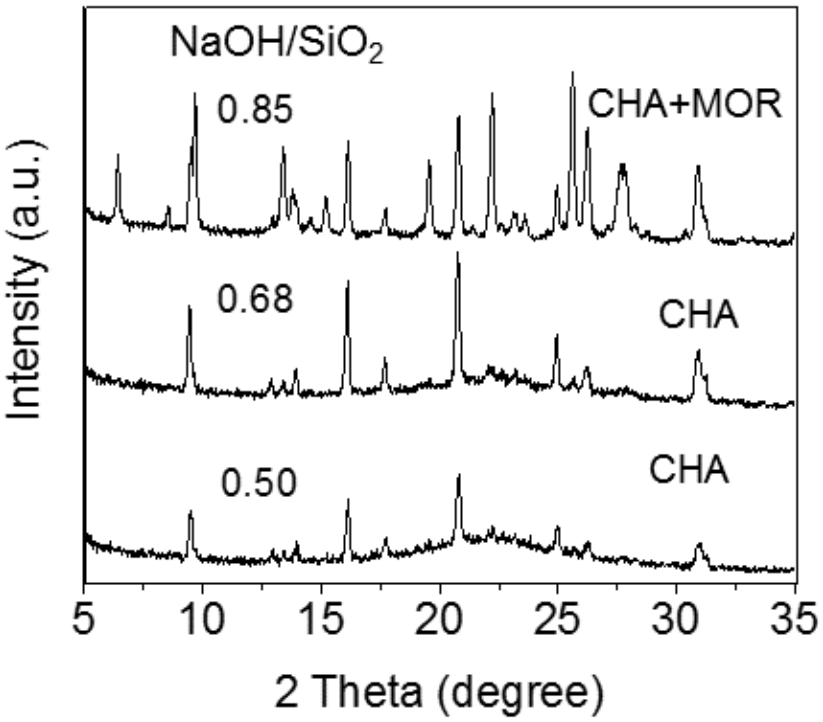

Figure 5.7 X-ray diffractograms of the products synthesized via transformations of FAU (Si/Al= 40) at $NaOH/SiO_2$ ratio of (a) 0.50, (b) 0.68, and (c) 0.85 using 10% wt. CHA seeds. Syntheses were carried out at 423 K, H_2O/SiO_2 = 95 for 40 h (Table 5.2).

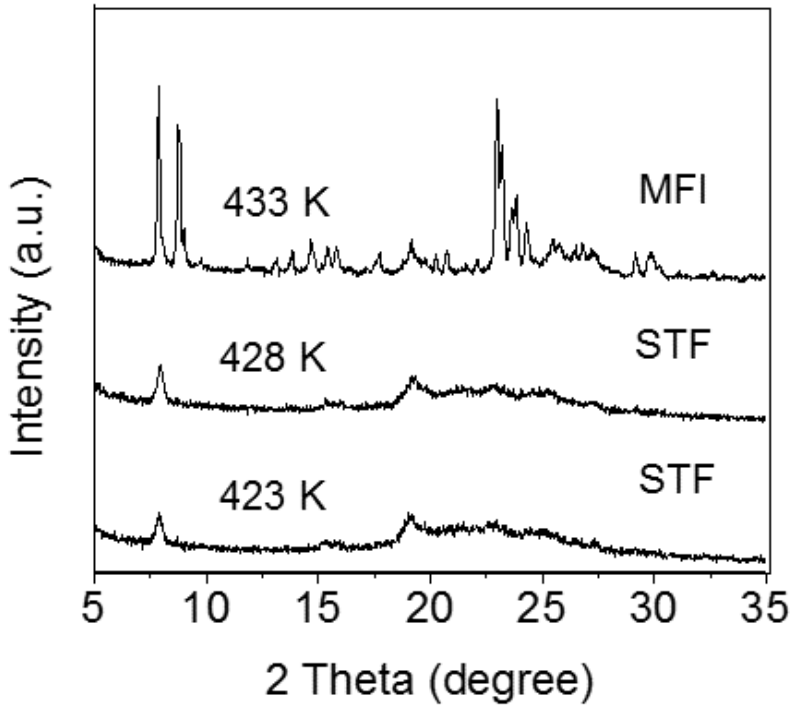

Figure 5.8 X-ray diffractograms of the products synthesized via transformations of parent FAU (Si/Al =40) at various temperatures in the presence of 10% wt. STF seeds. Syntheses were carried out for 40 h at $NaOH/SiO_2 = 0.5$, $H_2O/SiO_2 = 95$ (Table 5.2).

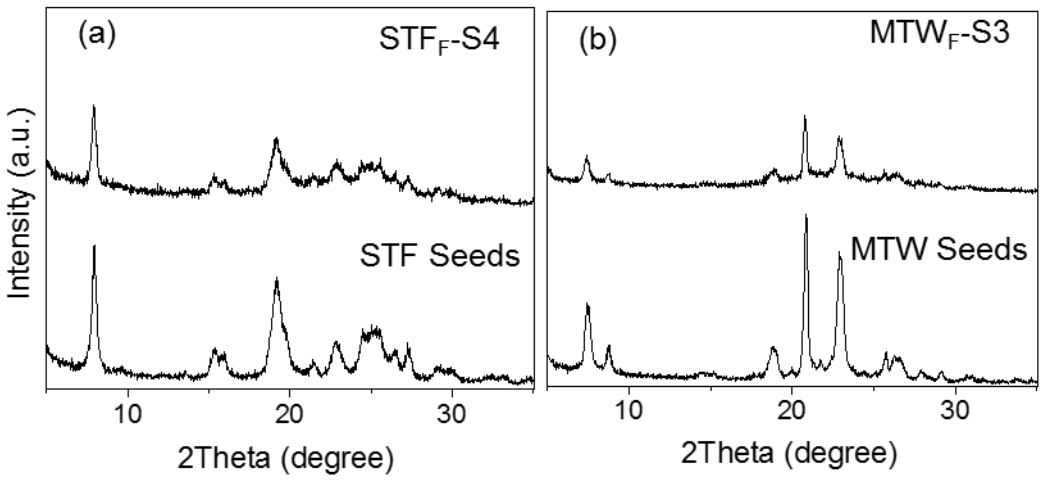

Figure 5.9 X-ray diffractograms of the products synthesized via transformations of parent FAU (Si/Al =40) with 10% wt. seeds of (a) STF and (b) MTW and their corresponding seeds used. Syntheses were carried out at 423 K, $NaOH/SiO_2 = 0.68$, $H_2O/SiO_2 = 95$ for 40 h (Table 5.2).

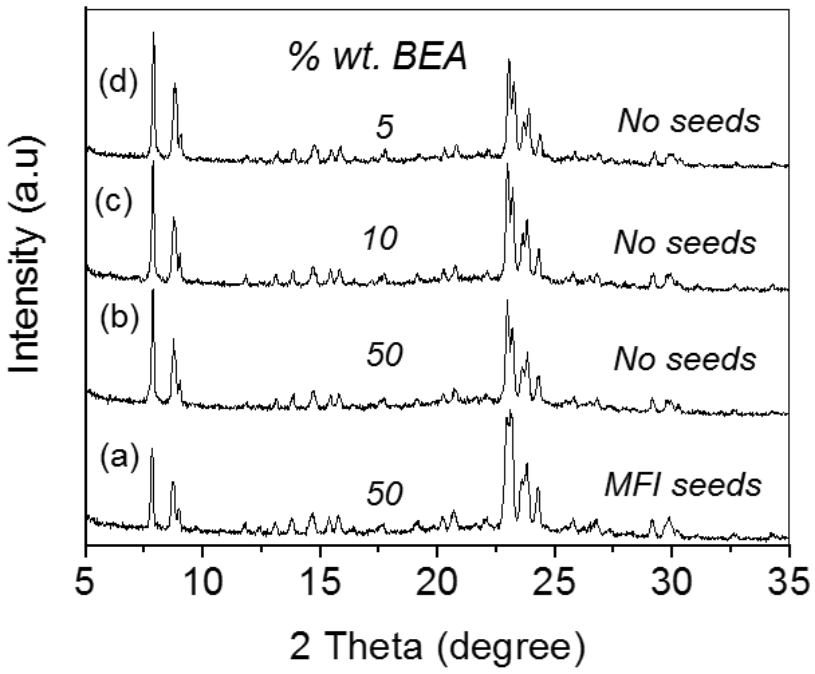

Figure 5.10 X-ray diffractograms of the products synthesized via transformations of FAU and BEA in (a) a mixture with 50% BEA and assisted by MFI seeds, and seed-free mixtures with (b) 50%, (c) 10%, and (d) 5% BEA. Syntheses were carried out at 423 K, $NaOH/SiO_2 = 0.45$, $H_2O/SiO_2 = 80$ and 40 h with/without 10% wt. MFI seeds (S_1).

Table 5.1 Initial synthesis molar compositions, product phase, yield and final pH of samples for synthesis of MFI.[a]

Sample name	Parent zeolite (Si/Al)	NaOH /SiO_2 [b]	H_2O/ SiO_2 [b]	Time (h)	Additional (OSDA/seed) [c]	Product phase[d]	Product (Si/Al)	Final pH	Yield[e] (%)
MFI_B-D1	BEA(12.5)	0.35	65	24	-	Am.	-	-	-
MFI_B-D2	BEA(37.5)	0.35	65	24	-	MFI	22	11.8	46
MFI_B-T	BEA(37.5)	0.35	65	24	TPABr (0.05)[f]	MFI	35	12.5	47
MFI_B-S	BEA(37.5)	0.35	65	24	10 wt % MFI Seeds	MFI	23	11.8	47
MFI_F-D1	FAU(6)	0.50	95	40	-	Am.	-	-	-
MFI_F-D2	FAU(40)	0.50	95	40	-	Am.	-	-	-
MFI_F-T	FAU(40)	0.50	95	40	TPABr (0.05)[f]	MFI	33	12.5	58
MFI_F-S1	FAU(40)	0.50	95	40	10 wt % MFI Seeds	MFI	22	11.8	47
MFI_F-S2	FAU(40)	0.23	95	40	10 wt % MFI Seeds	MFI+Am.	42	11.7	76
MFI_F-S3	FAU(40)	0.85	95	40	10 wt % MFI Seeds	MFI	11	12.0	18

[a] T = 423 K for all the syntheses.
[b] Reported values excludes the SiO_2 amount present in seed materials.
[c] $Seed\ (wt.\%) = \frac{Seed\ material\ (g)}{Parent\ zeolite\ (g)}\ x\ 100$
[d] Am. = Amorphous
[e] $yield\ (\%) = \frac{Product\ (g)}{Parent\ zeolite\ (g)+Seed\ (g)}\ x\ 100$
[f] Values in parentheses show molar composition of TPABr relative to SiO_2 amount of parent zeolite.

Table 5.2 Initial synthesis molar compositions, product phase, yield and final pH of samples for transformations of FAU using CHA, STF and MTW seeds.[a]

Sample Name	Parent (Si/Al)	NaOH/ SiO_2 [b]	Seeds [c] (10 wt %)	Temp (K)	Product phase [d]	Product (Si/Al)	Final pH	Yield[e] (%)	Crystallinity (%)
CHA_F-S1	FAU(40)	0.50	CHA	423	CHA+Am.	19	11.8	46	50
CHA_F-S2	FAU(40)	0.68	CHA	423	CHA+Am.	11	11.7	25	66
CHA_F-S3	FAU(40)	0.85	CHA	423	CHA+MOR	-	12.2	22	-
CHA_F-S4	FAU(40)	0.50	CHA	428	CHA+Am.	-	11.9	49	-
STF_F-S1	FAU(40)	0.50	STF	423	STF+Am.	-	11..8	47	-
STF_F-S2	FAU(40)	0.50	STF	428	STF+Am.	-	11.8	48	-
STF_F-S3	FAU(40)	0.50	STF	433	STF+MFI	-	12.0	52	-
STF_F-S4	FAU(40)	0.68	STF	423	STF+Am.	11	11.7	26	78
STF_F-S5	FAU(40)	0.85	STF	423	STF+MOR	-	12.0	33	-
MTW_F-S1	FAU(40)	0.50	MTW	423	MTW+Am.	-	11.9	44	-
MTW_F-S2	FAU(40)	0.50	MTW	428	MTW+Am.	-	11.8	48	-
MTW_F-S3	FAU(40)	0.68	MTW	423	MTW+Am.	12	12.0	29	60

[a] H_2O/SiO_2 = 95 and synthesis time = 40 h for all the syntheses.
[b] Reported values exclude the SiO_2 amount present in seed materials.
[c] $Seed\ (wt.\%) = \frac{Seed\ material\ (g)}{Parent\ zeolite\ (g)}\ x\ 100$
[d] Am. = Amorphous
[e] $yield\ (\%) = \frac{Product\ (g)}{Parent\ zeolite\ (g)+Seed\ (g)}\ x\ 100$

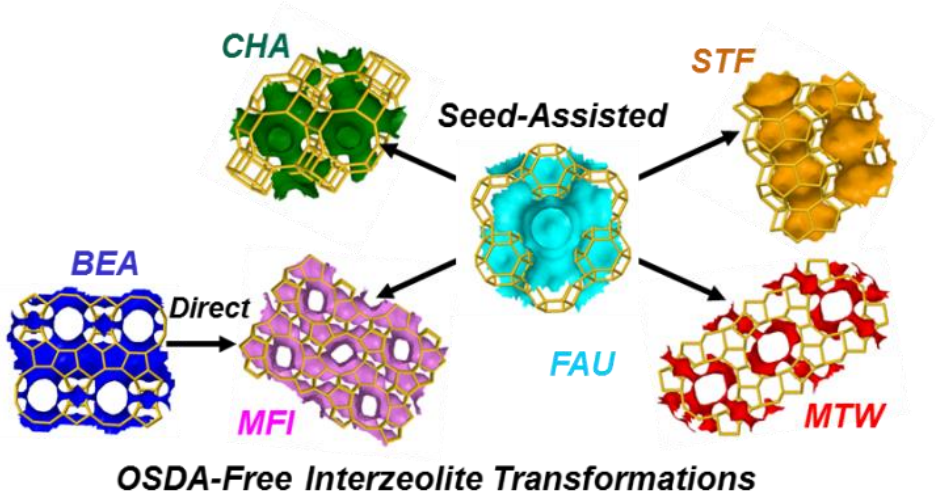

Scheme 5.1 Schematic representation of the synthesis of MFI, CHA, STF, and MTW zeolites via direct or seed-assisted transformations of parent BEA or FAU zeolites without organic structure-directing agents (OSDA).

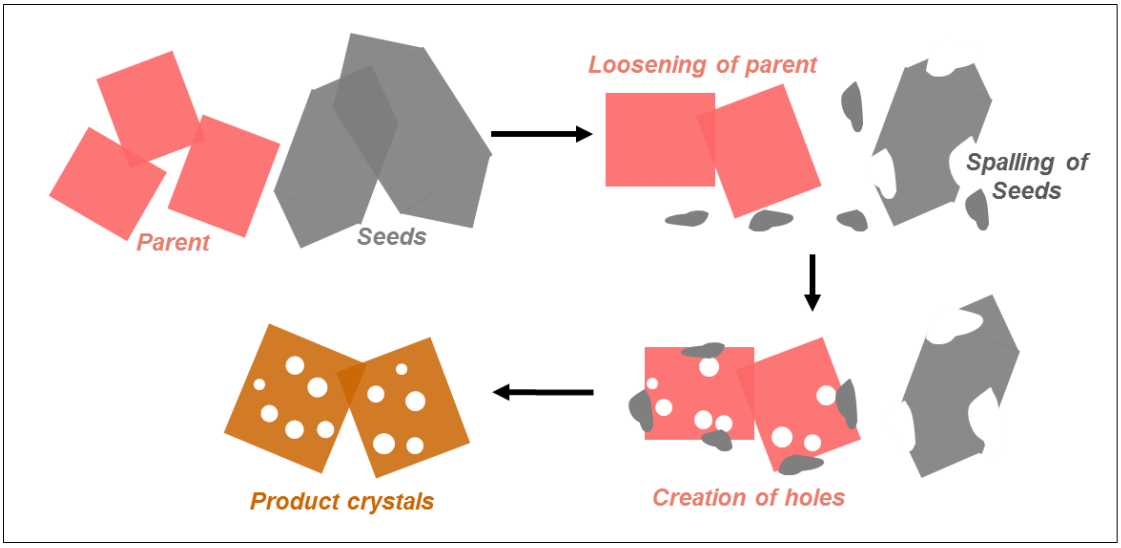

Scheme 5.2 Schematic representation of the proposed mechanism for seed-assisted transformations of parent FAU to daughter MFI zeolites.

5.7 Supporting Information

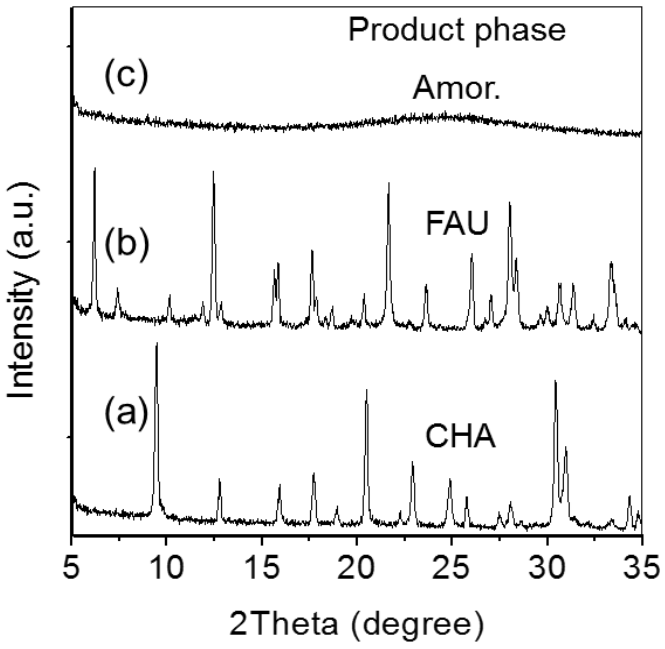

Figure 5.S1 X-ray diffractograms of the products synthesized by transformations using (a) FAU (Si/Al = 2.5) and KOH, (b) FAU (Si/Al = 2.5) and NaOH, and (c) FAU (Si/Al = 40) and NaOH. Syntheses were carried out at 403 K, XOH/SiO_2= 0.54 (X= Na, K), H_2O/SiO_2= 20 for 24 h.

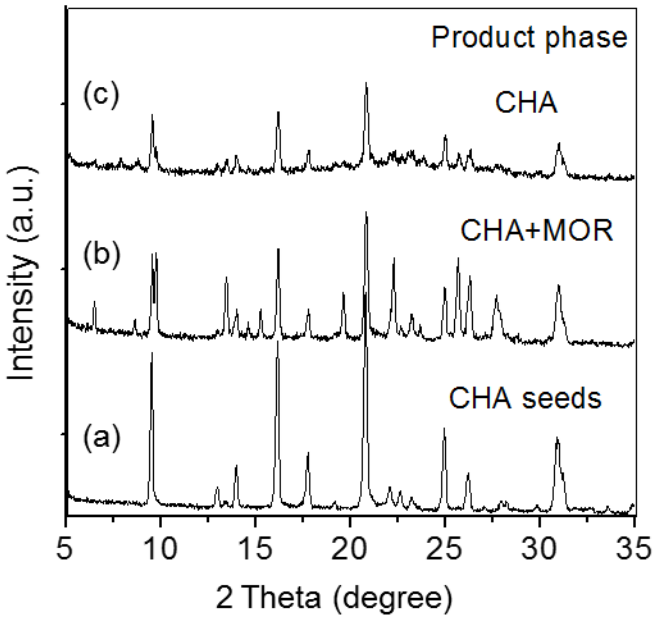

Figure 5.S2 X-ray diffractograms of (a) CHA seeds and the products synthesized with 10 wt % CHA seeds from (b) amorphous Si and Al sources and (c) parent FAU. Syntheses were carried out at 423 K, 0.68 NaOH: 1.0 SiO_2: 0.0125 Al_2O_3: 95.0 H_2O for 40 h. The solid yield of products was 6% in (b) and 25% in (c).

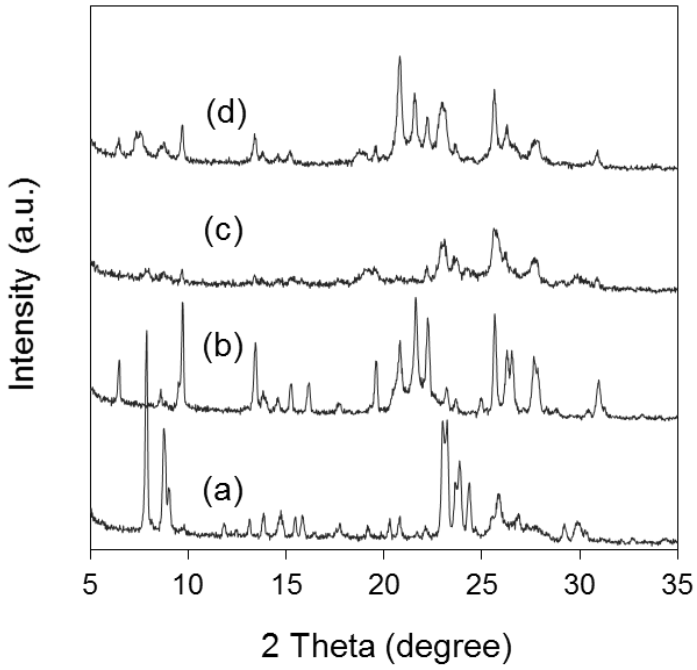

Figure 5.S3 X-ray diffractograms of the products synthesized via seed-assisted transformations of FAU (Si/Al = 40) using 10 wt % (a) MFI, (b) CHA, (c) STF and (d) MTW seeds for synthesis time of 10 days. Syntheses were carried out at 423 K, $NaOH/SiO_2$ = 0.5 (for MFI) and 0.68 (for CHA, STF, and MTW), and H_2O/SiO_2 = 95.

Table 5.S1 Micropore volumes of CHA, STF, and MTW samples synthesized via seed-assisted transformations of FAU.

Sample Name	Micropore volume[a] (cm^3/g)
Na-CHA	0.094
H-CHA[b, c]	0.095
CHA seeds	0.280
Na-STF	0.027
H-STF[b]	0.025
STF seeds	0.160
Na-MTW	0.006
H-MTW[b]	0.007

[a] Measured by N_2 adsorption at 77 K (ASAP 2020, Micromeritics). Prior to the measurements, both samples were degassed at 623 K for 4 h under vacuum. Micropore volumes are reported per g of total solids.
[b] H-Zeolite samples were synthesized by ammonium ion exchange of Na-Zeolite followed by thermal treatment in air to remove NH_3.
[c] 80% of total Na (determined by ICP-AES) present in the Na-CHA sample was successfully exchanged with NH_4^+ to form H-CHA sample.

5.8 References

(1) Davis, M. E. *Chem. Mater.* 2014, 26, 239.
(2) Weisz, P. B.; Frilette, V. J.; Maatman, R. W.; Mower, E. B. *J. Catal.* 1962, 1, 307.
(3) Csicsery, S. M. *Zeolites* 1984, 4, 202.
(4) Barrer, R. M. In *Zeolite Synthesis*; Occelli, M. L.; Robson, H. E., Eds.; American Chemical Society: Washington, DC, 1989; Vol. 398, pp 11.
(5) Corma, A.; Davis, M. E. *ChemPhysChem* 2004, 5, 304.
(6) Cundy, C. S.; Cox, P. A. *Microporous Mesoporous Mater.* 2005, 82, 1.
(7) Moliner, M.; Martínez, C.; Corma, A. *Chem. Mater.* 2014, 26, 246.
(8) Meng, X.; Xiao, F.-S. *Chem, Rev.* 2014, 114, 1521.
(9) Roth, W. J.; Nachtigall, P.; Morris, R. E.; Wheatley, P. S.; Seymour, V. R.; Ashbrook, S. E.; Chlubná, P.; Grajciar, L.; Položij, M.; Zukal, A.; Shvets, O.; Čejka, J. *Nat. Chem.* 2013, *5*, 628.
(10) Wheatley, P. S.; Chlubná-Eliášová, P.; Greer, H.; Zhou, W.; Seymour, V. R.; Dawson, D. M.; Ashbrook, S. E.; Pinar, A. B.; McCusker, L. B.; Opanasenko, M.; Čejka, J.; Morris, R. E. *Angew. Chem. Int. Ed.* 2014, *53*, 13210.
(11) Xie, B.; Zhang, H.; Yang, C.; Liu, S.; Ren, L.; Zhang, L.; Meng, X.; Yilmaz, B.; Müller, U.; Xiao, F.-S. *Chem. Commun.* 2011, 47, 3945.
(12) Itabashi, K.; Kamimura, Y.; Iyoki, K.; Shimojima, A.; Okubo, T. A *J. Am. Chem. Soc.* 2012, 134, 11542.
(13) Iyoki, K.; Itabashi, K.; Okubo, T. *Microporous Mesoporous Mater.* 2014, 189, 22.
(14) Iyoki, K.; Itabashi, K.; Chaikittisilp, W.; Elangovan, S. P.; Wakihara, T.; Kohara, S.; Okubo, T. *Chem. Mater.* 2014, 26, 1957.
(15) Kamimura, Y.; Iyoki, K.; Elangovan, S. P.; Itabashi, K.; Shimojima, A.; Okubo, T. *Microporous Mesoporous Mater.* 2012, 163, 282.
(16) Kamimura, Y.; Itabashi, K.; Okubo, T. *Microporous Mesoporous Mater.* 2012, 147, 149.
(17) Moden, B.; Cooper, D.; Li, H. X.; Cormier, W. E. *U.S. Patent* 0269719 A1, 2012.
(18) Zones, S. I. *J. Chem. Soc., Faraday Trans*. 1991, 87, 3709.
(19) Itakura, M.; Goto, I.; Takahashi, A.; Fujitani, T.; Ide, Y.; Sadakane, M.; Sano, T. *Microporous Mesoporous Mater.* 2011, 144, 91.
(20) Honda, K.; Itakura, M.; Matsuura, Y.; Onda, A.; Ide, Y.; Sadakane, M.; Sano, T. *J. nanosci. nanotechnol.* 2013, 13, 3020.
(21) Nedyalkova, R., Montreuil, C., Lambert, C. & Olsson, L. *Top. Catal.* 2013, 56, 550.
(22) Sano T., Itakura M., Sadakane M. *J. Jpn Pet. Inst.* 2013, 56, 183.
(23) Tendeloo, L. V.; Gobechiya, E.; Breynaert, E.; Martens, J. A.; Kirschhock, C. E. A. *Chem. Commun.* 2013, 49, 11737.
(24) Jon, H.; Ikawa, N.; Oumi, Y.; Sano, T. *Chem. Mater.* 2008, 20, 4135.
(25) Honda, K.; Yashiki, A.; Sadakane, M.; Sano, T. *Microporous Mesoporous Mater.* 2014, 196, 254.
(26) Dhainaut, J.; Daou, T. J.; Bidal, Y.; Bats, N.; Harbuzaru, B.; Lapisardi, G.; Chaumeil, H.; Defoin, A.; Rouleau, L.; Patarin, *J. CrystEngComm* 2013, 15, 3009.
(27) Maldonado, M.; Oleksiak, M. D.; Chinta, S.; Rimer, J. D. *J. Am. Chem. Soc.* 2013, *135*, 2641.
(28) Oleksiak, M. D.; Rimer, J. D. *Rev. Chem. Eng.* 2013, *30*, 1.

(29) Baerlocher, C.; McCusker, L. B. Database of Zeolite Structures: http://www.iza-structure.org/databases/.
(30) Goel, S., Zones, S., and Iglesia, E. *J. Am. Chem. Soc.* 2014, 136, 15280.
(31) Zones, S. I. Patent US8007763 B2, August 30, 2011.
(32) Musilová-Pavlačková, Z.; Zones, S. I.; Čejka, J. *Top. Catal.* 2010, 53, 273.
(33) Jones, A. J.; Zones, S. I.; Iglesia, E. *J. Phys. Chem. C* 2014, 118, 17787.
(34) Martens, J. A.; Jacobs, P. A. Synthesis of High-Silica Aluminosilicate Zeolites; Elsevier: New York, 1987.
(35) Auerbach, S. M.; Carrado, K. A.; Dutta, P. K. *Handbook of Zeolite Science and Technology*; M. Dekker: New York, 2003.
(36) Calero Diaz, S. In Zeolites and Catalysis; Čejka, J.; Corma, A.; Zones, S., Eds.; Wiley-VCH: Weinheim, Germany, 2010; pp. 335.
(37) Lee, P.-S.; Zhang, X.; Stoeger, J. A.; Malek, A.; Fan, W.; Kumar, S.; Yoo, W. C.; Al Hashimi, S.; Penn, R. L.; Stein, A.; Tsapatsis, M. *J. Am. Chem. Soc.* 2011, 133, 493.
(38) Sing, K. S. W.; Everett, D. H.; Haul, R. a. W.; Moscou, L.; Pierotti, R. A.; Rouquerol, J.; Siemieniewska, T. In *Handbook of Heterogeneous Catalysis*; Ertl, G., Ed.; Wiley-VCH: Weinheim, Germany, 2008.
(39) Iler, R. K. *The Chemistry of Silica: Solubility, Polymerization, Colloid and Surface Properties and Biochemistry of Silica*; Wiley: New York, 1979.
(40) Raatz F., Marcilly C., Freund E. *Zeolites* 1985, 5, 329.
(41) Möller, K.; Bein, T. *Chem. Soc. Rev.* 2013, 42, 3689.
(42) Ritsch, S.; Ohnishi, N.; Ohsuna, T.; Hiraga, K.; Terasaki, O.; Kubota, Y.; Sugi, Y. *Chem. Mater.* 1998, 10, 3958.

Chapter 6

Pore Accessibility Improvements in Zeolites Synthesized via Seed-Assisted Transformations without Organic Structure-Directing Agents

Abstract

CHA, STF and MTW zeolites (Na-form) synthesized via seed-assisted interzeolite transformations of FAU in the absence of organic structure-directing agents exhibited very low micropore volumes by N_2 adsorption measurements (0.094 cm^3/g, 0.027 cm^3/g and 0.006 cm^3/g for CHA, STF and MTW, respectively), inconsistent with the micropore volumes expected from the crystallinity values obtained from their X-ray diffraction (XRD) measurements (expected micropore volumes of 0.158 cm^3/g_{crys}, 0.156 cm^3/g_{crys} and 0.066 cm^3/g_{crys} (theoretical micropore volumes normalized per g of crystalline material) for CHA, STF and MTW, respectively). H-form of zeolites did not lead to any significant increase in micropore volumes compared to their Na-form, suggesting that low N_2 uptakes were not caused by the localization of alkali-cations at the pore mouth, which could lead to narrowing of pore apertures. Increased uptake with CO_2 adsorption measurements at 273 K in STF and MTW, compared to N_2 at 77 K and Ar at 87 K, suggested the presence of significant diffusion limitations using the latter adsorbates, which was overcome by CO_2 adsorption at higher temperature (273 K) and showed the presence of significant aperture narrowing in these materials, particularly in the one-dimensional framework structures such as STF and MTW compared to 3-dimensional CHA framework; these results further emphasize the importance of using the appropriate adsorbate and adsorption conditions for micropore volume analysis of zeolitic frameworks. However, micropore volumes by CO_2 adsorption measurements remained lower than those expected based on crystallinity values obtained from XRD measurements. These low CO_2 uptakes, taken together, with line broadening observed in ^{29}Si, ^{27}Al and ^{23}Na MAS NMR measurements suggested that the predominate pore blocking was caused by the presence of extra framework intracrystal species. Alkaline treatment followed by acid treatment proved effective in successfully unblocking these pores, forming accessible structures of CHA, STF and MTW zeolites without any significant loss of solid yields or changes in Si/Al ratios.

6.1 Introduction

Zeolites, crystalline aluminosilicate materials with voids of molecular dimensions, are widely used in adsorption, separation, ion-exchange and catalytic applications [1-6]. Zeolites are typically synthesized by hydrothermal synthesis in the presence of inorganic (e.g. Na^+, K^+, Li^+, etc.) and/or organic structure-directing agents (OSDA) in hydroxide, fluoride or ionic-liquid media [7-10]. OSDA reagents, in most cases, are the most expensive component of the synthesis and removal of these OSDA species occluded within zeolite micropores usually involve very high temperature treatments (up to 1000 K) and release of toxic species, which increase both the cost and environmental burdens of many large-scale zeolite syntheses. Much effort, therefore, has been devoted to the development of synthesis protocols with less expensive OSDA species [11, 12] or of those that eliminate the requirement of OSDA altogether [13-19] to decrease such costs and

avoid the emission of toxic species generated during the synthesis or the subsequent treatments required to decompose organic species contained within zeolite voids.

We have developed and reported previously, synthesis protocols and guiding principles, inspired by mechanistic considerations, for the synthesis of zeolites via interzeolite transformations that avoid the use of OSDA species [20]. More specifically, we synthesized high-silica CHA, STF, and MTW zeolites (Scheme 6.1) via seed-assisted interzeolite transformations without the addition of any organic structure-directing agents (OSDA). X-ray diffraction (XRD) patterns of the final zeolite products suggested the presence of highly crystalline zeolites but they exhibited low micropore volumes using N_2 adsorption measurements, lower than those expected based on crystallinity values obtained from their XRD measurements. In this work, we investigate the possible causes of such low N_2 uptakes by carrying out adsorption measurements with N_2, Ar and CO_2 at various temperatures to investigate the effect of adsorbate and adsorption conditions on resulting micropore volumes. Solid state ^{29}Si, ^{27}Al and ^{23}Na MAS NMR measurements are used to investigate, further, the presence of probable aperture narrowing and/or pore blocking species. A post-synthetic treatment strategy is proposed and performed, which led to successful pore unblocking in these materials to form accessible highly crystalline zeolite products necessary for catalytic applications.

6.2 Experimental Section

6.2.1 Reagents and Materials. NaOH (99.995%, Sigma Aldrich), FAU (CBV780, Zeolyst, Si/Al = 40, H-FAU), NH_4NO_3 solution (> 98%, Sigma-Aldrich) and HCl (Technical, Fisher Scientific) were used as received.

6.2.2 Synthesis Procedures

6.2.2.1 CHA, STF and MTW Seeds. The materials used as seeds were prepared using previously described synthesis procedures [20] for CHA, STF and MTW zeolites.

6.2.2.2 Synthesis of CHA, STF and MTW via Transformations of FAU. The synthesis of CHA, STF, and MTW zeolites was achieved by transformations of FAU as parent material. FAU (0.5-1.0 g) was added to an aqueous NaOH solution to achieve molar compositions of 0.68 NaOH: 1.0 SiO_2: 0.0125 Al_2O_3: 95 H_2O, into which 10% wt. (% wt. based on parent FAU) seed crystals (CHA, STF, or MTW) were added to prepare the final mixtures. These mixtures were placed within sealed polypropylene containers (Nalgene, 125 cm^3) and homogenized by vigorous magnetic stirring (400 rpm; IKA RCT Basic) for 1 h at ambient temperature. These mixtures were then transferred into a Teflon-lined stainless steel autoclave and held at 423 K for 40 h under static conditions. The resulting solids were collected by filtration through a fritted disc Buchner filter funnel (Chemglass, 150 ml, F) and washed with deionized water (17.9 MΩ·cm resistivity) until the rinse liquids reached a pH of 8-9. The samples were heated in a convection oven at 373 K overnight. The solid yields of the resulting products were defined as

$$Yield\ (\%) = \frac{Product\ (g)}{Parent\ zeolite\ (g) + Seeds\ (g)} \times 100 \qquad (1)$$

The samples were then treated in a tube furnace in flowing dry air (1.67 $cm^3\ g^{-1}\ s^{-1}$) to 873 K at 0.03 K s^{-1} and held at this temperature for 5 h. The resulting samples after treatment were denoted as Na-CHA-F, Na-STF-F and Na-MTW-F (where F = Fresh samples), synthesized via interzeolite transformations of FAU using seeds of CHA, STF, and MTW, respectively.

For the synthesis of the H-form of these zeolites, the treated Na-zeolite samples were added to an aqueous NH_4NO_3 solution (1 g zeolite per 100 cm^3 of 0.1 M solution) while stirring at 353 K for 4 h. The solids were recovered by filtration, and this process was repeated two more times to yield NH_4-zeolite. The samples were then treated in tube furnace in flowing dry air (1.67 $cm^3\ g^{-1}\ s^{-1}$) to 873 K at 0.03 K s^{-1} and held at this temperature for 3 h to form H-zeolite. The resulting samples after treatment were denoted as H-CHA-F, H-STF-F and H-MTW-F (where F = Fresh samples), H-form of zeolites synthesized via interzeolite transformations of FAU using seeds of CHA, STF, and MTW, respectively.

6.2.2.3 Post-Synthesis Treatment of Zeolite Samples. Fresh zeolite samples (Na-CHA-F, Na-STF-F and Na-MTW-F) were treated in aqueous NaOH (0.5 M, 1 g zeolite per 100 cm^3 of solution) at 338 K for 1 h under vigorous magnetic stirring (400 rpm; IKA RCT Basic). The resulting solids were collected by filtration through a fritted disc Buchner filter funnel (Chemglass, 150 ml, F), washed with deionized water (17.9 MΩ·cm resistivity) until the rinse liquids reached a pH of 8-9, and the collected solids were heated in a convection oven at 363 K overnight. The solids were then treated in aqueous HCl (0.1 M, 1 g zeolite per 100 cm^3 of solution) at 338 K for 8 h under vigorous magnetic stirring (400 rpm; IKA RCT Basic). The resulting solids were collected by filtration through a fritted disc Buchner filter funnel (Chemglass, 150 ml, F) and washed with deionized water (17.9 MΩ·cm resistivity) until the rinse liquids reached a pH of 7-8. The samples were heated in a convection oven at 363 K overnight. The samples were then treated in tube furnace in flowing dry air (1.67 $cm^3\ g^{-1}\ s^{-1}$) to 873 K at 0.03 K s^{-1} and held at this temperature for 5 h. The resulting samples after treatment were denoted as H-CHA-T, H-STF-T, H-MTW-T, synthesized via interzeolite transformations of FAU using seeds of CHA, STF, and MTW, respectively and subsequently treated in aqueous NaOH and HCl.

6.2.3 Characterizations. The identity and phase purity of the product zeolites were demonstrated by powder XRD measurements (Cu Kα radiation λ=0.15418 nm, 40 kV, 40 mA, Bruker D8 Advance). Diffractograms were collected for 2Θ values of 5-50^o at 0.02^o intervals with a 2 s scan time using MgO as an internal standard. The ratio of the sum of areas of three major peaks in the target material to that of their corresponding seed material (100% crystalline) was defined as the percentage crystallinity of each sample. Si, Al, and Na contents of the samples were measured by ICP-AES (IRIS Intrepid spectrometer; Galbraith Laboratories). Adsorption-desorption measurements of zeolite products were performed on ASAP 2020 (Micromeritics) or 3Flex (Micromeritics) at 77 K for N_2 and 87 K for Ar. Prior to the measurements, all samples were degassed at 623 K for 4 h under vacuum. t-plot method was used to calculate the micropore volume of the samples. CO_2 adsorption measurements were performed on Tristar 3000 (Micromeritics) at 195, 273 and 294 K. Prior to the measurements, all samples were degassed at 673 K for >24 h under vacuum. The micropore volumes from CO_2 adsorption at different temperatures were calculated by D-R method. A Bruker DSX-500 spectrometer was used to record ^{29}Si, ^{27}Al, and ^{23}Na MAS NMR spectra with their corresponding operating frequencies of 99.4, 130.3, and 132.3 MHz, respectively. A 4 mm Bruker MAS probe was employed to spin samples at 8 kHz for ^{29}Si

NMR or 14 kHz for ^{27}Al and ^{23}Na MAS NMR. ^{27}Al and ^{23}Na MAS spectra were collected with ^{1}H decoupling after a short 0.5 μs pulse that corresponded to 1/18π for ^{27}Al or 1/12π pulse for ^{23}Na nuclei. NMR spectra are reported in part per million (ppm) after calibration to 0 ppm to external standards such as tetramethylsilane (TMS), 1M aqueous solution of $Al(NO_3)_3$ and NaCl.

6.3 Results and Discussion

6.3.1 CHA Zeolite Synthesized via Seed-Assisted Transformations of Parent FAU

Parent FAU zeolite with lower framework density (framework density (FD) 13.3, represented in T atom/nm^3) was successfully transformed into thermodynamically-favored more stable CHA structure with higher framework density (FD 15.1) via recrystallization in aqueous NaOH at hydrothermal conditions (Scheme 6.1). Successful transformation required the addition of CHA seeds to overcome kinetic hurdles while exploiting the thermodynamic tendency of microporous solids to increase their framework density. The synthesis of high-silica CHA (Si/Al = 11) was achieved from transformations of FAU ($0.68NaOH: 1.0SiO_2: 0.0125Al_2O_3: 95H_2O$, 423 K, 40 h) with CHA seeds, using the developed synthesis guidelines [20]. CHA products were 66% crystalline, measured by powder XRD using MgO as an internal standard (Table 6.1); yet, the micropore volume, obtained from N_2 adsorption measurements, of these CHA products was 0.094 cm^3/g (Table 6.1, Figure 6.1), which is smaller than the theoretical void space of CHA (0.24 cm^3/g, [21]), consistent with the presence of some amorphous solids in the final material but inconsistent with measurements that indicated high crystallinity from XRD.

The H-CHA sample, prepared by ammonium ion exchange of synthesized Na-CHA sample and subsequent high temperature air treatments, showed no significant differences in the amount of nitrogen adsorbed (micropore volume 0.095 cm^3/g, Table 6.1) compared to that of Na-CHA, (0.094 cm^3/g, Table 6.1) suggesting that the pore blocking is not caused by localization of alkali cations at the pore entrances but perhaps by the presence of amorphous solids that can lead to a narrowing of pore openings or of extra framework debris that can cause pore filling.

The solid-state ^{29}Si MAS NMR spectra (Figure 6.2a) of treated CHA seeds and CHA product (Na-CHA-F), synthesized via seed-assisted interzeolite transformations of FAU, exhibited two sharp resonances at ~ -105 and -111 ppm, which correspond to Si(1Al) and Si(0Al) of CHA frameworks [22], respectively. The CHA product (Figure 6.2a(ii)), unlike CHA seeds (Figure 6.2a(i)), showed the presence of a broad background underneath the sharp peaks, likely associated with either the existence of partially amorphous regions or distortion of Si centers. The sharp/broad peak ratio, obtained by deconvolution of the spectral lines and a measure of structure amorphization, was 0.45 for CHA product and 1.81 for CHA seeds; higher value of this ratio exhibited by the CHA seeds (assumed 100% crystalline material) compared to the CHA product further supports the presence of significant amorphous regions or distorted Si centers in the final product.

The solid-state ^{27}Al MAS NMR spectra (Figure 6.2b) of treated CHA seeds and CHA product (Na-CHA-F) showed only one peak centered at ~ 59 ppm, which corresponds to tetrahedrally-coordinated Al [22] and there was no peak centered at ~ 0 ppm, suggesting the absence of octahedrally-coordinated extra-framework Al centers, both in CHA seeds and CHA product. This

data suggest that that almost all Al centers in the samples are located at the tetrahedral sites of the CHA framework. CHA product (Figure 6.2b(ii)), however, showed significant line broadening (down to ~ 40 ppm), compared to that of CHA seeds, possibly indicative of distortion of Al centers but cannot be derived from the presence of extra framework AlO_6 formation due to its absence. The broadening of this peak could also be the result of incomplete hydration of Al, generally carried out before NMR measurements at ambient temperature to weaken Al quadrupolar interactions and sharpen NMR lines [23, 24], possibly as a result of the inaccessibility of H_2O to Al centers located in the blocked pores. The solid state ^{23}Na MAS NMR spectra of CHA product (Na-CHA-F, Figure 6.S1) also exhibited line broadening similar to that seen in the solid-state ^{27}Al MAS NMR spectra, suggesting the presence of Na ions is directly related to the line broadening in ^{27}Al MAS NMR. The Na/Al ratio obtained from these NMR measurements is 1.0 while the ratio obtained from ICP analysis is 0.58, indicating, further, that some of the Al centers residing in blocked intracrystal locations may be invisible [24] as sharp peaks in ^{27}Al MAS NMR measurements.

These solid-state MAS NMR measurements, taken together, suggest that the CHA product synthesized via seed-assisted transformations of FAU show significant distortion of framework Al and Si species or distorted extra framework intracrystal species, but the exact nature of disorder and relevant extra framework species are not evident from these measurements.

Ar adsorption measurements at 87 K in CHA product showed micropore volume (0.070 cm^3/g, Table 6.1) similar to that obtained using N_2 adsorption (0.094 cm^3/g, Table 6.1), suggesting that the presence of a quadrupole moment in N_2 molecules (which is absent in Ar) is not causing the low micropore volumes because that may lead to specific interactions with the exposed cations and strongly affect the orientation of adsorbed N_2 molecule on the zeolitic surface and shift the initial stages of physisorption to very low pressures, where the rate of diffusion is extremely low [25]. Slightly higher adsorption temperature of Ar (87 K), which may lead to accelerated diffusion and faster equilibration time, did not lead to increase in micropore volumes suggesting that either sufficiently high diffusion barriers at low temperature of adsorption for both N_2 and Ar adsorbates lead to very high equilibration times, resulting in inaccessibility of adsorbate to CHA voids in the experimental time frame, or some of the void spaces are completely blocked, leading to lower micropore volumes.

CO_2 adsorption measurements of CHA product at 195 K resulted in micropore volume of 0.084 cm^3/g (Table 6.1, Figure 6.S2), similar to those obtained using N_2 and Ar adsorption measurements (Table 6.1, Figure 6.1). Further increase in CO_2 adsorption temperature to 273 and 294 K (from 195 K) did not lead to any increase in micropore volume of CHA product (0.083 and 0.076 cm^3/g for 273 and 294 K, respectively; Table 6.1, Figure 6.S2), suggesting that the pore aperture narrowing in CHA product is unlikely because the higher adsorption temperature, that may eliminate diffusion limitations due to higher temperature and high saturation pressure (26,200 torr [25]), and slightly lower size of CO_2 (0.33 nm) than N_2 (0.36 nm) and Ar (0.34 nm) molecule did not lead to any significant increase in adsorbate uptake. These data, taken together, suggest that lower micropore volumes by N_2, Ar and CO_2 adsorption measurements is not caused by pore aperture narrowing, rather most likely due to the complete pore blocking of some of the void spaces in CHA zeolite by intracrystal extra framework debris.

The fresh CHA sample after the hydrothermal synthesis was not cooled completely (from synthesis temperature of 423 K) but instead hot filtered at 373 K, to prevent re-precipitation of dissolved Si species at the external surfaces of zeolites while cooling, and excessively washed with deionized water to remove inter crystal extra framework species. The resulting material after thermal treatment (dry air (1.67 $cm^3 g^{-1} s^{-1}$), 873 K (0.03 K s^{-1}) for 5 h) lead to micropore volume of 0.102 cm^3/g (Table 6.S1) by N_2 adsorption measurements, similar to that of fresh CHA product (0.094 cm^3/g, Table 6.1), indicating that hot filtration was not effective to remove the pore blocking debris. This data also suggests that the lower micropore volume was not caused by the precipitation of excess Si species from solution to form sodium silicate-type species at the external surfaces of zeolites, which may lead to blocking or narrowing of pore entrances, but perhaps due to intracrystal extra framework species trapped in the zeolite voids during transformations itself. This data is consistent with the absence of ~ -70 ppm line, attributed to sodium silicate species [26], in solid state ^{29}Si MAS NMR measurements (Figure 6.2a) of CHA product. Therefore, post synthesis treatments, in this case, could be effective in removing such trapped species from zeolitic voids and unblocking the pores.

We surmise that the trapped extra framework species would most likely be Si-rich in nature, because the gel of transformation synthesis is Si-rich (due to high-silica parent FAU (Si/Al = 40)), that can be removed by alkaline NaOH treatment. Alkaline treatment with 0.5 M NaOH at 338 K for 1 h, however, led to micropore volume of 0.105 cm^3/g (Table 6.S1) by N_2 adsorption; a value only slightly higher than that obtained for the fresh zeolite and still lower than the value expected from % crystallinity obtained by XRD measurements. The slight increase in micropore volume observed after alkaline treatment is in contrast with decrease of micropore volumes reported after such alkaline treatments in zeolites [28], suggesting that the alkaline treatment, in this case, is selectively removing the extra framework Si species rather than framework Si centers, which would otherwise lead to a decrease in micropore volume as a result of Si extraction from the framework and concomitant formation of extra framework amorphous regions. Furthermore, only a slight increase in micropore volume after alkaline NaOH treatment indicates the presence of additional pore blocking debris or obstructions at the pore entrances.

Acid treatment (0.1 M HCl, 8 h) following the alkaline NaOH treatment (0.5 M NaOH, 1 h) resulted in higher micropore volume (Table 6.1) of 0.191 cm^3/g by N_2 adsorption (77 K) and 0.251 cm^3/g by CO_2 adsorption (273 K) measurements, consistent with that reported for mesoporosity generation in zeolite frameworks where a subsequent acid treatment after alkaline treatment is found to be essential to remove the Al-rich debris and unblock the micropore mouths [28]. This is also consistent with studies on MOR zeolites, where researchers have succeeded in unblocking pores or removing aperture narrowing by dealumination with acid treatment [27] under suitable conditions.

The resulting micropore volumes (Table 6.1) of 0.191 cm^3/g by N_2 and 0.251 cm^3/g by CO_2 adsorption measurements are consistent with the value expected based on crystallinity measurements from XRD, suggesting that the zeolitic pores are unblocked after the treatment and thus, available for adsorption of N_2 molecules during physisorption measurements. The final CHA sample (H-CHA-T), after post-synthesis treatment, showed Si/Al ratio of 11, same as that of fresh CHA (Si/Al =11), and overall solid yield of the synthesis did not decrease significantly (22 % for treated sample (H-form) vs 27 % for fresh sample (Na-form), Table 6.1), suggesting that these

treatments are effective in unblocking the pores without significant damage to the framework structure, while retaining its crystallinity and solid yield.

6.3.2 STF and MTW Zeolites Synthesized via Seed-Assisted Transformations of Parent FAU

STF and MTW zeolites were synthesized via seed-assisted interzeolite transformations of FAU ($0.68NaOH: 1.0SiO_2: 0.0125Al_2O_3: 95H_2O$, 423 K, 40 h, with 10 % wt. STF/MTW seeds) without the addition of organic structure-directing agents in the synthesis gel [20]. STF and MTW products were 78 and 60% crystalline, respectively, measured by powder XRD using MgO as an internal standard (Table 6.1); yet, their micropore volume (from N_2 adsorption) were 0.027 and 0.006 cm^3/g (Table 6.1), respectively, values much smaller than theoretical values for STF (0.20 cm^3/g [21]) and MTW structure (0.11 cm^3/g [21]), similar to the case of fresh CHA product. The low values of accessible micropore volumes in the STF and MTW zeolites formed via seed-assisted synthesis from FAU are not consistent with their crystalline nature and may reflect ubiquitous channel blockages that have been reported for one-dimensional zeolites, such as STF and MTW. Previous studies on MOR zeolites [27, 29] have concluded that such blockages account for the inability of MOR structures to adsorb molecules with kinetic diameters larger than ~0.4 nm; such blockages have also been attributed to intrachannel amorphous debris and to cations or defects along the main channels in MOR. Such factors may also account for the low accessible micropore volumes reported here for STF and MTW zeolites.

H-STF and H-MTW samples, prepared by exchanging the seed-assisted Na-STF and Na-MTW samples with NH_4^+ cations and treatment in air at 873 K did not lead to larger N_2 uptakes than the Na-containing samples (Micropore volumes; Table 6.1), analogous to that observed for CHA. We conclude, therefore, that any channel blockages are not caused by Na cations but may reflect instead the presence of amorphous intrachannel debris or structural defects that may form within the one-dimensional channels during crystal growth. The extensive twinning and faulting in MTW frameworks, caused by the incoherent stacking of polymorphs, have been reported in MTW prepared via OSDA-assisted [30] and OSDA-free [14] protocols from amorphous aluminosilicate gels. Stacking faults may also form during synthesis without OSDA, but such effects cannot be detected via powder XRD due to their local nature and low density.

Ar adsorption at 87 K gave micropore volumes (Table 6.1) of 0.005 cm^3/g for STF and 0.005 cm^3/g for MTW, respectively; values much lower than that expected from crystallinity obtained by XRD measurements. CO_2 adsorption at 273 K (Figure 6.S2), however, resulted in micropore volume (Table 6.1) of 0.072 and 0.045 cm^3/g for STF and MTW, respectively. These higher micropore volumes by CO_2 adsorption than those obtained using N_2 and Ar in STF and MTW zeolites, in contrast to CHA, suggest significant aperture narrowing, more pronounced in STF and MTW possibly due to 1-D nature of these frameworks in contrast to 3-D CHA framework. Increasing the CO_2 adsorption temperature to 294 K (from 273 K) did not lead to any further increase in micropore volume (Table 6.1) of STF zeolite, suggesting that CO_2 adsorption temperature of 273 K was sufficient to overcome the diffusion limitations caused by aperture narrowing. The aperture narrowing occurring in STF and MTW zeolites was, thus, overcome by adsorption measurements at higher temperature and high pressure leading to accelerated diffusion and faster equilibration times. The higher micropore volume obtained by CO_2 adsorption, in contrast to the lower micropore volumes by N_2 and Ar adsorption measurements, further

emphasizes the importance of using the appropriate adsorbate and adsorption conditions for pore volume measurements of small-pore zeolites, as also recommended by others [25, 31-33] previously. The micropore volumes obtained by CO_2 adsorption measurements, however, are still lower than the values expected from XRD measurements, suggesting that the pore blockages are still prevalent in these materials.

To remove extra framework debris, alkaline treatment (0.5 M NaOH, 1h) followed by acid treatment (0.01 M HCl, 8 h), similar to that done in CHA which resulted in unblocking of pores, was performed, which led to micropore volumes (Table 6.1) of 0.131 cm^3/g by N_2 at 77 K and 0.171 cm^3/g by CO_2 at 273 K in STF zeolites and 0.084 cm^3/g by N_2 adsorption measurements in MTW zeolites. These micropore volumes are much higher than those of fresh STF (0.027 cm^3/g (N_2 adsorption at 77 K), Table 6.1) and MTW (0.006 cm^3/g (N_2 adsorption at 77 K), Table 6.1) zeolites and consistent with the values expected from XRD measurements, suggesting that these post-synthesis treatments have successfully unblocked the zeolitic pores. The Si/Al ratio of treated samples (11 and 12 for STF and MTW, respectively; Table 6.1) was similar to the fresh samples (11 and 15 for STF and MTW, respectively; Table 6.1) and the overall solid yields (Table 6.1) of treated samples were 23 and 22 % for STF and MTW, respectively, compared to 27 and 28 % for fresh STF and MTW samples, respectively, confirming that these treatments are effective in removing the extra framework debris without significantly damaging the zeolite framework structures.

6.4 Conclusions

We have investigated some of the possible causes of low micropore volumes, obtained by N_2 adsorption measurements, and demonstrated a strategy to unblock the pores that become blocked during the synthesis of CHA, STF and MTW zeolites via seed-assisted interzeolite transformations of FAU. The small micropore volumes by N_2 and Ar adsorption measurements suggested restricted diffusion, which was overcome by CO_2 adsorption at higher temperature (273 K). CO_2 adsorption at 273 K led to higher micropore volumes in STF (0.072 cm^3/g) and MTW (0.045 cm^3/g), in contrast to the absence of significant increases in CHA, suggesting that aperture narrowing occurred in these zeolites, more severe as a result of their one-dimensional pore structures compared to the 3-D framework of CHA. Solid state MAS NMR and physisorption measurements suggested the presence of significant framework disorder or extra framework debris, which led to line broadening in NMR and low micropore volumes by adsorption measurements. The predominant pore blocking, however, was caused by extra framework debris, which was successfully removed by alkaline treatment and subsequent acid treatment. Higher micropore volumes, similar Si/Al ratios and solid yields of fresh and treated zeolites confirmed the effectiveness of these treatments in selectively removing extra framework debris while preserving framework Si and Al species. Our developed strategy and understanding gained in post-synthetic pore unblocking to form accessible and highly crystalline zeolite products can be extended to other target zeolite frameworks, enhancing their adsorption capabilities that are important in both catalytic and separation applications.

6.5 Acknowledgments

The authors acknowledge with thanks Dr. Sonjong Hwang (Caltech) for performing NMR measurements, Dr. Howard Lacheen (Chevron) for CO_2 adsorption measurements and Chevron Energy Technology Company for the financial support for this research.

6.6 Figures, Tables and Scheme

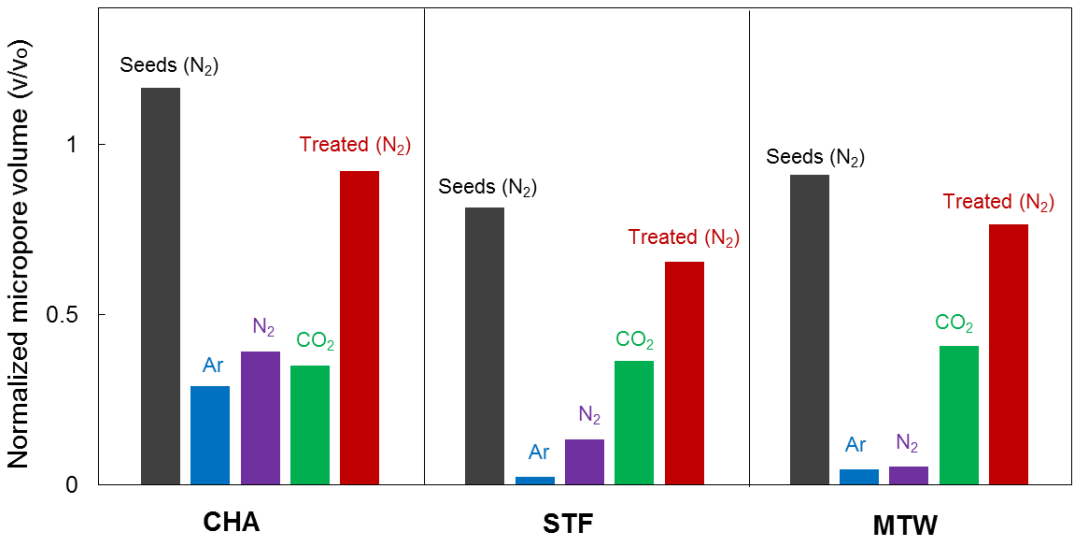

Figure 6.1 Normalized micropore volumes (v/v_0, where v = micropore volume of desired zeolite product and v_0 = theoretical micropore volume for corresponding zeolite framework) of zeolite seeds measured by N_2 adsorption (black), zeolites synthesized via seed-assisted interzeolite transformations and measured by Ar (blue), N_2 (purple) and CO_2 (green) adsorption and of post synthesis treated zeolites by N_2 adsorption (red) measurements.

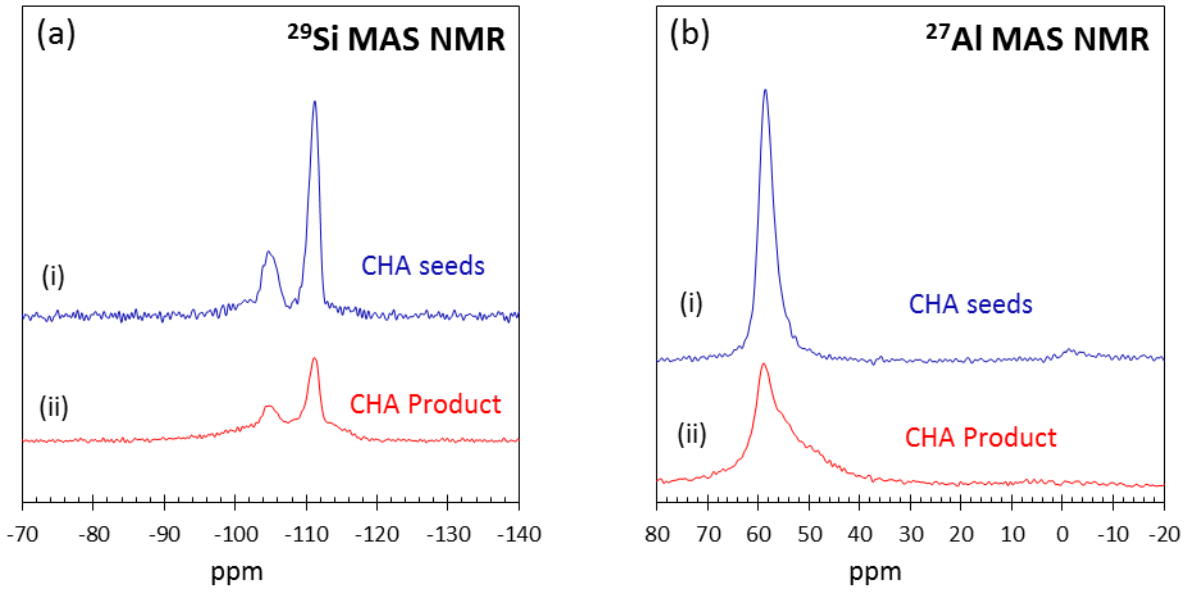

Figure 6.2 Solid-state (a) ^{29}Si MAS NMR and (b) ^{27}Al MAS NMR spectra of (i) CHA seeds (Si/Al =15) and (ii) CHA product (Si/Al = 11) synthesized via seed-assisted transformations of FAU.

Table 6.1 Percentage crystallinity, micropore volumes, Si/Al ratios and solid yields of zeolite seeds and fresh and post-synthesis treated zeolites synthesized via seed-assisted transformations of FAU.

Sample	Crystallinity	Micropore volume (cm^3/g)					Si/Al [c]	Solid yield (%)[d]
	(%)	Ar (87 K)[a]	N_2 (77 K) [a]	CO_2 (195 K)[b]	CO_2 (273 K)[b]	CO_2 (294 K)[b]		
CHA seed	100	-	0.280	-	-	-	15	-
STF seeds	100	-	0.163	-	-	-	20	-
MTW seeds	100	-	0.100	-	-	-	30	-
Na-CHA-F	66	0.07	0.094	0.084	0.083	0.076	11	27
Na-STF-F	78	0.005	0.027	0.073	0.072	0.064	11	27
Na-MTW-F	60	0.005	0.006	-	0.045	-	12	28
H-CHA-F	-	-	0.095	-	-	-	-	-
H-STF-F	-	-	0.021	-	-	-	-	-
H-MTW-F	-	-	0.006	-	-	-	-	-
H-CHA-T	86	-	0.191	-	0.251	-	11	22
H-STF-T	85	-	0.131	-	0.171	-	11	23
H-MTW-T	83	-	0.084	-	-	-	15	22

[a] Micropore volumes from N_2 and Ar adsorption measurements are obtained using t-plot method.
[b] Micropore volumes from CO_2 adsorption measurements are obtained using D-R method.
[c] Analyzed by inductively coupled plasma optical emission spectroscopy.
[d] $yield\ (\%) = \frac{Product\ (g)}{Parent\ zeolite\ (g)+Seed\ (g)}\ x\ 100$

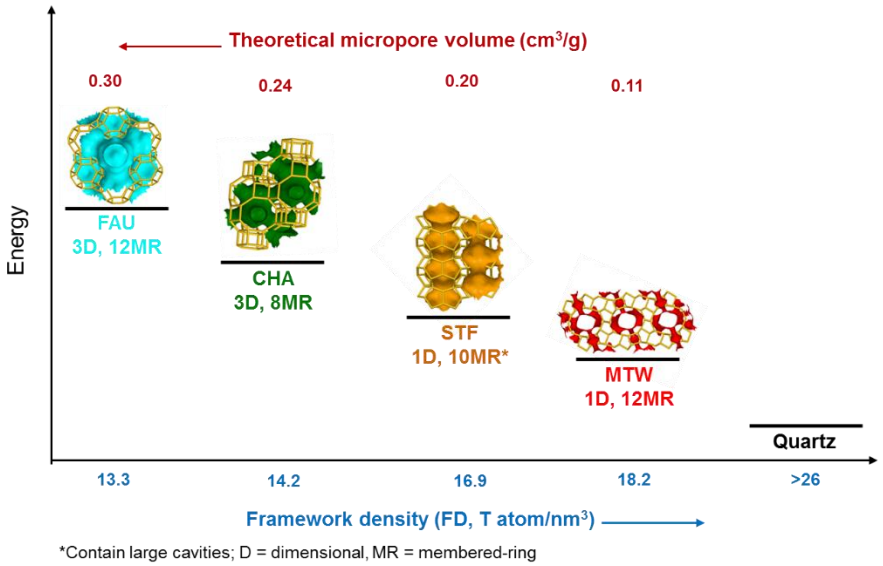

Scheme 6.1 Schematic representation of parent (FAU) and product (CHA, STF, and MTW) zeolite frameworks in an energy landscape with their corresponding theoretical micropore volumes and framework densities. The energy and framework density placement in the scheme is not to scale.

6.7 Supporting Information

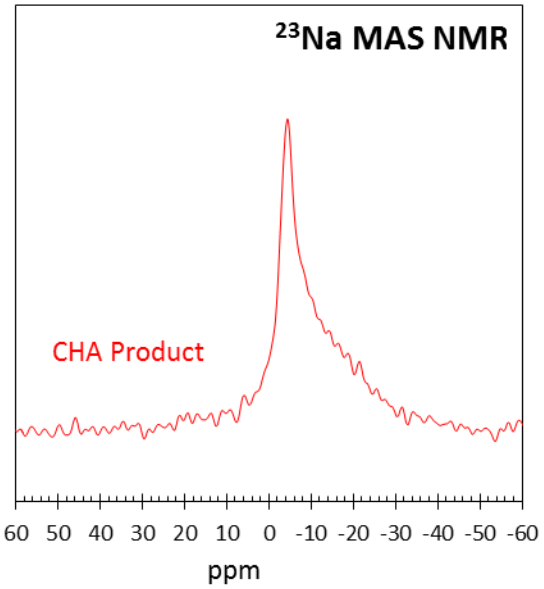

Figure 6.S1 Solid-state ^{23}Na MAS NMR spectra of CHA product (Si/Al = 11) synthesized via seed-assisted transformations of FAU.

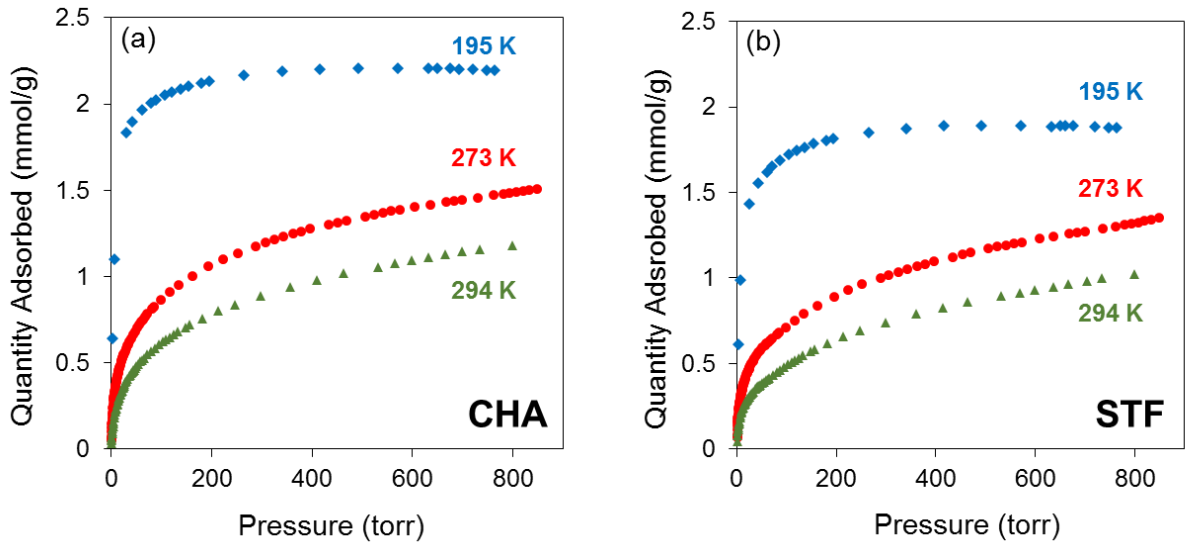

Figure 6.S2 CO_2 adsorption isotherms of fresh (a) CHA (Na-CHA-F) and (b) STF (Na-STF-F) zeolites, synthesized via seed-assisted transformations of FAU, at adsorption temperatures of 195, 273, and 294 K.

Table 6.S1 Micropore volumes of CHA seeds and fresh and post-synthesis treated CHA products synthesized via seed-assisted transformations of FAU.

Sample	Micropore volume (cm^3/g)		
	N_2 (77 K)[a]	Ar (87 K)[a]	CO_2 (273 K)[b]
CHA seeds	0.280	-	-
Na-CHA-F	0.094	0.070	0.083
Na-CHA-F (After hot filtration)	0.102	-	-
H-CHA-F	0.095	-	-
H-CHA-T (After NaOH treatment)	0.105	-	-
H-CHA-T (After NaOH + HCl treatment)	0.191	-	-

[a] Micropore volumes from N_2 and Ar adsorption measurements are obtained using t-plot method.
[b] Micropore volumes from CO_2 adsorption measurements are obtained using D-R method.

6.8 References

(1) Weisz, P. B.; Frilette, V. J.; Maatman, R. W.; Mower, E. B. *J. Catal.* 1962, *1* (4), 307.
(2) Csicsery, S. M. *Zeolites* 1984, *4* (3), 202.
(3) Corma, A. *Chem. Rev.* 1995, *95* (3), 559.
(4) Corma, A. *Chem. Rev.* 1997, *97* (6), 2373.
(5) Davis, M. E. *Nature* 2002, *417* (6891), 813.
(6) Davis, M. E. *Chem. Mater.* 2014, *26* (1), 239.
(7) R. M. Barrer. In *Zeolite Synthesis*; ACS Symposium Series; American Chemical Society, 1989; Vol. 398, pp 11–27.
(8) Cundy, C. S.; Cox, P. A. *Microporous Mesoporous Mater.* 2005, *82* (1–2), 1.
(9) Meng, X.; Xiao, F.-S. *Chem. Rev.* 2014, *114* (2), 1521.
(10) Moliner, M.; Martínez, C.; Corma, A. *Chem. Mater.* 2014, *26* (1), 246.
(11) Zones, S. I.; Hwang, S.-J. *Chem. Mater.* 2002, *14* (1), 313.
(12) Lee, H.; Zones, S. I.; Davis, M. E. *Nature* 2003, *425* (6956), 385.
(13) Xie, B.; Zhang, H.; Yang, C.; Liu, S.; Ren, L.; Zhang, L.; Meng, X.; Yilmaz, B.; Müller, U.; Xiao, F.-S. *Chem. Commun.* 2011, *47* (13), 3945.
(14) Kamimura, Y.; Itabashi, K.; Okubo, T. *Microporous Mesoporous Mater.* 2012, *147* (1), 149.
(15) Kamimura, Y.; Tanahashi, S.; Itabashi, K.; Sugawara, A.; Wakihara, T.; Shimojima, A.; Okubo, T. *J. Phys. Chem. C* 2011, *115* (3), 744.
(16) Wheatley, P. S.; Chlubná-Eliášová, P.; Greer, H.; Zhou, W.; Seymour, V. R.; Dawson, D. M.; Ashbrook, S. E.; Pinar, A. B.; McCusker, L. B.; Opanasenko, M.; Čejka, J.; Morris, R. E. *Angew. Chem. Int. Ed.* 2014, *53* (48), 13210.
(17) Itabashi, K.; Kamimura, Y.; Iyoki, K.; Shimojima, A.; Okubo, T. *J. Am. Chem. Soc.* 2012, *134* (28), 11542.
(18) Maldonado, M.; Oleksiak, M. D.; Chinta, S.; Rimer, J. D. *J. Am. Chem. Soc.* 2013, *135* (7), 2641.
(19) Honda, K.; Itakura, M.; Matsuura, Y.; Onda, A.; Ide, Y.; Sadakane, M.; Sano, T. *J. Nanosci. Nanotechnol.* 2013, *13* (4), 3020.
(20) Goel, S.; Zones, S. I.; Iglesia, E. *Chem. Mater.* 2015, *27*(6), 2056.
(21) Calero Diaz, S. In Zeolites and Catalysis; Čejka, J.; Corma, A.; Zones, S., Eds.; Wiley-VCH Verlag GmbH & Co. KGaA, 2010; pp. 335–360.
(22) Klinowski, J. Annu. Rev. Mater. Sci. 1988, 18 (1), 189.
(23) Gounder, R.; Jones, A. J.; Carr, R. T.; Iglesia, E. J. Catal. 2012, 286, 214.
(24) Kraus, H.; Müller, M.; Prins, R.; Kentgens, A. P. M. J. Phys. Chem. B 1998, 102 (20), 3862.
(25) Thommes, M.; Cychosz, K. A. *Adsorption* 2014, *20* (2-3), 233.
(26) Tognonvi, M. T.; Massiot, D.; Lecomte, A.; Rossignol, S.; Bonnet, J.-P. J. Colloid Interface Sci. 2010, 352 (2), 309.
(27) Raatz, F.; Freund, E.; Marcilly, C. *J. Chem. Soc. Faraday Trans. 1 Phys. Chem. Condens. Phases* 1983, *79* (10), 2299.
(28) Verboekend, D.; Mitchell, S.; Milina, M.; Groen, J. C.; Pérez-Ramírez, J. *J. Phys. Chem. C* 2011, *115* (29), 14193.
(29) Van Geem, P. C.; Scholle, K. F. M. G. J.; Van der Velden, G. P. M.; Veeman, W. S. *J. Phys. Chem.* 1988, *92* (6), 1585.

(30) Ritsch, S.; Ohnishi, N.; Ohsuna, T.; Hiraga, K.; Terasaki, O.; Kubota, Y.; Sugi, Y. *Chem. Mater.* 1998, 10, 3958.
(31) García-Martínez, J.; Cazorla-Amorós, D.; Linares-Solano, A. In *Studies in Surface Science and Catalysis*; K.K. Unger, G. K. and J. P. B., Ed.; Characterization of Porous Solids V; Elsevier, 2000; Vol. 128, pp 485–494.
(32) Thommes, M. *Chem. Ing. Tech.* 2010, *82* (7), 1059.
(33) Smeets, S.; Xie, D.; McCusker, L. B.; Baerlocher, C.; Zones, S. I.; Thompson, J. A.; Lacheen, H. S.; Huang, H.-M. *Chem. Mater.* 2014, *26* (13), 3909.